TIME-AVERAGED OPTICAL POTENTIALS FOR CREATING AND SHAPING BOSE-EINSTEIN CONDENSATES

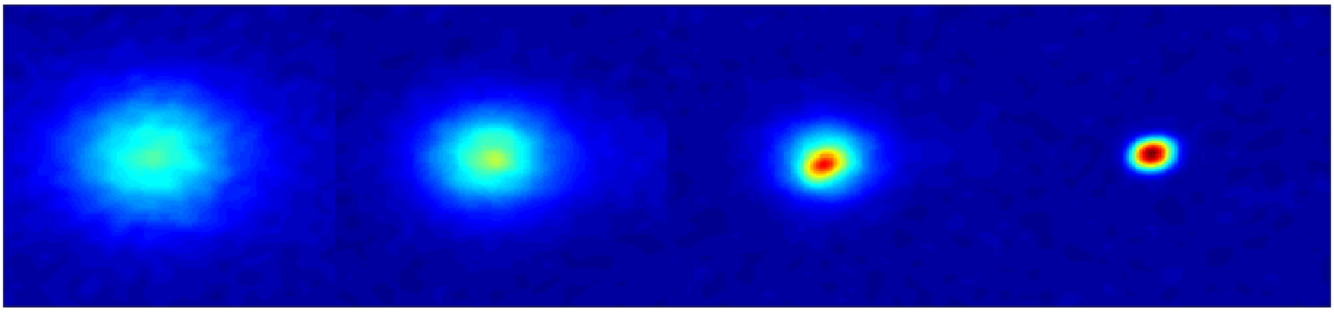

PhD thesis by Henning Albers
Hannover 2020

Für
Saskia & Finn

Henning Albers: *Time-Averaged Optical Potentials for Creating and Shaping Bose-Einstein Condensates,*© 2020

The cover picture shows a series of density profiles taken at different stages of a phase transition (see chapter 4).

TIME-AVERAGED OPTICAL POTENTIALS FOR CREATING AND SHAPING BOSE-EINSTEIN CONDENSATES

Von der QUEST-Leibniz-Forschungsschule der
Gottfried Wilhelm Leibniz Universität Hannover

zur Erlangung des Grades
Doktor der Naturwissenschaften
- Dr. rer. nat. -
genehmigte Dissertation von

M.Sc. Henning Albers
geboren am 17.05.1986,
in Bückeburg

2020

Referent:
Prof. Dr. Ernst M. Rasel
Institut für Quantenoptik
Gottfried Wilhelm Leibniz Universität Hannover

Korreferent:
Dr. Dennis Schlippert
Institut für Quantenoptik
Gottfried Wilhelm Leibniz Universität Hannover

Korreferent:
Prof. Dr. Claus Lämmerzahl
ZARM
Universität Bremen

Tag der Disputation:
19.08.2020

ABSTRACT

TIME-AVERAGED OPTICAL POTENTIALS FOR CREATING AND SHAPING BOSE-EINSTEIN CONDENSATES

The precision of atom interferometers, targeted for example in the Hannover Very Long Baseline Atom Interferometer (VLBAI) facility, imposes stringent requirements in several respects. They concern the control of center-of-mass motion and expansion of the wave packets by the matter-wave source as well as the number of atoms. By reducing the expansion, systematic errors, appearing e.g. through wavefront aberrations, can be lowered. These requirements can be matched by employing ultracold quantum gases or even quantum degenerate gases. A promising method to create those ensembles is evaporative cooling in a spatially modulated optical dipole trap. Here, the utilization of time-averaged potentials enables the fast creation of ultracold atomic ensembles with large number of atoms. Both, the higher number of atoms and the increased repetition rate, enhance the performance of the interferometer due to a lower quantum projection noise, which scales with $1/\sqrt{N}$, and a larger bandwidth of the sensor due to faster sampling. The shaping of the matter-waves by techniques such as matter-wave lensing or Delta-Kick collimation is also feasible due to the dynamic control of the trapping potential.

In this thesis the implementation and application of dynamic time-averaged optical potentials created via center position modulation of dipole trap beams is demonstrated. By evaporative cooling in these potentials, $1.9(0.4) \times 10^5$ condensed atoms with an expansion temperature of $29.2(1.3)$ nK were achieved after 3 s of evaporation. Up to $4.2(0.1) \times 10^5$ condensed atoms could be observed with slower evaporation of 5 s. Subsequent matter-wave lensing is carried out yielding expansion rates as low as $553(49)\ \mu\mathrm{m\,s^{-1}}$ resulting in an effective temperature of $3.2(0.6)$ nK in two dimensions. This lens can be applied at any stage of evaporative cooling, thus short-cutting the generation of ultracold effective temperatures. In this thesis the limitations of optical matter-wave lensing in the current setup are revealed and ways to improve the performance are discussed.

The fast generation of ultracold atomic ensembles will enhance the performance of the dual-species atom interferometer, which represents the experiment apparatus for this thesis and strives for a test of the Universality of Free Fall with an uncertainty on the order of 10^{-9}. The results of this thesis were used to test numerical simulations which were utilized to show the perspective of generating up to 10^6 collimated condensed atoms within 1 s of cycle time in the rubidium source system of Hannover's VLBAI.

Keywords: time-averaged optical Potentials, Bose-Einstein Condensate, Matter-Wave lensing

ZUSAMMENFASSUNG

ZEITLICH GEMITTELTE OPTISCHE POTENTIALE ZUR ERZEUGUNG UND MANIPULATION VON BOSE-EINSTEIN KONDENSATEN

Die Präzision von Atominterferometern, welche beispielsweise das Hannoveraner Very Long Baseline Atom Interferometer (VLBAI) anstrebt, stellt in mehrfacher Hinsicht hohe Anforderungen. Sie betreffen die Kontrolle der Schwerpunktbewegung und Ausdehnung der Wellenpakete durch die Materiewellenquelle als auch die Atomzahl. Durch die Reduzierung der Ausdehnung können systematische Fehler, die z.B. durch Wellenfrontstörungen auftreten, verringert werden. Diese Anforderungen können durch den Einsatz ultrakalter Quantengase oder sogar quantendegenerierter Gase erreicht werden. Eine vielversprechende Methode zur Erzeugung solcher Ensembles ist die Verdampfungskühlung in einer räumlich modulierten optischen Dipolfalle. Diese zeitlich-gemittelten Potentiale ermöglichen die schnelle Erzeugung großer ultrakalter atomarer Ensembles. Sowohl die höhere Atomzahl, geringeres Quantenprojektionsrauschen, skaliert mit $1/\sqrt{N}$, als auch die erhöhte Wiederholungsrate, größere Bandbreite des Sensors, verbessern die Leistung eines Interferometers. Auch die weitere Manipulation der Wellen-Pakete durch Techniken wie Materie-Wellen Linsen oder Delta-Kick-Kollimation ist in diesen dynamischen Potentialen möglich.

In dieser Arbeit wird die Implementierung und Anwendung von dynamischen zeitlich-gemittelten optischen Potentialen, durch Modulation der Mittenposition von Dipolfallenstrahlen, gezeigt. Durch Verdampfungskühlung wurden $1.9(0.4) \times 10^5$ kondensierte Atome mit einer Ausdehnungstemperatur von $29.2(1.3)$ nK nach 3 s Kühldauer erreicht. Bis zu $4.2(0.1) \times 10^5$ kondensierte Atome konnten bei einer langsameren evaporativen Kühlung von 5 s beobachtet werden. Durch den Einsatz einer optischen Materiewellen-Linsen in zwei Raumrichtungen wurde die Expansionsrate bis auf $553(49)$ $\mu\text{m}\,\text{s}^{-1}$ reduziert, was einer effektiven Temperatur von $3.2(0.6)$ nK entspricht. Diese Linse kann in jeder Phase der Verdampfungskühlung durchgeführt werden, wodurch die Erzeugung ultrakalter effektiver Temperaturen abgekürzt wird. In dieser Arbeit werden die Grenzen der optischen Materiewellen-Linse im gegenwärtigen Aufbau aufgezeigt und Möglichkeiten zur Verbesserung diskutiert.

Die schnelle Erzeugung ultrakalter atomarer Ensembles wird die Leistung des Zwei-Spezies-Atom-Interferometers verbessern, das den Versuchsapparat für diese Arbeit darstellt und einen Test der Universalität des freien Falls mit einer Unsicherheit in der Größenordnung von 10^{-9} anstrebt. Außerdem werden die Ergebnisse verwendet, um numerische Simulationen zu testen, die die Perspektive zur Erzeugung von bis zu 10^6 kollimierten kondensierten Atomen innerhalb von 1 s Zykluszeit im Rubidium-Quellsystem des Hannoveraner VLBAI aufzeigen.

Slagwörter: zeitlich-gemittelte optische Potentiale, Bose-Einstein Kondensate, Materiewellen-Linse

ACKNOWLEDGMENTS

An dieser Stelle möchte ich mich bei allen bedanken, ohne deren Hilfe und Unterstützung diese Arbeit wohl nicht in dieser Form existieren würde.

Ich möchte mich bei **Ernst Rasel** bedanken. Ich durfte bereits für meine Masterarbeit in Deiner Gruppe am ATLAS Experiment arbeiten. Anschließend hast Du mir die Möglichkeit gegeben meine erweckte Neugierde an der Atom Interferometrie sowie meinen Spaß am Experimentieren, Entwickeln und Tüfteln weiter zu stillen. Ich möchte mich bei Dir bedanken, dafür dass Du mir die Möglichkeit gegeben hast Teil deines wunderbaren Teams zu sein. Das Arbeitsumfeld, dass Du und auch **Wolfgang Ertmer**, am Institut für Quantenoptik geschaffen habt, ist geprägt durch viele verschiedene tolle Menschen. Es gibt einige Eigenschaften die alle gemein haben. Neben der Freude an der Physik ist die Hilfsbereitschaft die Eigenschaft die wohl am meisten hervorsticht.
Ohne die Hilfe und Unterstützung dieser Menschen wäre diese Arbeit so nicht möglich gewesen.

Auch bei "Team ATLAS" möchte ich mich bedanken, bei allen die vor mir an diesem aufregenden Experiment gearbeitet haben und allen mit denen ich Zeit im Labor verbringen durfte. **Jonas Hartwig, Dennis Schlippert** und **Daniel Tiarks**, Ihr habt mich 2011 als HiWi ans Experiment geholt. Ich danke Euch sowie **Alexander Herbst ,Jonas Matthias, Christian Meiners, Dipankar Nath, Logan Richardson, Ashwin Rajagopalan** und **Maral Sahelgozin** für die unzähligen gemeinsamen Stunden im Labor. Es hat mir immer sehr viel Spaß gemacht und ich habe von Euch allen viel gelernt.
Logan, I have spend the most time in the lab with you. We went through a lot of problems together, but you have never lost your enthusiasm and pushed me forward. For this I want to particularly thank you.

"A good day is a day when nothing breaks!"

Wann immer ich Fragen zu theoretischen Aspekten oder Modellen hatte konnte ich das Theorie Team um **Naceur Gaaloul** um Hilfe bitten. Speziell **Sirine Amri, Robin Corgier, Florian Fitzek** und **Sina Loriani** wurden so zu meinem Lieblings Theorie-Support.

Zur Auswertung, Modellierung und Darstellung der Daten dieser Arbeit habe ich in erster Linie Python genutzt. Die Grundlagen dieser Sprache hat mir **Etienné Wodey** in einem Python Crashkurs, im ICE auf der Rückfahrt von der DPG Tagung in Heidelberg, beigebracht. Ich bin Dir dafür sehr dankbar, merci!

Ohne die zahlreichen Korrekturen und Unterstützung von sowie Diskussionen mit meinen Kollegen **Sven Abend, Holger Ahlers, Sebastian Bode, Robin Corgier,**

Alexander Herbst, Waldemar Herr, Maike Lachmann, Ashwin Rajagopalan, Ernst Rasel, Dennis Schlippert, Christian Schubert, Torben Schulze, Knut Stolzenberg und **Dorothee Tell** wäre diese Arbeit nicht das, was sie ist. Danke!

Dennis, Du wurdest zwar schon mehrmals genannt, ich möchte Dir jedoch einen extra Dank aussprechen. Seit ich als HiWi bei ATLAS angefangen habe standest Du mir mit Rat und Tat zur Seite. Ich habe dabei immer deine direkte Art und die klare Kommunikation geschätzt. Wenn meine Motivation am Ende war konntest du sie meist wieder aufleben lassen. Du hast dir immer Zeit genommen um Probleme, Ideen und Erfolge zu diskutieren und mich zu unterstützen. Ich habe dadurch von dir unglaublich viel gelernt. Danke!

Ich danke meinen Eltern **Hermann** und **Katrin** und meiner Schwester **Kristin** für die Unterstützung und Liebe, die ich schon mein ganzes Leben von Ihnen erfahre. Meinen Großeltern **Lisa** und **Günter** danke ich, weil Ihr immer versucht alles für uns Kinder möglich zu machen.
Opa, ich weiß du hättest diese Arbeit auch gerne gelesen.

Mein größter Dank gilt jedoch **Saskia** und **Finn**. Ihr seid meine größte Motivation und Inspiration. Bei euch kann ich entspannen und Kraft sammeln. Ihr habt in den vergangenen Monaten leider viel zu oft auf meine volle Anwesenheit verzichten müssen.
Saskia, Du stehst immer hinter mir und gibst mir Halt. Ich danke dir für die wundervolle Zeit die wir zusammen erleben.
Finn, Deine Neugierde und der Drang alles zu entdecken haben mich daran erinnert warum ich Physik studiert habe. Deine Freude über die kleinen und unscheinbaren Dinge ist genau so ansteckend wie dein Lachen.

Ich liebe euch!

CONTENTS

1 INTRODUCTION 1
- 1.1 Atom Interferometry 1
- 1.2 Einstein's Equivalence Principle 2
  - 1.2.1 Testing the Universality of Free Fall with Atoms 4
- 1.3 Improving the Sensitivity of Atom Interferometers 4
  - 1.3.1 Bose-Einstein Condensates 6
  - 1.3.2 Matter-Wave Lensing 6
- 1.4 The Scope of this Thesis 8

2 TIME-AVERAGED OPTICAL POTENTIALS 11
- 2.1 The Optical Dipole Trap 11
- 2.2 Time Averaged Potentials 12
- 2.3 The GAUSSIAN 'Brush' 14

3 EXPERIMENTAL REALIZATION AND CHARACTERIZATION 17
- 3.1 Vacuum and MOT System 17
- 3.2 Detection 17
  - 3.2.1 Setup of the Absorption Detection 19
  - 3.2.2 Image Analysis 20
- 3.3 Expansion Rate and Temperature Evaluation 21
- 3.4 Optical Dipole Trap 23
  - 3.4.1 Implementation 23
  - 3.4.2 Center Position Modulation 23
- 3.5 Characterization of the Spatially Modulated Optical Dipole Trap 27
  - 3.5.1 Trap Frequencies 27
  - 3.5.2 Beam Focus Alignment 29

4 BOSE-EINSTEIN CONDENSATION IN DYNAMIC POTENTIALS 33
- 4.1 Loading of the Dipole Trap 33
  - 4.1.1 Numerical Simulation 34
- 4.2 Rapid Production of Bose-Einstein Condensates in Time-Averaged Potentials 37
  - 4.2.1 Evaporative Cooling 37
  - 4.2.2 Numerical Simulation 39
  - 4.2.3 Comparing Dynamic and Quasi Static Traps 40
  - 4.2.4 Prediction for an Advanced Scenario 43
- 4.3 Comparison with Other BEC Sources 46
- 4.4 Conclusion 47

5 MATTER-WAVE LENSING IN TIME-AVERAGED OPTICAL POTENTIALS 49
- 5.1 Scaling Approach 50
- 5.2 Experimental Sequence and Results 52
- 5.3 Conclusion 55

6 CONCLUSION 59
6.1 Current Limitations and Ways to Improve 59
6.1.1 Technical Limitations 59
6.1.2 Ways to Improve 61
6.2 Outlook 63
A APPENDIX 67
A.1 Parasitic Optical Pumping into F=2 67
A.2 2 µm Laser 68
A.2.1 Characterization of the Laser 68
A.3 Characterization of the AOM for 2 µm 69
A.4 Input Parameters for DKC Simulation 74

BIBLIOGRAPHY 77

LIST OF FIGURES

Figure 1.1 Mach-Zehnder-type atom interferometer in space time . . 2
Figure 1.2 Delta-Kick collimation 7
Figure 1.3 Atom images of initial and collimated ensemble. 8
Figure 2.1 Solutions of **equation (2.17)** 13
Figure 2.2 Beam modulation by acousto-optical modulator (AOM) . . . 14
Figure 2.3 Gaussian, and Dirac 'brush' 15
Figure 2.4 Trapping potentials 15
Figure 3.1 Vacuum system 18
Figure 3.2 Detection setup 19
Figure 3.3 Example of image evaluation 20
Figure 3.4 Gaussian- (red) and Thomas-Fermi-distribution (blue). . . 21
Figure 3.5 Time of flight measurement 22
Figure 3.6 Optical dipole trap setup 24
Figure 3.7 Center-position modulation control setup 25
Figure 3.8 Simulation of optical path 26
Figure 3.9 Trap frequency measurement 28
Figure 3.10 Trap frequency comparison of measurement and simulation 28
Figure 3.11 Shift of the atoms due to astigmatism 30
Figure 3.12 Trap position shift due to astigmatism 30
Figure 4.1 Atom number dependent on center-position modulation (CPM) amplitude and optical power 34
Figure 4.2 Loading efficiency and phase space density (PSD) ratio . . . 36
Figure 4.3 Evaporation process 38
Figure 4.4 Evaporation trajectories in terms of optical power and CPM amplitude 41
Figure 4.5 Evaporation measurement and simulation. 42
Figure 4.6 Comparison of Bose-Einstein condensate (BEC) sources . . 43
Figure 4.7 Loading efficiency and PSD ratio 44
Figure 4.8 Advanced evaporation simulation. 45
Figure 4.9 Comparison of BEC sources 47
Figure 5.1 Collimation by matter-wave lensing 49
Figure 5.2 Scaling during Delta-Kick collimation sequence 51
Figure 5.3 Matter-wave lens measurement protocol 53
Figure 5.4 Oscillations of expansion rate versus holding time 54
Figure 5.5 Atom number versus radial expansion rate 55
Figure 5.6 Trapping potential with AOM imperfections 56
Figure 5.7 Trap depth vs. vertical trap frequency 57
Figure 6.1 Linear potential 61
Figure 6.2 Expansion of the ensemble for different collimation trap frequencies 62
Figure 6.3 Scaling during dual species matter-wave lensing sequence . 64

Figure A.1 Pumping into F=2 67
Figure A.2 Pump rate into F=2 68
Figure A.3 Laser timeline 69
Figure A.4 Beam radius measurement 70
Figure A.5 Waist of the beam after the laser collimator 71
Figure A.6 Diffraction angle of AOM 72
Figure A.7 Beam diffraction for different frequencies 72
Figure A.8 Diffraction efficiency over frequency 73

LIST OF TABLES

Table 4.1 Optical dipole trap loading parameters 33
Table 5.1 Results of the Delta-Kick collimation 58
Table A.1 2 µm laser 68
Table A.2 Positions of beam profile measurement. 69
Table A.3 Input Parameters for the Delta-Kick collimation (DKC) Simulation 75

ACRONYMS

AOM	acousto-optical modulator
AOD	acousto-optical deflector
ATLAS	ATom LASer
AWG	arbitrary waveform generator
BEC	Bose-Einstein condensate
CCD	charge-coupled device
cMOT	compression magneto-optical trap
CPM	center-position modulation
DKC	Delta-Kick collimation
EEP	Einstein's equivalence principle
FPGA	field programmable gate array
FWHM	full width half maximum
GR	theory of general relativity
HWHM	half width half maximum
LLI	local Lorentz invariance

LPI	local position invariance
LMT	large momentum transfer
MAIUS	Matteriewelleninterferometer unter Schwerelosigkeit
MOT	magneto-optical trap
μW	microwave
ODT	optical dipole trap
PBS	polarizing beam splitter
PI	proportional–integral
PRIMUS	Präzisionsinterferometrie mit Materiewellen unter Schwerelosigkeit
PSD	phase space density
RF	radio frequency
RT	real time
TAOP	time-averaged optical potential
TAP	time-averaged potential
TOF	time of flight
UFF	Universality of Free Fall
VCA	voltage-controlled attenuator
VCO	voltage-controlled oscillator
VLBAI	Very Long Baseline Atom Interferometer
WEP	Weak equivalence principle

1

INTRODUCTION

At the beginning of the 19th century Thomas Young measured the wavelength of light with the famous double-slit experiment [1]. He explained the nature of light by undulations of the luminiferous æther by luminating bodies. This wave-like behavior of light explains the interference patterns observed in his experiment as well as the colors of thin plates. Since then light interferometers were used in numerous prominent experiments. One of the first ground-breaking results was performed with an interferometer invented by Albert Abraham Michelson [2]. The experiment was carried out by himself and Edward Williams Morley in 1887 [3]. Michelson and Morley tried to observe the aberration of light by the motion of the Earth through the luminiferous æther, which was a theoretical medium in that light propagates. They could not prove its existence. The observations attributed to the æther could sufficiently be explained by Albert Einstein's special relativity [4] without the need of an æther, but it requires the constancy of the vacuum speed of light. Nowadays light interferometers are represented in a variety of applications, for example in inertial navigation [5], telecommunication [6] or astronomy [7].

1.1 ATOM INTERFEROMETRY

In 1923 Louis De Broglie postulated the principle of wave-particle-duality of matter [8]. As a consequence particles also exhibit wave-like characteristics which form the basis for matter-wave interferometry. After the demonstration of interference of electrons in 1955 [9] and neutrons in 1962 [10] the interference of neutral atoms was shown in 1991 [11] in a Young's double-slit-like experiment. In the same year the first demonstration of sensing inertial effects with a light pulse matter-wave interferometer using laser cooled atoms was performed [12].

Since then atom interferometers have become a tool for a variety of applications [13], like the precise measurements of fundamental constants, such as the gravitational constant G [14–17] or the fine structure constant α [18–21]. Due to their sensitivity to inertial forces atom interferometers are also used to measure rotations, like the one of the Earth [22–24], the local acceleration due to gravity [25–28], or its gradient [29, 30].

The principle of an atomic gravimeter relies on coherent manipulation of an atom cloud, which is achieved by near-resonant laser light stimulating Rabi oscillations within the internal states of the atoms. During this process the momenta of the absorbed and stimulated emitted photons changes the atoms motion. By coherently splitting ($\pi/2$-pulse), reflecting (π-pulse), and recombining ($\pi/2$-pulse) the atomic wave function, a Mach-Zehnder like interferometer [31, 32] is opened. A space-time diagram of this interferometer scheme is depicted in **figure 1.1**. While operating the atom interferometer as a gravimeter the effective wave vector $\vec{k}_{\text{eff}} = |\vec{k}_1 - \vec{k}_2|$, where k_i are the wave vectors of the two irradiated Raman light beams, propagates

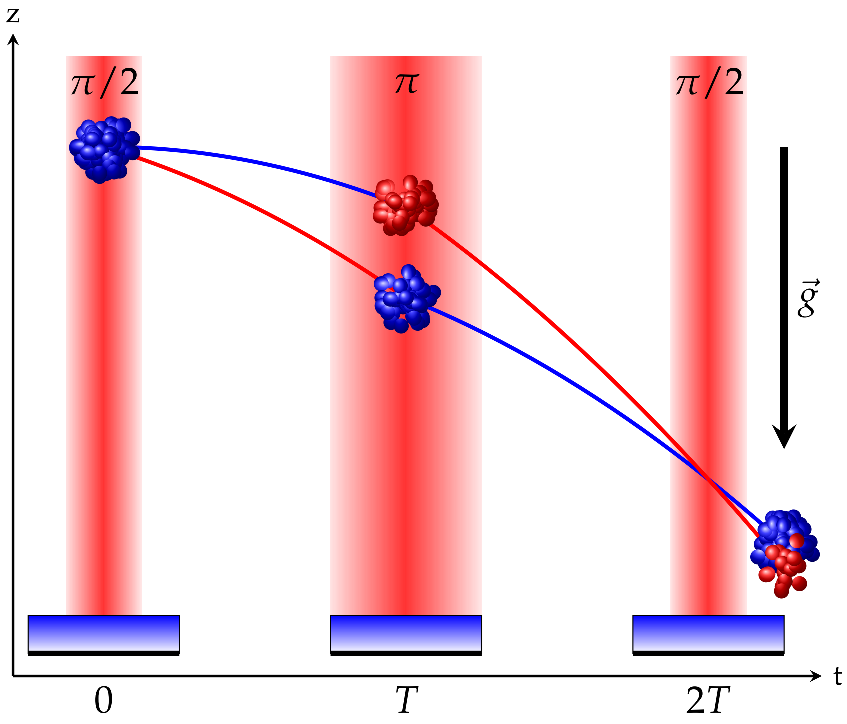

Figure 1.1: Mach-Zehnder-type atom interferometer in space time. The atomic wave packet is split ($\pi/2$), reflected (π) and recombined ($\pi/2$) by retro-reflected light fields (red vertical bars) in the direction of $\vec{g}$. During the interaction with the light field the atoms change their internal state (red and blue lines and atoms) and get an additional momentum kick.

along the direction of g. The pulses are separated by a time T. The differential phase recorded by such an interferometer depends on the acceleration in direction of beam splitting. Thus the leading phase contribution reads:

$$\Delta\Phi = \vec{k}_{\text{eff}} \cdot \vec{g} \cdot T^2. \tag{1.1}$$

Atom interferometers perform absolute measurements of the local gravitational acceleration and possess the potential to outperform their classical counterparts in terms of sensitivity, accuracy, and long term stability [33, 34].
Furthermore the differential readout of the gravity induced acceleration of two atomic ensembles paves the way for high precision tests of the Universality of Free Fall (UFF) which is one of the cornerstones of Einstein's equivalence principle (EEP).

1.2 EINSTEIN'S EQUIVALENCE PRINCIPLE

In 1916 Einstein published his work on a theory of general relativity (GR), attributing a special role to massive objects in a geometrized space-time [35]. Einstein's theory was able to explain effects like the perihelion precession of Mercury [36] or the deflection of light by massive objects [37]. One of the consequences of GR is the existence of gravitational waves [38], which were observed recently for the first time by the Laser Interferometer Gravitational-Wave Observatory (LIGO), consisting of two Michelson interferometers with 4 km long optical cavities in each arm, one

century after EINSTEIN's prediction [39].
Complementary to the direct observations of GR-effects, such as gravitational waves, stands the test of the elemental postulates of EINSTEIN's theory, one of which is the EEP [40]. It can be divided into three fundamental ideas [41]:

- **The local Lorentz invariance (LLI):**
  The outcome of any local non-gravitational experiment is independent of the velocity of the freely-falling reference frame in which it was performed.
- **The local position invariance (LPI):**
  The outcome of any local non-gravitational experiment is independent of where and when in the universe it is performed.
- **The Universality of Free Fall (UFF):**
  All bodies in a given gravitational field experience the same acceleration, independent of their inner composition.

The latter is also known as the "Weak equivalence principle (WEP)". A violation of one of the above would imply that GR is incomplete. Therefore numerous experiments have been performed testing the postulates of EEP [42, 43]. Here a closer look onto tests on the Universality of Free Fall is aimed for. The WEP states that all uncharged bodies, placed under the same conditions in space-time, will follow the same trajectory independent of their internal structure and composition. This idea was not new. Previously GALILEO GALILEI had stated this principle in the 17th century claiming that test bodies with different masses will experience the same acceleration under the same gravitational conditions [44]. Later this was generalized by ISAAC NEWTON. In the end of the 19th century LORÁND EÖTVÖS published a test of the Weak equivalence principle comparing the gravitational acceleration of different objects with different compositions in a torsion balance [45]. This resulted in a differential acceleration of the test masses smaller than 5×10^{-7}. Since then the outcome of UFF tests are quantified by the EÖTVÖS ratio:

$$\eta_{A,B} = 2\frac{g_A - g_B}{g_A + g_B}. \tag{1.2}$$

A violation will manifest in a non-zero measurement. The result of EÖTVÖS's test influenced EINSTEIN to base the theory of general relativity on the Weak equivalence principle.
Ever since the first measurements by EÖTVÖS, the torsion balance remained as a precise tool to test the Weak equivalence principle. Latest measurements have reached $\eta_{^9\mathrm{Be,Ti}} = 0.3(1.8) \times 10^{-13}$ [46].
Apart from the Lunar Laser Ranging ($\eta_{\mathrm{Earth,Moon}} = -3(5) \times 10^{-14}$ [47]) and the MICROSCOPE satellite mission ($\eta_{\mathrm{Ti,Pt}} = -0.1(1.3) \times 10^{-14}$[48]) the torsion balance is still one of the most precise classical test of the Weak equivalence principle.
Another approach is the direct comparison of the signals from two gravimeters. This is a direct analogy to the thought experiment of GALILEI. Such a classical test performed with two free falling corner cubes as independent gravimeters made of copper and uranium yielded an EÖTVÖS ratio of $\eta_{\mathrm{Cu,U}} = 1.3(5) \times 10^{-10}$ [49].

1.2.1 *Testing the Universality of Free Fall with Atoms*

In addition to tests of the Universality of Free Fall with classical objects, the field of quantum inertial sensing with atom interferometers opens new perspectives. Atom interferometers open the access to a broad range of possible test objects. These samples stand out due to their highly isotropic purity and well defined characteristics [50]. Another benefit of atoms is that it is possible to manipulate their internal and external degrees of freedom with a high accuracy. Additionally atom interferometers extend the group of possible test masses to all atomic species where laser cooling is possible. Comparisons between atom interferometers and classical gravimeters can be interpreted as semi-classical UFF tests ($\eta_{\mathrm{SiO}_2,{}^{87}\mathrm{Rb}}$ $=4.4(6.5) \times 10^{-9}$ [51]). One disadvantage of such tests is the need for two independent systems for operation and therefore a spatial separation of the two test masses.
On the contrary cold atom gravimeters in general allow for two spatially overlapping different atomic ensembles. Quantum tests of the Universality of Free Fall have been performed using: (i) two internal states of the same isotope ($\eta_{{}^{87}\mathrm{Rb}}$ $=0.9(2.7) \times 10^{-10}$ [52]), (ii) two isotopes of the same species ($\eta_{{}^{85}\mathrm{Rb},{}^{87}\mathrm{Rb}}$ $=2.8(3) \times 10^{-8}$ [53]), and (iii) two different chemical elements ($\eta_{{}^{39}\mathrm{K},{}^{87}\mathrm{Rb}}$ $=-1.9(3.2) \times 10^{-7}$ [50]). The latter was performed with the dual-species atom interferometer apparatus ATLAS (ATom LASer) in Hannover within the PRIMUS (Präzisionsinterferometrie mit Materiewellen unter Schwerelosigkeit) collaboration.

1.3 IMPROVING THE SENSITIVITY OF ATOM INTERFEROMETERS

Compared to classical tests, quantum tests do not represent the most precise probing of the UFF so far, but the method has also not reached its ultimate limitations. Regarding freely falling atoms, there are a few approaches to improve the sensitivity of atom interferometers for inertial sensitive measurements, and thus quantum tests of the Universality of Free Fall. From **equation (1.1)** follows that imparting a higher momentum onto the atoms and extending the interrogation time T improves the sensitivity.
The accuracy of phase readout of the interferometer with classical input states is limited by the quantum projection noise, which scales with $1/\sqrt{N}$. Therefore a higher atom number will also increase the possible sensitivity of quantum sensors. Apart from that the utilization of entangled input states of matter waves can undercut the quantum projection noise [54]. The rapid development in this field promises sensitivity gain of atom interferometric metrology [55, 56], such as atom clocks [57]. Currently the field of entanglement-enhanced precision measurements with atomic ensembles has started progressing from proof-of-principle experiments towards an improvement of sensitivity of real life metrological applications [54].
Regarding the momentum transfer a typical Doppler-sensitive Raman transition [12, 58], carried out by counter-propagating beam-splitting light fields, transfers momentum $\vec{p} = \hbar\vec{k}_{eff}$ to the atoms. In order to increase the momentum transfer and thereby the spatial separation of the wave function one can use sequential Raman-transitions [59], Bragg beam splitters [60], a sequence of the former two [61], or Bloch-lattices [62, 63]. These large momentum transfer beam splitters reach

multiples of the two-photon momentum $p = 2n\hbar k$. Momentum separations of up to $408\hbar k$ have been demonstrated in an atom interferometer [64].
With respect to the free evolution time T an improvement in sensitivity can be achieved by physically extending the length of the interferometry region in the apparatus such as in the case of very long baseline atom interferometers with free fall distances on the order of meters, such as the VLBAI (Very Long Baseline Atom Interferometer) facility in Hannover [65, 66]. This experiment has the potential to reach an uncertainty in the Eötvös ratio better than 10^{-13}. Another way to extend T is to perform the experiments under micro-gravity (μg) conditions. There are different approaches to provide μg conditions for atom interferometry. In facilities such as the drop tower at the Center of Applied Space Technology and Microgravity (ZARM) in Bremen, experiments can experience up to 4.7 s of μg in drop mode or 9.4 s in catapult mode [67, 68]. Weightlessness is also provided by the called EINSTEIN-elevator [69, 70]. Atom interferometry has also been performed on parabolic flights [71]. The sounding rocket mission MAIUS, which achieved the first BOSE-EINSTEIN condensate (BEC) in space [72], also performed atom interferometry during the flight [73]. All the mentioned methods provide μg times on the order of seconds or minutes. Unlimited duration in μg can be ensured by operating in space. With this perspective the Cold Atom Laboratory (CAL) has started its operation aboard the International Space Station (ISS) in 2018 [74]. This will pave the way for its successor BECCAL which will be a fully operational atom interferometry unit operating in space, possessing the potential to become the pinnacle of cold atom sensing [75].
Especially for atom interferometers operated with long interrogation times (T on the order of seconds) it is crucial to reduce the expansion rate of the atomic ensemble, to maintain the overlap of the atomic wave packets with the beam splitting light field as well as to ensure a cloud density for which detection is feasible. After trapping and sub-DOPPLER cooling the atoms, the expansion rate is on the order of $\mathrm{cm\,s^{-1}}$ ($T_{^{87}Rb} \approx \mu\mathrm{K}$). This will lead to large and dilute ensembles during detection and increases the susceptibility to systematic effects, such as wave-front distortions. Typically the reduction of the expansion rate is achieved by lowering the temperature of the ensemble by means of evaporative cooling [76, 77]. This can be performed in both, magnetic [78] and optical [79] traps. During the evaporative cooling process the mean temperature is reduced by selectively removing the hottest particles. This is achieved by lowering the effective trap depth and thus particles with energies above the threshold can escape the trap. In state selective traps the high energy particles can be coupled to a non-trapped state by means of radio frequency (RF) [78], microwave (μw) [80], or light induced transitions [81]. The advantage of these techniques is that the trapping frequency is maintained. In all cases the ensembles need to rethermalize by collisions in order to re-establish a thermally equalized distribution of their new lower energy state. The rate of collisions is dependent on the confinement of the particles in the trap. For a steep trap the rethermalization is faster than in a shallow potential. Another way is to lower the trapping potential itself [82], e.g. by decreasing the optical power of an optical dipole trap. Here the reduction of trap depth induces a relaxation of the trap confinement and slows down the rethermalization.

The evaporative cooling in the experiment described in this thesis is performed in an optical dipole trap by lowering the optical intensity and thus the trap depth. In order to overcome the reduction of trap frequency, time-averaged potentials are used to generate a dynamically controlled trapping potential which enables constriction of the confinement during evaporative cooling. This allows for rapid evaporation and fast creation of BECs [69, 83].

1.3.1 *Bose-Einstein Condensates*

After their prediction by ALBERT EINSTEIN and SATYENDRANATH BOSE in 1924 [84, 85], it took more than 70 years to demonstrate the first BEC formed with neutral atoms [86–88]. The energy distribution of BECs follows the BOSE-EINSTEIN statistics, as opposed to thermal gases which follow a MAXWELL-BOLTZMANN distribution. All particles in this condensed gas exist in the energetic ground state and share the same macroscopic wave function, thus they are indistinguishable. Quantum degenerate gases possess a variety of interesting features [89]. They present highly coherent sources, therefore they are often promoted as a matter analogy of lasers.
In atom interferometers BECs are used due to their low expansion rates, on the order of $\mathrm{mm\,s^{-1}}$ ($T_{^{87}Rb} \approx \mathrm{nK}$). This enables beam splitting by BRAGG pulses, which reach efficiencies close to 1 [67, 90]. Moreover, BECs typically feature spatial coherence across their full size [91–93]. However the time needed to generate quantum degenerate gases, mainly dominated by the duration of evaporative cooling, on the order of seconds, is long compared to standard sub-DOPPLER cooling techniques, which take a few ten milliseconds. This limits the repetition rate of devices used for precision measurements. Therefore methods to accelerate the evaporative cooling process are subject of current research.
One approach to increase the speed of BEC generation in optical dipole trap setups is the utilization of time-averaged potentials. This method is presented in this work. Due to modulation of the center position of the optical dipole trap beams the typical dependency of the trap frequency from the trap depth can be resolved. By keeping the trapping frequency high during evaporative cooling the duration of rethermalization is decreased [83].
For interferometers, with seconds of duration, expansion rates below $150\,\mathrm{\mu m\,s^{-1}}$ are required [65]. Such small expansion rates are not in reach for typically dense BECs due to mean field interactions, which pull the BEC apart. To further reduce the expansion rate of atomic ensembles matter-wave lensing [94, 95] is performed.

1.3.2 *Matter-Wave Lensing*

The basic principle behind matter-wave lensing is to reduce kinetic energy by work and thus tighten the velocity width of an atomic ensemble. Typically matter-wave lensing is performed by releasing the ensemble from the trap and turning on the trapping potential for a finite period after a certain time of flight (TOF) [96–99]. This method is known as Delta-Kick collimation (DKC), since it makes use of the Delta-Kick rotor [100]. The momentum width achievable by DKC depends on the size of the atomic cloud at the release and at the time of the collimation pulse [101]. Since

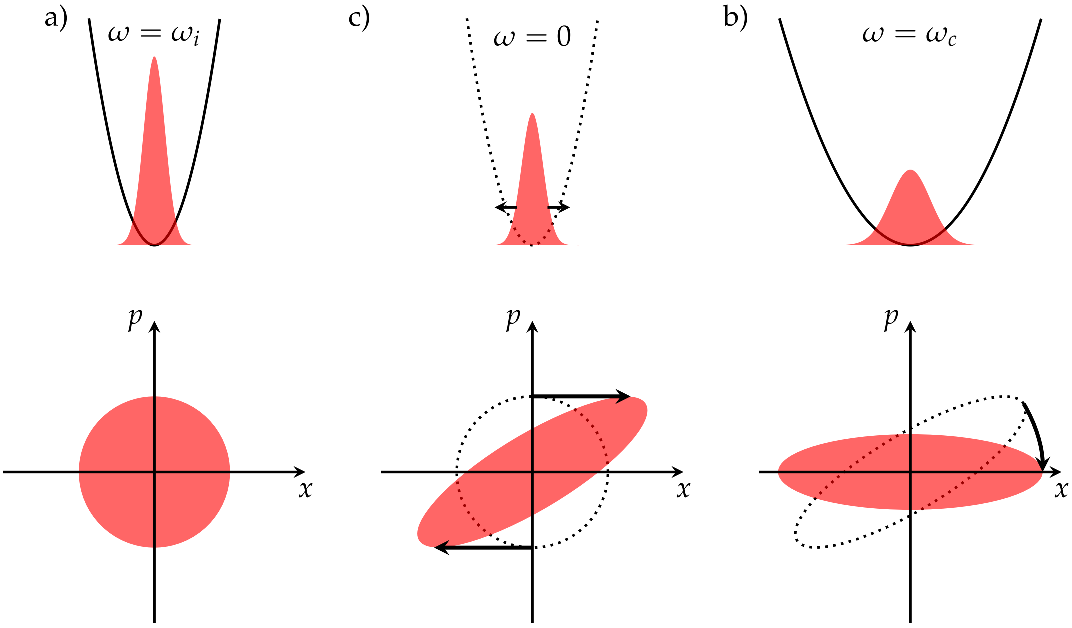

Figure 1.2: Cartoon of the Delta-Kick collimation and the corresponding phase space diagrams for each step. The sequence starts in the initial trap ω_i (a)), the distribution in phase space is equally distributed. When the trap is turned off $\omega = 0$ (b)) the ensemble starts to expand. The phase space distribution sheers since the atoms with the highest kinetic energy expand the fastest. When the collimation trap ω_c (c)) is pulsed for a certain time phase space distribution is rotated. After the rotation the momentum distribution is reduced to a minimum while the size of the atomic ensemble is large.

the ensemble will not drop out of the trapping region and long pre-kick expansion times are achievable DKC is preferably employed under μg conditions [67]. Effective temperatures below 100 pK were observed in Ref.'s [102–104] corresponding to expansion rates below $100\,\mu\mathrm{m\,s^{-1}}$.

The final momentum width achievable by DKC also depends on the harmonicity of the employed potential. Under the influence of gravity the atoms will leave the harmonic center of the trap. Therefore collimation of a freely falling ensemble requires adjustment of the position of the potentials minimum. Another approach was carried out by kicking the atoms by a vertical optical dipole potential after 1 s of expansion [101]. This yielded a residual expansion rate below $70\,\mu\mathrm{m\,s^{-1}}$ in two dimensions.

Besides DKC the expansion of the ensemble can be also lowered by instantaneously reducing the trap confinement [93, 105, 106]. This procedure is similar to the one described by Steven Chu in 1986 [94]. In this configuration the ratio of the velocity spread before and after collimation is proportional to the trap frequencies of the initial trap and the collimation potential [94]. Low trap frequencies allow for larger sizes of the ensemble and thus the typical DKC and matter-wave lenses by instantaneously lowering the trap confinement scale similarly. Especially for ground

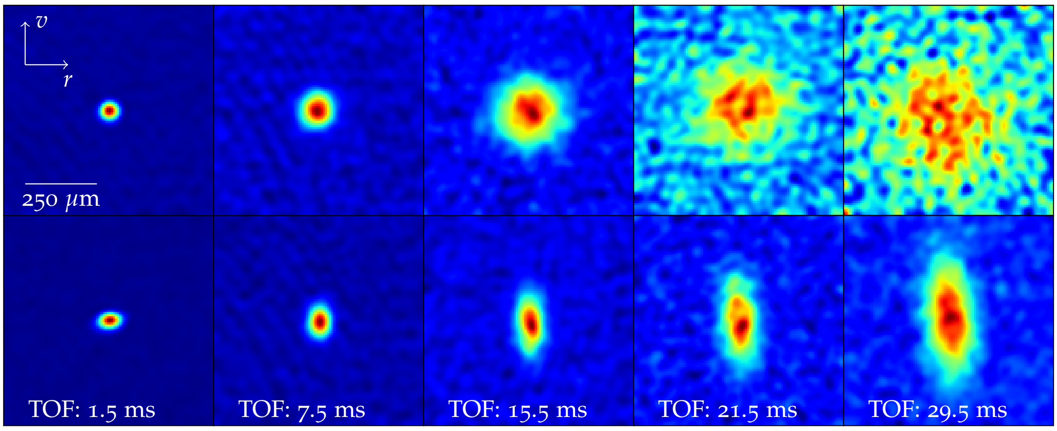

Figure 1.3: Side view of false color images of the atomic ensemble of the initial normal expansion (top) and after matter-wave lensing in two dimensions (bottom) for different TOF. The kinetic temperature of the initial ensembles is T_r =197(6) nK (T_v =181(6) nK) and the Delta-Kicked ensemble T_r =20.9(0.6) nK (T_v =134.4(3.4) nK). The images are Gauss-filtered with $\sigma = 3$.

based experiments the latter method can improve the performance by reducing the expansion of the atomic clouds to sub-nK temperatures.

1.4 THE SCOPE OF THIS THESIS

The creation and shaping of quantum states with low expansion rates, used for matter-wave interferometry, directly enhance the performance of precision measurements. For interferometers operated with large pulse separation times, the control over the expansion rate of the atomic ensembles is of paramount importance. For this, techniques such as matter-wave lensing are indispensable.

Dynamic time-averaged potentials improve the creation of BECs in optical dipole traps by accelerating the process of evaporative cooling. Beyond this they allow for matter-wave lensing in a well controlled expansion of the trap to further reduce the kinetic energy of the atomic ensemble. This thesis is organized as follows. The basic principle and theory of generating time-averaged potentials with an optical dipole trap is explained in chapter 2. Along with the description of the experiment setup the characterization of the time-averaged potential is summarized in chapter 3. Most of the measurements in this work were read out by imaging the ensemble. Therefore this chapter also covers the detection setup and image analysis. Chapter 4 shows the results of generating quantum degenerate gases and compares the performance of dynamic and quasi static traps. The outcome of these measurements are supported by theoretical models and numerical simulations. A comparison to other BEC generating experiments shows the comparability of the performance presented in this work. The implementation of matter-wave lensing is shown in chapter 5.

The performance of collimating the atomic ensemble by means of matter-wave lensing is presented over the whole temperature range reachable by evaporative cooling, from a few tens microkelvin to a few tens of nanokelvin. This thesis is concluded with the final results of BEC generation and matter-wave collimation.

This is followed by an outlook concerning possible improvements on the current apparatus. A perspective for the utilization of matter-wave lensing and DKC in future experiments is also given in chapter 6.

2

TIME-AVERAGED OPTICAL POTENTIALS

This chapter is dedicated to derive the theoretical background of time-averaged potentials. The derivation is focused on the demands of this thesis, a detailed description can be found in [83, 107]. Starting with the optical dipole trap the general idea of time-averaged potential as well as the method to derive the form of the modulation function will be explained.

2.1 THE OPTICAL DIPOLE TRAP

Optical dipole traps can be realized by focusing an intense off-resonant laser beam, the electric field **E** of this beam induces an atomic dipole moment **p** and thus leads to an intensity dependent AC-Stark shift [108]. The resulting potential is

$$U_{dip}(x,y,z) = -\frac{1}{2}\langle \mathbf{pE}\rangle = -\frac{1}{2\epsilon_0 c}\Re(\alpha) I(x,y,z) \quad , \tag{2.1}$$

were ϵ_0 is the permittivity of vacuum, c the speed of light in vacuum, and α is the complex polarizability depending on the atomic state and the frequency of the driving field[1]. The spatial intensity distribution of a beam, propagating in the direction of z, of an elliptical Gaussian beam ($w_{0,x} \neq w_{0,y}$) is described by:

$$I(x,y,z) = \frac{2P}{\pi w_x(z) w_y(z)} \underbrace{\exp\left(-\frac{2x^2}{w_x(z)^2}\right)}_{\textbf{horizontal}} \underbrace{\exp\left(-\frac{2y^2}{w_y(z)^2}\right)}_{\textbf{vertical}} \quad , \tag{2.2}$$

here P is the total optical power. The beam radius $w_i(z)$ at position z is given by

$$w_i(z) = w_{0,i}\sqrt{1+\left(\frac{z}{z_R}\right)^2} \quad , i \in x, y, \tag{2.3}$$

with the Rayleigh length

$$z_R = \frac{w_{0,i}^2 \pi}{\lambda} \quad , \tag{2.4}$$

and $w_{0,i}$ the waists at position $z = 0$[2] From **equation (2.1)** the potential depth can be determined

$$U_0 = U_{dip}(0,0,0) = -\frac{\Re(\alpha) P}{\epsilon_0 c \pi w_{0,h} w_{0,v}} \quad . \tag{2.5}$$

---

[1] A detailed calculation of the complex polarizability for the participating states of ^{87}Rb in a 2 µm trap, which was used in this thesis, was done in [109], with the resulting real part of the complex polarizabilities: $\Re(\alpha(5^2S_{1/2})) = 6.2 \times 10^{-39}\,\mathrm{C\,m^2\,V^{-1}}$, $\Re(\alpha(5^2P_{3/2})) = 32.8 \times 10^{-39}\,\mathrm{C\,m^2\,V^{-1}}$.

[2] The positions of the vertical and horizontal waists ($w_{0,i}$) can differ. This leads to an shift of the position of the trap's center, section 3.5.2.

In the case of $\Re(\alpha) > 0$ the atoms experience a force towards the center of the trap, where the intensity is the highest. For an elliptically shaped beam the dipole potential can be written as:

$$U_{dip}(x,y,z) = U_0 \frac{w_{0,x} w_{0,y}}{w_x(z) w_y(z)} I(x,y,z) \quad . \tag{2.6}$$

Therefore the shape of the potential is proportional to the intensity at each position $I(x,y,z)$ and the dimensions of the beam. For the experiments presented in this work the trap frequency plays a fundamental role. A GAUSSIAN shaped potential the center of the trap can be approximated by an harmonic function:

$$U_{dip}(x,y,z) \approx U_0 \left(1 - \left(\frac{x}{w_{0,x}}\right)^2 - \left(\frac{y}{w_{0,y}}\right)^2 - \left(\frac{z}{z_R}\right)^2 \right) \quad . \tag{2.7}$$

In the model of an classical harmonic oscillator $U_{HO}(x_i,t) = \frac{1}{2} m \omega_i^2 x_i^2$ with mass m the trap frequencies are approximated by:

$$\omega_i = \sqrt{-\frac{2U_0}{m w_{0,i}^2}} \quad , i \in x, y, \tag{2.8}$$

and

$$\omega_z = \sqrt{-\frac{2U_0}{m z_R^2}} \quad . \tag{2.9}$$

From **equation (2.8)** and **(2.9)** one can see that the trap frequencies of an unmodulated dipole trap scale with $\sqrt{U_0}$. During the process of evaporative cooling the trap depth is lowered and the hottest atoms are expelled from the trap. The remaining atoms need time, which depends on the trapping frequency, to reestablish thermal equilibrium. To uncouple this process from the trap depth time-averaged potentials,also known as painted potentials, are applied in this work.

2.2 TIME AVERAGED POTENTIALS

The time-averaged potentials are generated by modulating the center position of the initial potential $I(x,y,z)$ by $x'(t) = x - h_0 f(t)$, were h_0 is the spatial modulation amplitude of the beam and $f(t)$ is a periodic function with frequency ω_{mod} and amplitude 1. The averaged potential can be written as:

$$\tilde{I}(x,y,z) \quad = \quad \frac{\omega_{mod}}{2\pi} \int_0^{2\pi/\omega_{mod}} I(x'(t),y,z) dt \quad . \tag{2.10}$$

The modulation of the beam takes place in one dimension, such that:

$$\tilde{I}_{1D}(x) \quad = \quad \frac{\omega_{mod}}{2\pi} \int_0^{2\pi/\omega_{mod}} I(x'(t)) dt \quad . \tag{2.11}$$

For simplicity we assume a DIRAC-distribution as 'brush',

$$\tilde{I}_{1D}(x) \quad = \quad \frac{\omega_{mod}}{2\pi} \int_0^{2\pi/\omega_{mod}} I_0 \delta(x - h_0 f(t)) dt \quad , \tag{2.12}$$

where the argument of the Dirac function $\delta(x - h_0 f(t))$ denotes the mean position of the beam at time t. The beam has to spend a certain time dt at position f'. To "paint" an arbitrary function $g(f')$ the time dependent modulation function $f(t)$ has to fulfill:

$$\begin{aligned} g(f') &= \frac{\frac{df}{dt}\big|_{f=0}}{\frac{df}{dt}\big|_{f=f'}} \\ &= \frac{v_0}{\frac{df'}{dt}} \qquad (2.13) \\ \Rightarrow g(f')\frac{df'}{dt} &= v_0 \qquad (2.14) \end{aligned}$$

Here df/dt at position 0 is written as v_0, a constant velocity of the beam which is given by the modulation frequency ω_{mod} and the spatial modulation amplitude h_0. Integration of **equation (2.14)** gives:

$$\int_0^{f(t)} g(f')df' = v_0 t \quad . \qquad (2.15)$$

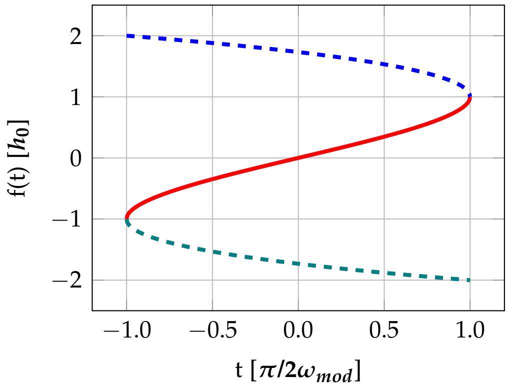

Figure 2.1: Solutions of **equation (2.17)**

One can now solve for $f(t)$ by integrating the known function $g(f')$. Like in Ref. [83] a harmonic potential is targeted, thus

$$g(f') = 1 - (f'/h_0)^2 \quad . \qquad (2.16)$$

Solving **equation (2.15)** for **(2.16)** gives:

$$\frac{f(t)^3}{3h_0^3} - f(t) + v_0 t = 0 \quad . (2.17)$$

The solutions for $f(t)$ of **equation (2.17)** are shown in **figure 2.1**. Since the center position can only be shifted in a range between $-h_0$ and $+h_0$ only the solution in which $|f(t)| \leq 1$ (red solid curve) is of physical relevance. Modulating the voltage of the voltage-controlled oscillator (VCO) in **figure 2.2** b) with a periodic repetition of $f(t)$ will lead to a harmonic averaged intensity distribution. In the direction of modulation the potential has the form:

$$\tilde{U}_{1D}(x) = U_0 + \frac{1}{2} m\omega_x^2 x^2 \quad . \qquad (2.18)$$

For $\tilde{U}_{1D}(h_0) \overset{!}{=} 0$ the trap frequency reads:

$$\omega_x = \sqrt{-\frac{2U_0}{mh_0^2}} \quad . \qquad (2.19)$$

Comparison with 2.8 shows that the frequency no longer depends on $w_{0,i}$, but on the amplitude of the center-position modulation h_0. Therefore the loss in trap

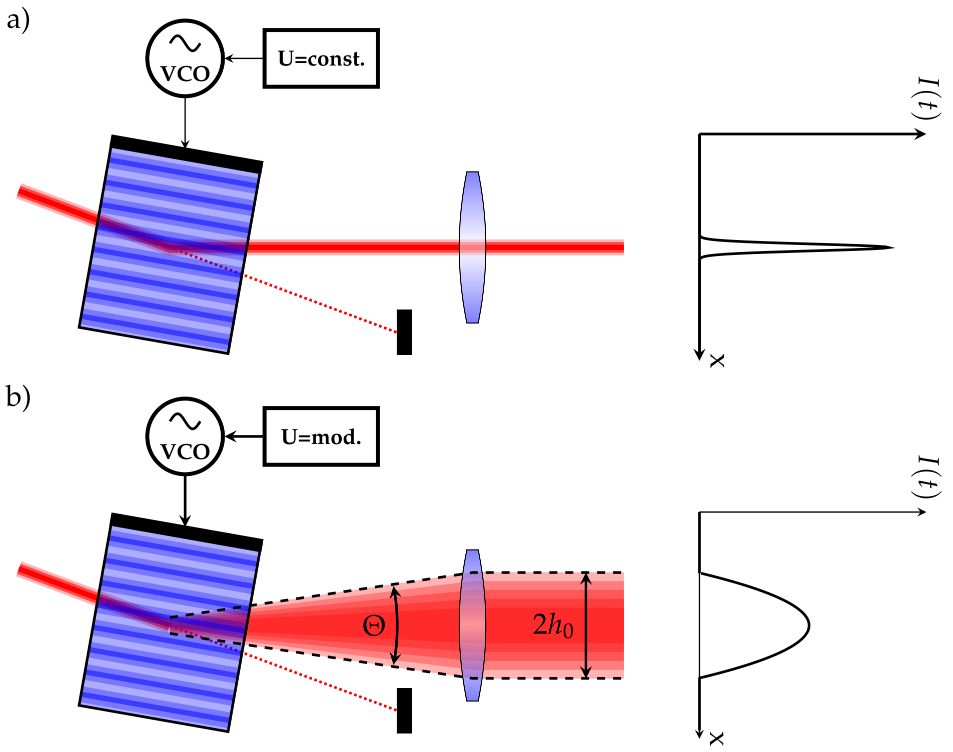

Figure 2.2: Diffraction of a laser beam in an AOM driven by a VCO, in a) for a constant voltage and in b) for a modulated voltage. The shape of the time averaged intensity profile is determined by the modulation of the VCO control voltage. The focal length of the lens and the differential diffraction angle Θ determine the width h_0 of the intensity profile.

frequency during the reduction of the trap depth can be compensated by reducing the modulation amplitude. In the setup that is described in this thesis an acousto-optical modulator (AOM) is used to generate the center-position modulation (CPM) of a laser beam (**figure 2.2**) in horizontal direction.

2.3 THE GAUSSIAN 'BRUSH'

The derivation of the time-averaged potential of the former section 2.2 was done under the approximation that the center-position modulation is acting on an ideal pencil like laser beam described by a DIRAC delta function. In our case the position modulation acts on a GAUSSIAN beam, with intensity distribution:

$$I(x) = I_0 e^{-2\frac{(x-x_c)^2}{w^2}} \quad , \tag{2.20}$$

were x_c is the center of the bell curve with width w.
The center of the beam spends a certain time dt at the position $h_0 f(t)$. The intensity distribution reads then:

$$\tilde{I}(x) = \frac{1}{\sum\limits_i g(x_i)} \sum_i g(x_i) e^{-2\frac{(x-x_i)^2}{w^2}}, \text{ with } x_i \in \{-h_0, \ldots, h_0\} \quad . \tag{2.21}$$

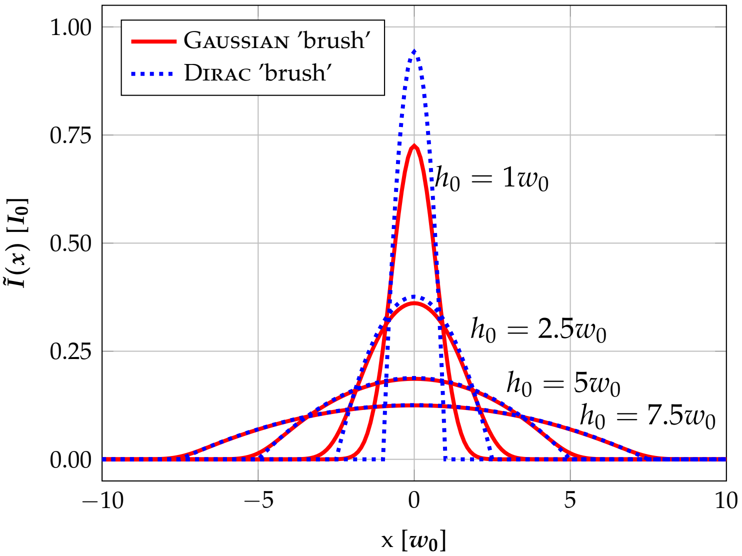

Figure 2.3: Comparison of the intensity profiles painted by GAUSSIAN and DIRAC 'brushes'.

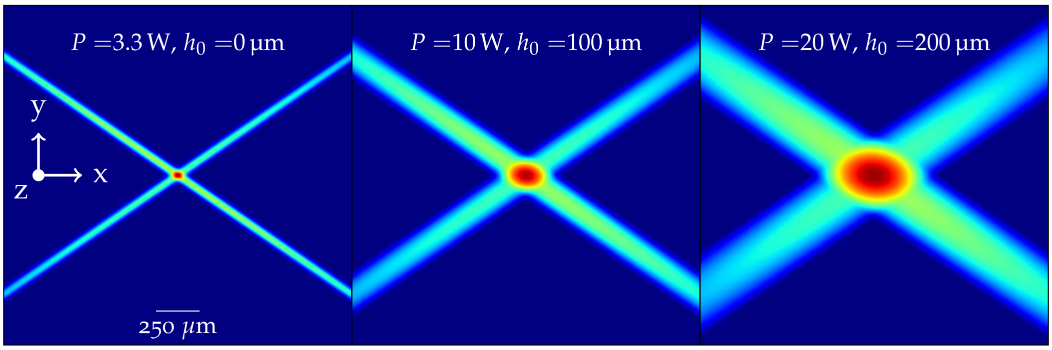

Figure 2.4: Trapping potentials for different powers and CPM amplitudes. The powers have been chosen in order to reach comparable trap depth.

Here $g(x_i)$ is given by **equation (2.16)** for a parabolic shaped trap. The positions x_i are distinct positions within the modulation amplitude. Due to the modulation of the RF-frequency of the AOM the distance between the x_i is:

$$\Delta x = x_i - x_{i-1} = \frac{dx}{d\omega}\omega_{mod} \quad . \tag{2.22}$$

It depends on the deflection efficiency $dx/d\omega_{mod}$ of the AOM and the modulation frequency ω_{mod}. A comparison of the intensity profiles given by **equation (2.12)** and **(2.21)** is shown in **figure 2.3**. For low modulation amplitudes the two intensity profiles diverge.

Therefore the horizontal part of **equation (2.2)** is replaced by **equation (2.21)**. The intensity of the time-averaged potential reads:

$$\tilde{I}(x,y,z) = \frac{2P}{\pi w_x(z) w_y(z)} \underbrace{\left(\frac{1}{\sum\limits_i g(x_i)} \sum_i g(x_i) e^{-2\frac{(x-x_i)^2}{w_x(z)^2}} \right)}_{\textbf{horizontal}} \underbrace{e^{-\frac{2y^2}{w_y(z)^2}}}_{\textbf{vertical}} \quad , \tag{2.23}$$

with $x_i \in \{-h_0, \dots, h_0\}$. The dipole beams utilized in this thesis are crossed under an angle of 70°. **Figures** 2.4 show simulated trapping potentials for different optical powers and center-position modulation amplitudes.

3

EXPERIMENTAL REALIZATION AND CHARACTERIZATION

The experiment apparatus is designed to operate two simultaneous atom interferometers using rubidium and potassium atoms. For this purpose the atoms need to be captured and laser cooled under vacuum conditions. The vacuum system as well as the laser system are shown in section 3.1.

Most of the measurements, presented in this work, rely on a precise readout of the ensemble's temperature. Those measurements of the atomic ensembles were done using absorption detection. In section 3.2 and 3.2.2 the detection system as well as the image analysis are described. To determine the ensembles temperature time of flight expansion measurements are performed. Section 3.3 describes the readout of the kinetic temperature of the ensembles.

The setup of the optical dipole trap as well as the system to generate time-averaged potentials is described in section 3.4 and characterized in section 3.5.

3.1 VACUUM AND MOT SYSTEM

The vacuum chamber consists of three major parts: The 2D-magneto-optical trap (MOT), 3D-MOT, which acts as the main chamber in this thesis, and a high aperture detection region connected via a tube below the main chamber allowing for about 20 cm of free fall. An ion getter pump `[Gamma Vacuum, TiTan-IPG, 40l/s]` and a titanium sublimation pump `[VG-Scienta, ZST23]` create and maintain vacuum conditions of about 4×10^{-11}mbar in the region of the 3D-MOT. The pressure is monitored with a cold cathode gauge `[Vacuum Generators, ZCR40R]`. All view ports are indium sealed anti-reflection coated windows. A detailed description of the vacuum system can be found in Ref. [109–111].

The laser system can be divided into three parts: The rubidium and potassium systems for cooling, trapping, and coherent manipulation of the different atomic species, and the optical dipole trap system. For this work no design changes have been done compared to the potassium system described in Ref. [110] as well as the rubidium part shown in Ref. [112].

3.2 DETECTION

Atoms exposed to resonant light will absorb and spontaneously re-emit photons. This process is used for detection. There are two different approaches. On one hand the scattered photons can be imaged and their intensity measured. The so called fluorescence detection is used in the experiment for a state selective readout of the interferometer by an photo diode `[OSI Optoelectronics, PIN-10D]` [110], but contains no information about the spatial distribution of the atomic cloud.

On the other hand detection of the atomic ensemble can be achieved using absorption imaging. For this a collimated laser beam is shone onto the atomic ensemble.

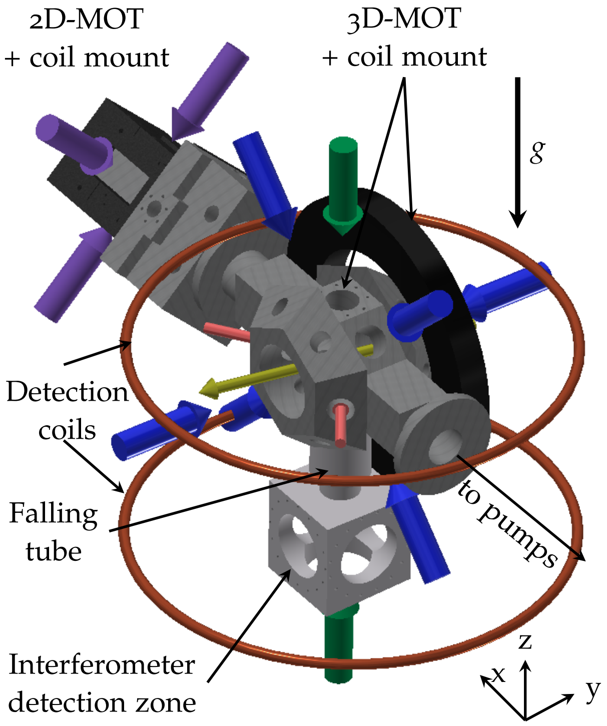

Figure 3.1: Vacuum setup with the 2D-MOT, 3D-MOT and the magnetic coil mounts. For longer interrogation times the free fall tube and the detection chamber are attached below the 3D-MOT chamber. Colored arrows indicate the axes of laser beams for the 2D-MOT (purple), 3D-MOT (blue), RAMAN and fluorescence detection beams (green) for the interferometer, optical dipole trap (ODT) (red), and the absorption detection (yellow). The detection coils are set up in HELMHOLTZ configuration to generate the quantization field for the absorption detection as well as interferometry. Modified from Ref. [110].

The atoms absorb photons and scatter them undirected. This leads to a reduction in intensity along the beams direction z' at the position of the atoms described by BEER-LAMBERT law:

$$\frac{dI}{dz'} = -n\sigma I \quad , \tag{3.1}$$

where n is the local density of the cloud and σ_{sc} the atoms' scattering cross section. The latter is given by:

$$\sigma_{sc} = \frac{\sigma_0}{1 + 4\left(\frac{\delta}{\Gamma}\right)^2 + \frac{I}{I_{sat}}} \quad , \tag{3.2}$$

with the line width Γ, the detuning δ to the atomic transition ω_{at}, and the on-resonance cross section:

$$\sigma_0 = \frac{\hbar\omega_{at}\Gamma}{2I_{sat}} \quad . \tag{3.3}$$

The saturation intensity I_{sat} depends on the polarization of the light and the orientation of the atoms to the quantization field [113]. Each measurement consists of three images: I_{bg} is taken with the laser beams turned off and is used for background subtraction.

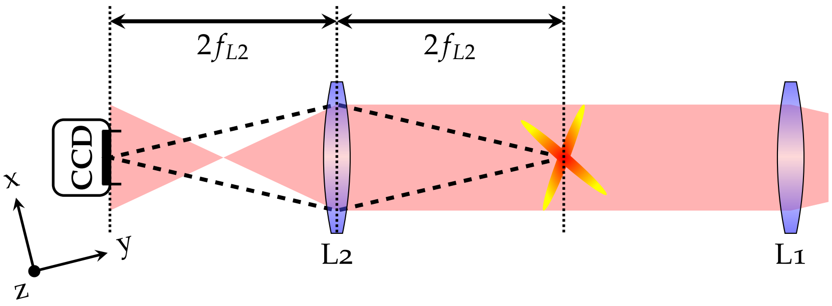

Figure 3.2: Top view of the absorption detection setup. The position of the dipole trap beams is sketched as a cross. The detection beam is sketched in red, while the shadow of the atoms is depicted by the dashed black lines.

The Images I_{atoms} and I_{beam} contain the spatial distribution of the intensity with and without atoms. The optical density at position (x, y) is given by:

$$OD(x,y) = \ln\left(\frac{I_{beam}(x,y) - I_{bg}(x,y)}{I_{atoms}(x,y) - I_{bg}(x,y)}\right) \quad . \tag{3.4}$$

From this the column density, integrated along z and in dependence of x and y, of atoms reads:

$$n(x,y) = \frac{OD(x,y)}{\sigma_{sc}} \quad , \tag{3.5}$$

integration over the illuminated area gives the atom number N.

3.2.1 *Setup of the Absorption Detection*

The detection system consists of a charge-coupled device (CCD)-camera `[Hamamatsu, C8484-15G]` and a simple $2f$-$2f$ lens setup, **figure** 3.2. The linear polarized detection light, resonant to the $|F = 2\rangle \rightarrow |F' = 3\rangle$ transition, is guided by a polarization maintaining fiber towards the MOT chamber and is collimated by lens L1 ($f = 200$ mm). In order to transform polarization fluctuations into observable intensity fluctuations the light passes through a polarizing beam splitter optimized for transmission by a $\lambda/2$ retardation wave plate The orientation of light polarization is optimized to match the vertical quantization fields axis, generated by two coils in HELMHOLTZ configuration. The detection light passes the main chamber under an angle of $-14°$. A second lens (L2, $f = 100$ mm) images the initial beam and the shadow of the atoms onto the CCD-chip. The system has a magnification of 0.881,due to imperfect distances between atoms, lens(L2), and CCD-Camera, measured by observing the free fall parabola of an atomic ensemble. The CCD-chip with an area of 8.67 mm × 6.6 mm, 1344 × 1024 pixel, has a pixel size of 6.45 µm × 6.45 µm. This results in a spatial resolution of 7.2 µm.

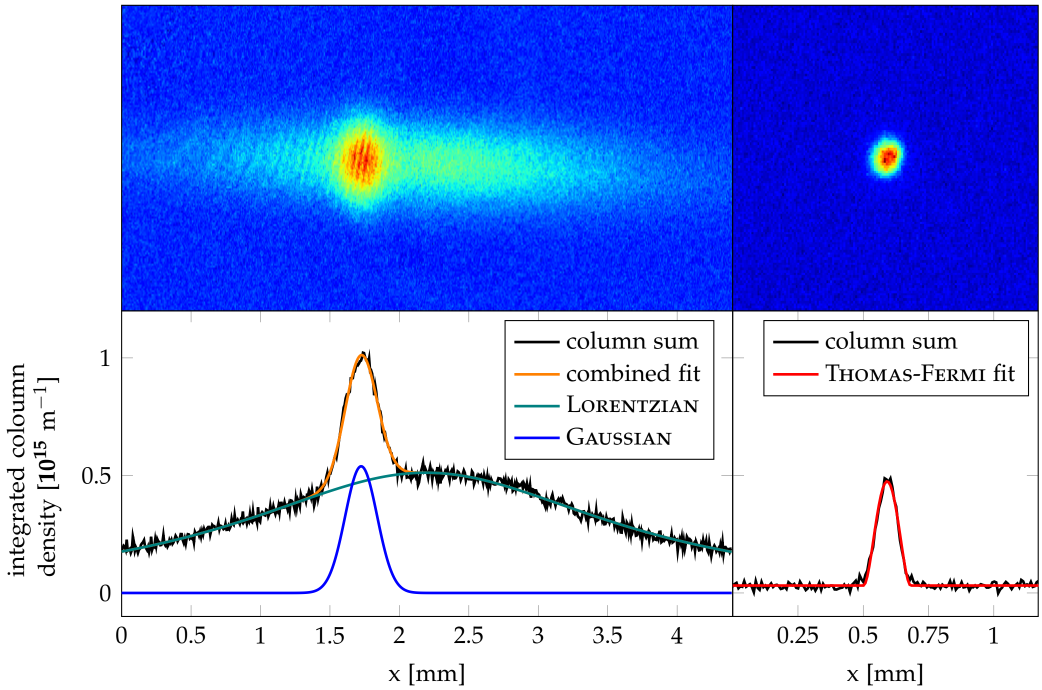

Figure 3.3: Example images in false colors of atoms in two thermal regimes (top) and their analyses (bottom). The bottom graphs exemplary show the sum over column density in x direction (black) and the fitted models (colored). On the left side density image an atomic ensemble with a temperature of about 5 µK and 1.2×10^6 atoms in the Gaussian part is shown after 5 ms of TOF. The right side image shows a BEC at about 35 nK and 4×10^5 atoms after 20 ms of TOF. A Thomas-Fermi model is fitted to the density distribution. Notice the different spatial scale of the left and right side.

3.2.2 *Image Analysis*

The spatial distribution of a thermal atomic ensemble follows a Gaussian distribution.

$$D_G(\vec{r}) = \frac{N}{\sqrt{2\pi\sigma^2}} e^{-\frac{\vec{r}^2}{2\sigma_G^2}} \tag{3.6}$$

For temperatures larger than 1 µK a strong background of atoms trapped in the wings of the crossed-ODT is visible, see **image** 3.3 (top left). To subtract this background a combination of a Lorentzian- and Gaussian-distribution was fitted to the integrated column sum. This way the Gaussian part can be extracted. For ensembles colder than 1 µK the Lorentzian background vanishes and the distribution follows a pure Gaussian distribution until the temperature is low enough to form a Bose-enhanced Gaussian distribution. Upon crossing into the quantum degenerate regime the spatial arrangement of atoms does not follow a Gaussian- but rather a Thomas-Fermi-distribution, see **figure** 3.3 (right).

$$D_{TF}(\vec{r}) = \left[\left(1 - \frac{\vec{r}^2}{R_{TF}^2}\right) \cdot \Theta(R_{TF} - |\vec{r}|)\right]^2 \tag{3.7}$$

Here $\Theta(x)$ is the Heaviside step function and R_{TF} the radius of the atomic distribution. In between a combination of the two describes the thermal atoms in the

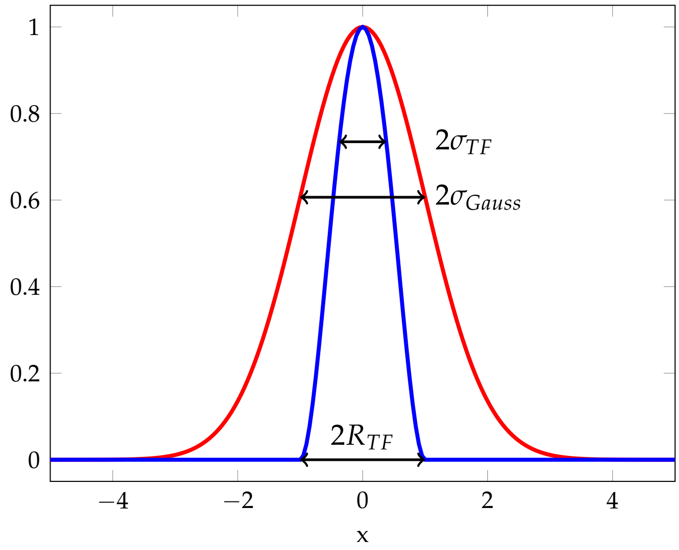

Figure 3.4: Gaussian- (red) and Thomas-Fermi-distribution (blue).

Gaussian-part and the condensed atoms in the Thomas-Fermi-part.
The width of the Gaussian distribution is defined as:

$$\sigma_G = \frac{FWHM}{2\sqrt{2\ln 2}} \quad , \tag{3.8}$$

with $FWHM$ being the full width half maximum of the curve. For the Thomas-Fermi distribution the width equivalent can be found as

$$\sigma_{TF} = \frac{R_{TF}}{\sqrt{7}} \tag{3.9}$$

from the radius R_{TF} [114].
Due to the angle of the imaging system (3.2.1) to the orientation of the optical dipole trap the projection of the x- and y-dimension had to be taken into account. This is done by rotating the measures:

$$\rho = x\cos\phi - y\sin\phi \quad , \tag{3.10}$$

where $\phi = -14°$ is the angle of detection. Since ρ is a combination of the x- and y-expanse the term 'radial' is used in the following.

3.3 EXPANSION RATE AND TEMPERATURE EVALUATION

Nearly all results in chapter 4 and 5 depend on the precise readout of the atomic ensembles' expansion rate and thus the temperature. Multiple methods exist to extract the ensemble temperature. One is to do Raman-spectroscopy of a certain transition, e.g. $5^2S_{1/2}$, $|F=1\rangle \rightarrow |F=2\rangle$, and measure the Doppler-broadening. Another way is to observe the expansion of the ensemble in a TOF-measurement.

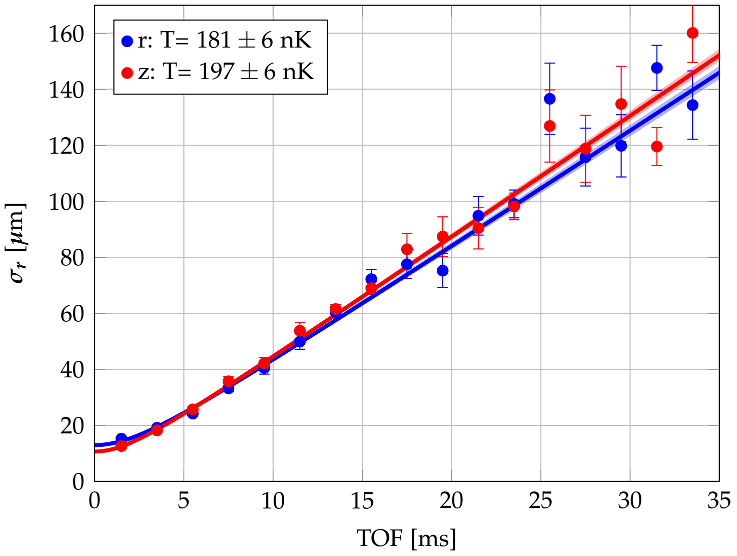

Figure 3.5: Measurement of the radius of the ensemble over time, with fit according to **equation (3.13)**.

The latter method has been used in this thesis. The expansion kinetic energy of a thermal atomic ensemble is given by

$$\bar{E}_{kin} = \frac{1}{2}m\bar{v}^2 = \frac{3}{2}k_B T \tag{3.11}$$

$$= \frac{1}{2}m\left(\sigma_{v_x}^2 + \sigma_{v_y}^2 + \sigma_{v_z}^2\right) = \frac{1}{2}k_B\left(T_x + T_y + T_z\right) \quad , \tag{3.12}$$

with m the mass of the atoms, k_B the Boltzmann constant, the velocity spread σ_{v_i}, and T_i the temperature of the ensemble in the ith direction. The time evolution of the size, due to the kinetic temperature T_i, of a freely expanding ensemble can be written as :

$$\sigma_{r_i}(t) = \sqrt{\sigma_{v_i}^2 t^2 + \sigma_{r_i,0}^2} = \sqrt{\frac{k_B T_i}{m}t^2 + \sigma_{r_i,0}^2} \quad , \tag{3.13}$$

where $\sigma_{r_i,0}$ is the initial cloud size at the time of the release ($t = 0$). For short times t the cloud size $\sigma_{r_i}(t)$ is dominated by the initial cloud size. After longer expansion times the size of the ensemble is governed by the velocity spread (**equation (3.13)**) and thus by the temperature. From **equation (3.12)** and **(3.13)** one can see that the square of the expansion rate is proportional to the temperature of the ensemble,

$$\sigma_{v_i}^2 = \frac{k_B T_i}{m} \quad . \tag{3.14}$$

Figure 3.5 shows a typical TOF measurement. Since the detection system (3.2) can image the ensemble only in two dimensions the x- and y-expansion is averaged as a radial (ρ) expansion. To get the temperature, function **(3.13)** is fitted to the measured data.

3.4 OPTICAL DIPOLE TRAP

Optical dipole trapping is performed using a thulium doped fiber laser at a center wavelength of about 2 µm `[IPG, TLR-50-1960-LP, TLR-50-1940-LP]` [1] providing output powers up to 50 W. The optical system used for the ODT is divided into three parts, the intensity stabilization and control, the beam paths towards and through the vacuum chamber, see section 3.4.1, and the modulation of the center position of the dipole trap beam by an AOM, see section 3.4.2.

To suppress intensity fluctuations of the laser source the intensity is stabilized using a Pockels cell and a FPGA (field programmable gate array) based proportional–integral (PI)-control loop directly behind the fiber output of the laser. A detailed description of this feedback loop can be found in Ref. [115]. This setup is also used to linearize the sinusoidal response of the Pockels cell and to control the optical power in the dipole trap. Around 30 W of intensity stabilized light is available in the downstream setup.

3.4.1 *Implementation*

After intensity stabilization the beam size is decreased by a telescope (f=200 mm, 150 mm) from 1.6 mm to 1.2 mm to reduce diffraction at the aperture (5.1 mm × 7.4 mm) of the AOM. The AOM is mounted on a mirror mount `[Thorlabs, KC1/M]` fixed on a rotation mount `[Thorlabs, PRM1/M]` to align the CPM horizontally. The AOM deflects up to 60 % of the light into the first diffraction order.

Figure 3.6 shows the optical setup downstream of the intensity stabilization and the beam path through the science chamber. Behind the AOM a second telescope (L1 ($f_1 = 100$ mm) and L2 ($f_2 = 300$ mm)) is enlarging the beam while the distance between L1 and the AOM is $d_{\text{AOM,L1}} = f_1$ to allow for a parallel shift of the painted beams in the chamber. The light is guided by a periscope (M1 and M2) to, and focused by lenses L3 and L5 at the center of the main chamber. For precise adjustment these lenses are situated on µm translation stages `[Neport, M-423 & SM-25]`. In order to generate a dipole trap consisting of two crossed beams L4 is re-collimating the beam, and M3 and M4 redirect it to the MOT under an angle of 70° with respect to the incident beam. The recycled beam contains about 80 % of the initial power. The polarization of the initial and the recycled beams are cleaned by $\lambda/2$-retardation wave plates and orthogonally oriented PBSs `[FOCtek Photonics]` to suppress heating effects stemming from interference due to imperfect polarizations.

3.4.2 *Center Position Modulation*

The modulation of the center-position modulation of the dipole trap beams is achieved using the AOM. The modulator features a nearly GAUSSIAN resonance with a center frequency of 99 MHz and a bandwidth of 4.65 MHz half width half maximum (HWHM). The AOM is modulating the position of the beam with a diffraction angle

---

[1] Over the course of the measurement campaign described in this thesis, the IPG laser originally envisaged for this project failed several times and had to be sent in for repair. During the repair dead time, the second laser was used.

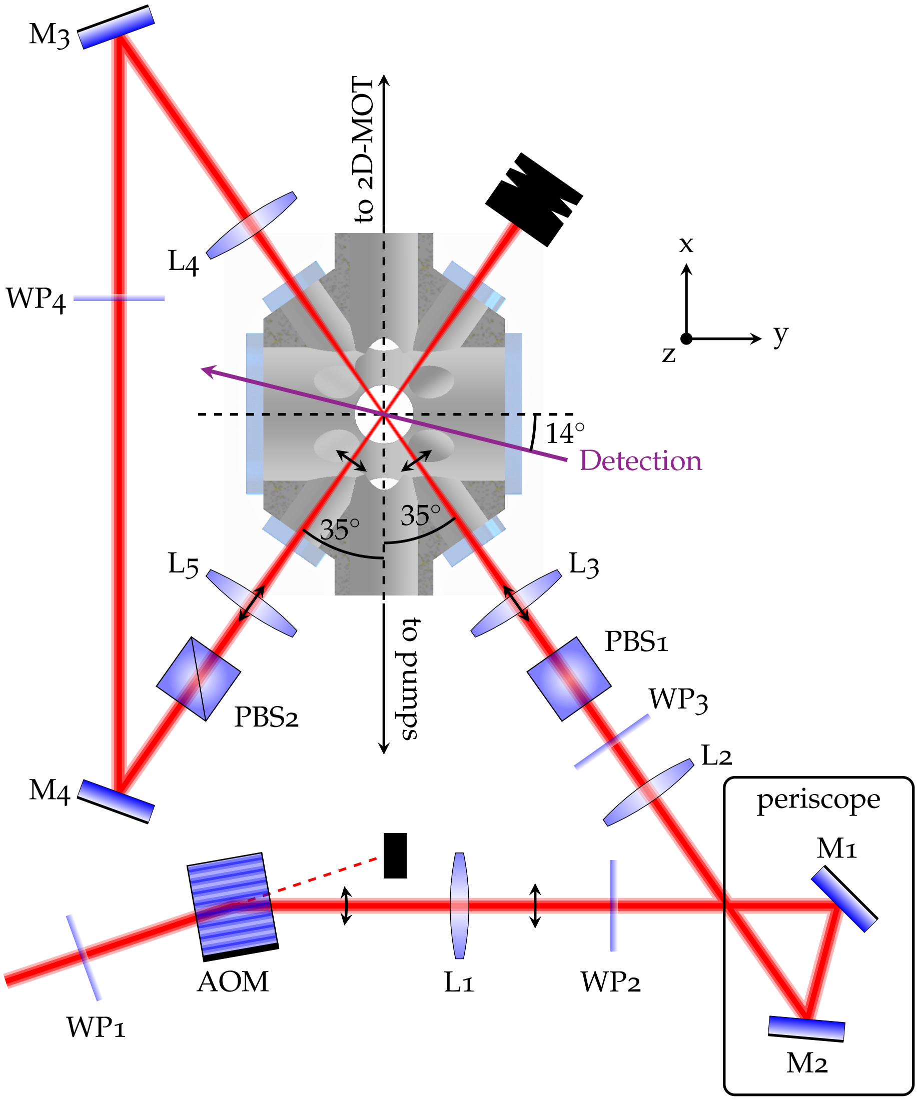
M3
to 2D-MOT
L4
WP4
x
y
z
14°
Detection
35°
35°
L5
L3
to pumps
PBS1
PBS2
WP3
L2
M4
periscope
M1
AOM
L1
WP2
WP1
M2

Figure 3.6: Optical setup of the ODT and alignment through the vacuum chamber. The AOM is used for CPM and intensity control with WP1 ($\lambda/2$) matching the polarization of the beam for best diffraction. L1 ($f_1 = 100\,\mathrm{mm}$) and L2 ($f_2 = 300\,\mathrm{mm}$) magnify the beam radius to about 3 mm, 4 mm (vertical, horizontal). L3, L4, and L5 ($f_{3,4,5} = 150\,\mathrm{mm}$) focus, re-collimate and re-focus the beam into the center of the chamber. WP3, WP4 ($\lambda/2$), and WP2 ($\lambda/4$) set the polarization for maximum transmission at the orthogonally oriented polarizing beam splitters (PBSs) (PBS1 and PBS2). The mirrors M1 and M2 form a periscope to guide the beam onto the level of the atoms. M3 and M4 direct the beam a second time through the chamber. The purple arrow indicates the direction of absorption detection.

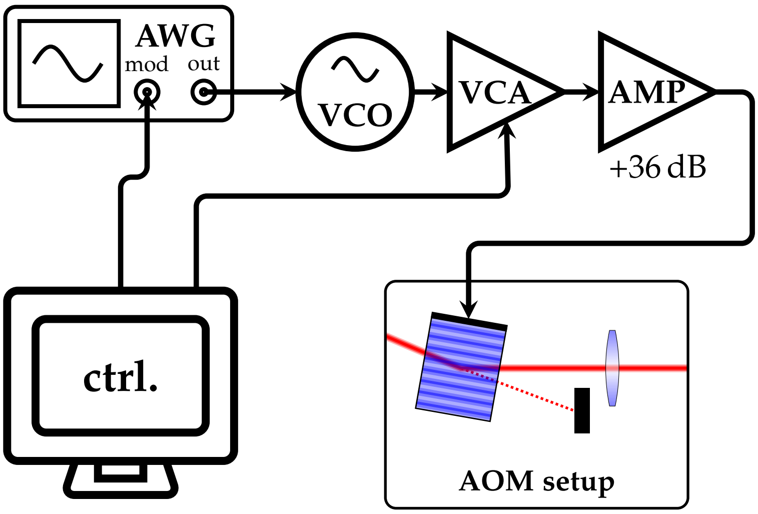

Figure 3.7: Setup of the CPM control. The amplitude of the spatial beam modulation is regulated by controlling the amplitude of the periodic function generated by the AWG.

of about $\delta\Theta/\delta f = 0.36\,\mathrm{mrad\,MHz^{-1}}$. A characterization of the AOM performance is given in appendix A.3. The signal driving the AOM is modulated with a maximum amplitude of 8 MHz. A programmable arbitrary waveform generator (AWG) `[Rigol, DG1022Z]` generates the required functions $f(t)$, as derived in 2.2. The amplitude of the displacement of the center position of the dipole trap beam, h_0, is controlled by regulating the amplitude of $f(t)$ using the modulation input port of the AWG. The output of the AWG is used to drive a VCO `[Mini-Circuits, ZOS-150+]` with a slope of $5.8\,\mathrm{MHz\,V^{-1}}$. A second stage of intensity regulation, besides the FPGA stabilization, is realized by controlling the RF-power of the AOM driving frequency via a voltage-controlled attenuator (VCA) by the real time (RT)-control, capable of linear voltage ramps. The RF-signal is amplified `[AA Opto-Electronic, AMPA-B-36, +36 dB]` to drive the AOM. The center-position modulation amplitude h_0 depends on the diffraction angle difference per frequency change $\delta\Theta/\delta f$ and the focal length of the lens used to parallelize the beam paths of different frequencies. For the simple case of just AOM and one lens, see **figure 2.2**, the amplitude of CPM after the lens can be calculated by:

$$h_0 = f_1 \cdot \tan(\Theta/2) \quad . \tag{3.15}$$

A rather simple setup, were the beams are shifted parallel and focused at the center of the trapping region, like depicted in **figure 2.2**, is not applicable in the current experiment due to limited space. In order to guide the modulated beam towards the main chamber it is necessary to change the vertical position of the beam and pass a distance of nearly 1 m. To overcome this distance three lenses are used. The first lens (L1) collimates the modulated beam propagation axes and focuses the beam at the common focal plane of L1 and L2. This leads to a re-collimation of the beam, but a focusing of the propagation axes. The final lens (L3) focuses the beam at the center of the trapping region. In an ideal setup the focal planes of the three lenses (L1-L3) would be arranged, to realize a parallel shift of the modulated beam

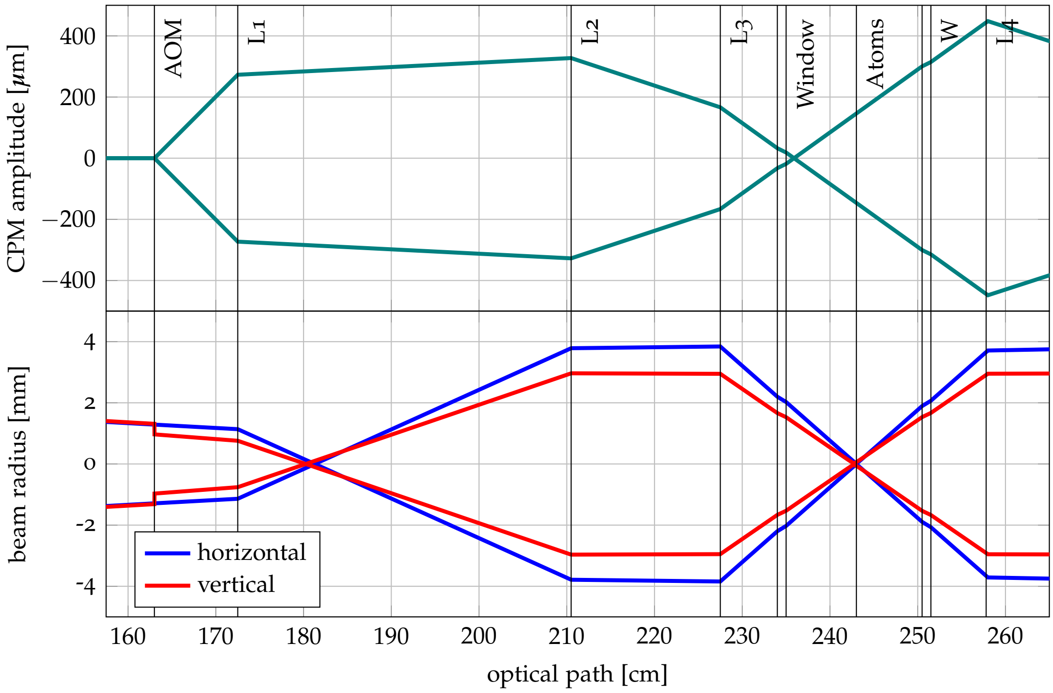

Figure 3.8: Behavior of the CPM amplitude and the beam radius in horizontal and vertical direction has been estimated using the GAUSSIAN optics. In the upper graph the zero corresponds to the unmodulated beams axis.

propagation axes. The behavior of the CPM and the beam radius in horizontal and vertical direction has been estimated using ray transfer matrices for geometrical and GAUSSIAN optics. The calculations also take imperfect distances between the lenses into account. The used input parameters are based on measurements performed on the beam shown in A.3 and A.2.1. The results are shown in **figure** 3.8. In the upper graph the zero corresponds to the unmodulated beams axis. The depicted behavior shows only the part downstream of the AOM until the first pass through the chamber. One can see that at the position of the AOM the vertical waist is reduced. To match observations this correction had to be made to the shape of the diffracted beam. It leads to a difference in waist size between the horizontal and vertical axis.

The simulation of the beam propagation also reveals, that the beam is astigmatic at the center of the trap caused by different divergences of the beam in vertical and horizontal direction, see appendix A.2.1. This leads to a separation of the position of the vertical and horizontal focus by about 2.9 mm. Section 3.5.2 explains the effect on the trapped atoms and how to overcome this complication.

In an ideal setup the propagation axes of the modulated beam would be shifted parallel. In the current setup this is not achieved, which leads to an angle of the propagation axes of the CPM beams at the position of the atoms of about 2 mrad.

The calculated waists at the atoms' position are around 25/30 µm in horizontal/vertical direction with a maximum CPM amplitude of around 165 µm. Simulations with different lens systems always aimed for the same amplitude-to-waist ratio of around 6.7.

3.4.2.1 *Choice of Modulation Frequency*

The modulation frequency ω_{mod}, **equation (2.12)**, hast to stay within lower and upper bounds. Atoms experience a time-averaged potential only if the CPM frequency of the light beams exceeds the trap frequency corresponding to the direction of the beam displacement.

$$\omega_{\text{trap}} \ll \omega_{mod} \tag{3.16}$$

For the setup shown here the maximum reachable trap frequency is on the order of $\omega_{\text{trap}}/2\pi = 2\,\text{kHz}$. During loading and evaporative cooling in the trap typical trapping frequencies do not exceed 500 Hz.
The upper boundary is set by the temporal response of the AOM, with a specified rise time of $151\,\text{ns}\,\text{mm}^{-1}$. This leads to a rise time of about $\tau_{\text{rise time}} = 550\,\text{ns}$ for the given beam radius. Therefor the maximum modulation frequency supported by the AOM is on the order of 1.8 MHz.

$$\frac{\omega_{mod}}{2\pi} < \frac{1}{\tau_{\text{rise time}}} \tag{3.17}$$

Repeating the waveform $f(t)$, sec. 2.2, with a frequency ω_{mod} will lead to formation of modulation sidebands around the center frequency [116]. Thus the frequency spectrum driving the AOM will consist of distinct peaks separated by $\omega_{mod}/2\pi$. The AOM deflects the beam by $0.36\,\text{mrad}\,\text{MHz}^{-1}$. This diffraction is transformed into a center position shift of $\Delta x_{\text{cpm}} \approx 20\,\mu\text{m}\,\text{MHz}^{-1}$ by the three lens system (L1 - L3). An upper restriction for the modulation frequency is therefore:

$$\Delta x_{\text{cpm}} \cdot \frac{\omega_{mod}}{2\pi} \ll w_0 \quad , \tag{3.18}$$

with the waist of the unmodulated beam w_0. For a spacing below $w_0/10$ the upper limit for the modulation frequency is $\omega_{mod}/2\pi < 150\,\text{kHz}$.

3.5 CHARACTERIZATION OF THE SPATIALLY MODULATED OPTICAL DIPOLE TRAP

The amplitude of spatial modulation of the beams of the time-averaged optical potential is next to the optical power the lever to control the properties of the optical dipole trap. One of which is the trap frequency, which defines, next to the trap depth, the confinement of the atoms in the trapping potential. As in Ref. [117], the trap frequencies associated with the time-averaged dipole potential are measured by parametric heating of the atomic ensembles as explained in section 3.5.1
The potential minimum defines the position at which the atoms are captured. The beam astigmatism leads to different foci and waists in the transverse direction of the light beam and hence influences the time-averaged potential as discussed in section 3.5.2.

3.5.1 *Trap Frequencies*

The behavior of the trap frequencies, determined via parametric heating of the atomic ensembles, agrees well with the results of the numerical simulations of the

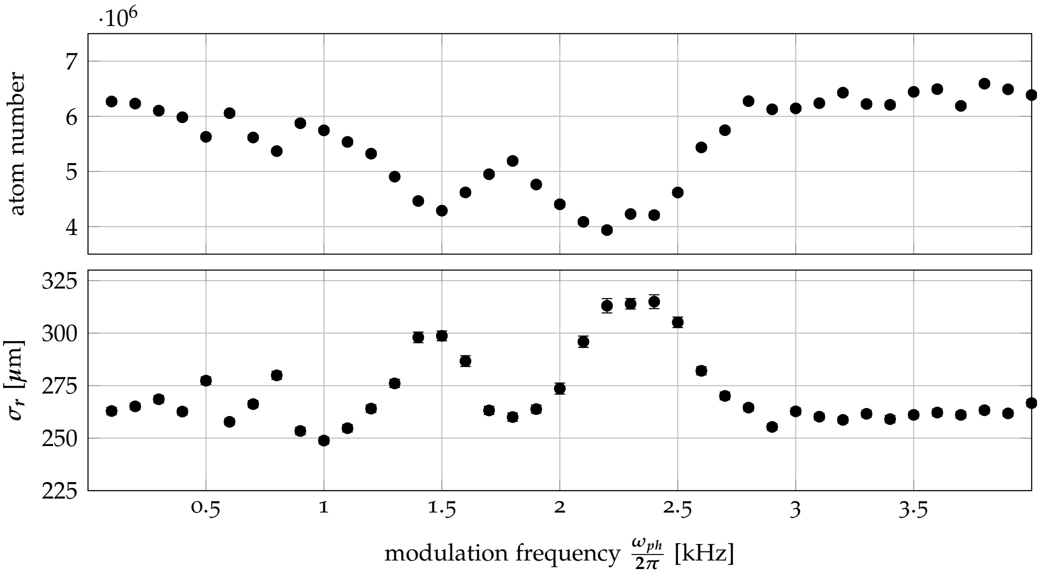

Figure 3.9: Measurement of the trap frequency for an optical power of about 3.9 W and modulation amplitude of 195 mW in the single beam configuration without CPM. The graph on top displays the atom number, while the bottom graph shows the ensemble radius in radial direction of the cloud after some TOF.

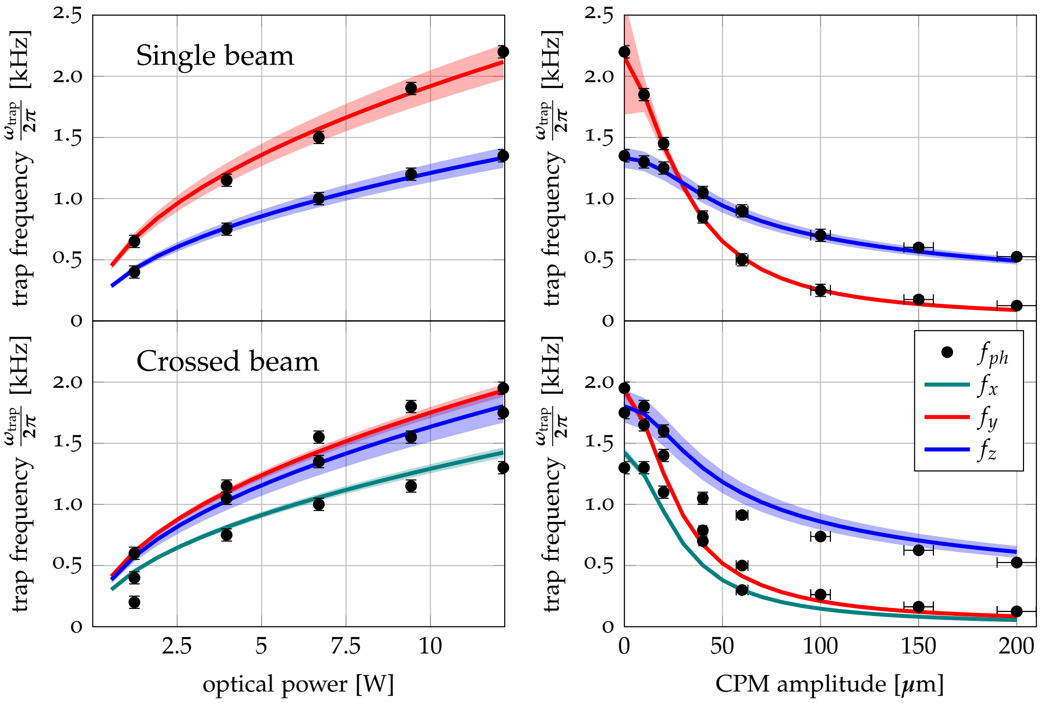

Figure 3.10: Measured trap frequencies over optical power with no CPM (left side), and amplitudes of the CPM at constant initial power (right side) for single beam trap (top) and crossed beam trap (bottom) configuration. The black dots indicate the resonances measured by parametric heating f_{ph} (e.g. fig. 3.9). The colored lines show the simulated behavior for the different trap axes with error estimation in the shaded areas.

time-averaged potential explained in 3.4.2 and set boundaries on the free parameters of this simulation. An atom at the center of the trap can be described as an 3D-harmonic oscillator with frequency ω_i. This oscillator can be excited if its potential is modulated with frequency ω_{ph} and amplitude ϵ:

$$U_{HO}(x_i,t) = \frac{1}{2}m\omega_i^2 x_i^2 \cdot \left(1+\epsilon\sin(\omega_{ph}t)\right), \quad i \in x,y,z \quad . \tag{3.19}$$

The modulation frequency has to fulfill

$$\omega_{ph} = \frac{2\omega_i}{n}, \quad n \in \mathbb{N} \quad , \tag{3.20}$$

the excitation decreases for higher n. For $n = 1 \rightarrow \omega_{ph} = 2\omega_i$ the resonance is the highest. A modulation at this frequency will lead to atom loss, and an increase in temperature of the trapped ensemble.

The trap can be modulated by varying the light intensity by steering it via the FPGA. The measurement sequence was performed as follows. The atoms are loaded (section 4.1) into the trap and held for 500 ms followed by a 200 ms modulation interval. The modulation has an amplitude of 5 % of the laser intensity. Subsequently the atoms are held in the trap for another 500 ms for rethermalization. Imaging of the ensemble is performed after 10 ms of TOF. Figure 3.9 shows an exemplary measurement of the trap frequency via parametric heating. Starting with the simple case of a single beam where the recycled beam is blocked, **figure 3.10** (a) and (b), the simulation can be adjusted to fit the measurements by approximate values for the waists ($w_{horiz.,initial} = 29\,\mu\text{m}$, $w_{vert.,initial} = 47\,\mu\text{m}$) and CPM amplitude ($h_{0,initial} = 200\,\mu\text{m}$) of the initial beam.

Repeating this method with the recycled beam unblocked, **figure 3.10** (c) and (d), leads to the waists ($w_{horiz.,recycled} = 30\,\mu\text{m}$, $w_{vert.,recycled} = 42\,\mu\text{m}$) and CPM amplitude ($h_{0,recycled} = 300\,\mu\text{m}$). For the crossed optical dipole trap case the measured values slightly differ from the simulated curves. This deviation can be explained by small vertical position drifts of the overlapping beams. This pointing instability has been observed multiple times due to performance drifts of the BEC generation. Also readout errors from the trap frequency measurements are possible due to the three overlapping resonances.

3.5.2 *Beam Focus Alignment*

The dipole trap exerts a force on the atoms towards the position of highest intensity. In a perfect optical system the vertical and horizontal focus position will be at the same point. Section 3.4.2 shows that due to different divergences of the fiber output a difference in position of the vertical and horizontal waist is likely. For the beam waists in this system, see section 3.5.1, the horizontal waist of the unmodulated beam is the most attractive, **figure 3.11** (a). Modulating the center position of the trap will artificially increase the effective waist in the horizontal direction. Therefore the vertical focus position will become the more attractive location, **figure 3.11** (b). The effect of different focus positions is shown in **figure 3.12**. To compensate this effect, one could use two orthogonal oriented cylindrical lenses in order to control the vertical and horizontal focus position separately. Another approach is to use

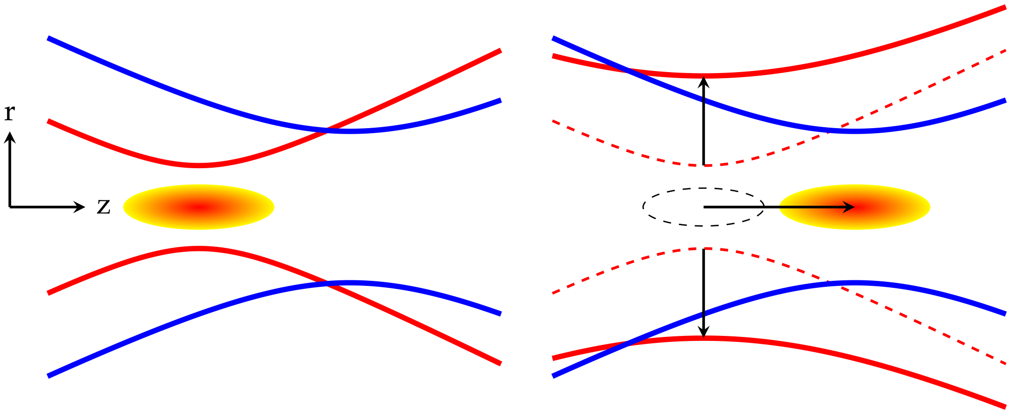

(a) Position of the atoms without CPM

(b) Position of the atoms with CPM

Figure 3.11: Shift of the atoms due to astigmatism for (a) without CPM and (b) with CPM. The solid lines depict the profile of the focused beam for the horizontal (red) and vertical (blue) direction. In (a) the atoms position is mostly confined by the horizontal focus. Artificially increasing the horizontal waist by CPM will lead to a shift of the atoms position. The dashed lines represent the profile and position of atoms for the not modulated case.

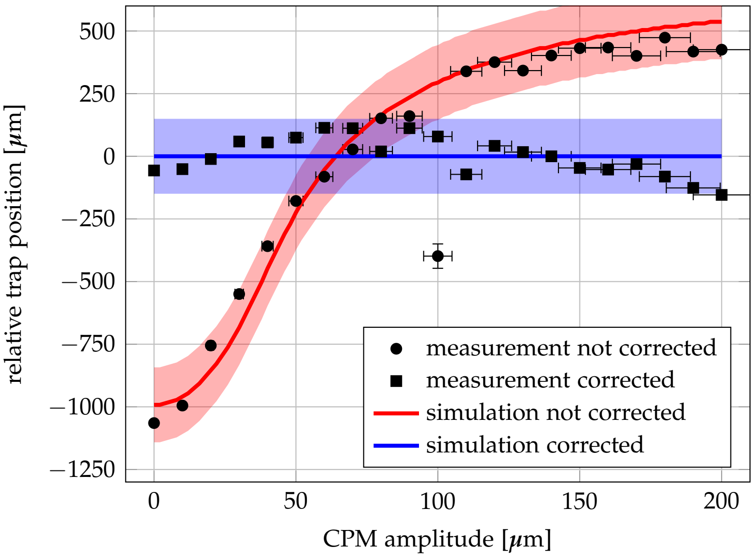

Figure 3.12: Position shift due to astigmatism. The dots are measured data, in red for the original uncorrected, and in blue for the corrected setup.The solid lines show the results from the simulation with error bars as shaded area, in red with a distance between the vertical and horizontal focus of 2.9 mm, and in blue with both foci at the same position.

the astigmatism on a lens [118], which appears if the object to image is not situated on the optical axis of the lens. In this case the image position in the sagittal plane is closer to the lens than in the meridional plane. Therefore one can correct the different focus positions caused by different divergences of the laser beam by tilting the lens. The rotation of the focusing lens (L3 **figure 3.6**) around its vertical axis by approximately 5° pulls the horizontal focus position towards the lens and overlays the vertical and horizontal focus. **Figure 3.12** shows the relative position of the atoms over CPM amplitude for the uncorrected and corrected focus alignment.

4

BOSE-EINSTEIN CONDENSATION IN DYNAMIC POTENTIALS

The generation of Bose-Einstein condensates with a large number of atoms requires an optimization of all involved phases of the experiment, starting from the magneto-optical trapping, the loading into the optical dipole trap via molasses cooling, and the final evaporative cooling. The experimental results of the latter two steps are presented in this chapter and compared with mathematical models.

One benefit of time-averaged potentials is the bigger initial trapping volume compared to unmodulated optical dipole traps, which leads to higher loading efficiencies. In Section 4.1 the number of atoms loaded into the modulated crossed optical dipole trap dependence on the optical power and center-position modulation amplitude is shown. Further it gives an insight into mode matching of the trap parameters and the atomic ensemble which allows for trap loading without phase space density (PSD) (**equation (4.8)**) loss.

The results of Bose-Einstein condensation by means of evaporative cooling in a dynamic time-averaged potential and its benefits compared to a quasi static trap are discussed in section 4.2.

4.1 LOADING OF THE DIPOLE TRAP

Prior to the loading the atoms into the time-averaged optical potential the atomic ensemble is prepared in a compression magneto-optical trap (cMOT) [119]. The influence of the MOT parameters, such as detuning and intensity of the light fields for loading the 2 µm dipole trap, have been analyzed in Ref. [109, 120].

After loading the 3D-MOT from the 2D-MOT for about 3 seconds the gradient of the MOT quadrupole field is increased by nearly a factor of two and the cooling laser jumps to a higher detuning ($\Delta_{cool} = -4.6\Gamma$). The cMOT lasts for about 20 ms and increases the density of the trapped atomic ensemble. Subsequent the quadrupole field is turned off and the cooling laser jumps to a rather high detuning ($\Delta_{cool} = -35\Gamma$) for the optical molasses for sub Doppler cooling (subD) [121]. During the whole MOT and cooling sequence the optical dipole trap is kept at a constant power

phase	duration [ms]	Δ_{cool} [Γ]	I_{cool} [I_{sat}]	I_{repump} [I_{sat}]	$\frac{\partial}{\partial z}B$ [G/m]	N, N_{ODT}
MOT	3×10^3	-2.6	31.8	0.2	510	5×10^8, —
cMOT	31	-4.6	26.9	0.09	920	4×10^8, —
subD	58	-35	31.8	0.007	0	3.8×10^8, 2×10^7

Table 4.1: Loading parameters for the optical dipole trap. The repump laser is always kept on resonance. Intensities are given in I_sat and correspond to the sum of all six MOT-beams with a radius of 1.2 mm.

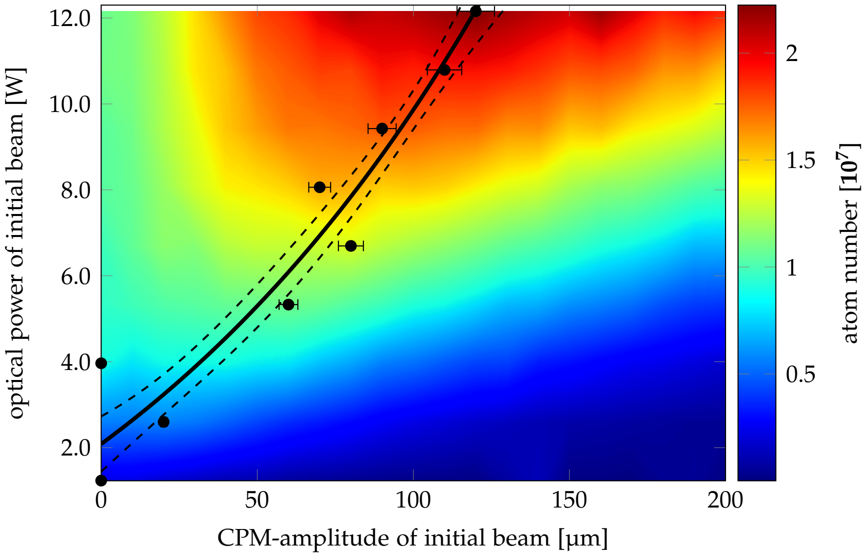

Figure 4.1: Dependency of the atom number on the center-position modulation amplitude and optical power. The black marks show the maxima of atom number per optical power. The black solid line shows an exponential regression through these points, the dashed lines indicate the 1-sigma error bar.

and center-position modulation amplitude. This leads to an accumulation of the atoms in the trap during the phase of sub Doppler cooling. The parameters used in this thesis were optimized for highest initial atom numbers in the optical dipole trap, and summed up in **table 4.1**.

The center-position modulation amplitude enlarges the free parameter space of the optical dipole trap. The number of trapped atoms was determined for different optical powers and modulation amplitudes, see **figure 4.1**. For each power the maximum atom number in dependence of the CPM amplitude was determined, black circles with error bars, which follows a exponential dependency. For maximum optical power of 12 W and a displacement amplitude of 140 µm 2×10^7 atoms are loaded into the trap.

4.1.1 *Numerical Simulation*

The experimental results were compared with an analytical model to extrapolate the possibilities of the time-averaged potential trap in terms of the loading efficiency and the PSD tendency.

Starting with a spherical, Gaussian shaped cloud of N_0 atoms (**equation (3.6)**) with a temperature T and rms radius σ_G and under the assumption that the atoms are in a thermal equilibrium, the kinetic energy of the ensemble follows a Maxwell-Boltzmann distribution [122]:

$$p(E) = 2\sqrt{\frac{E}{\pi}}\left(\frac{1}{k_B T}\right)^{3/2} e^{-\frac{E}{k_B T}} \quad . \tag{4.1}$$

Only atoms with kinetic energy lower than the trapping potential $U(x)$ at position x are trapped. Therefore the ratio of atoms loaded into the trap can be estimated using:

$$p_N = \frac{N_{trap}}{N_0} = \frac{1}{N_0} \int_{-\infty}^{\infty} D_G(x) \cdot \left(\int_0^{U(x)} p(E) \, dE \right) dx \quad . \tag{4.2}$$

This ratio is displayed in **figure 4.2** (a). The simulation is performed for an ensemble of temperature $T = 30\,\mu\mathrm{K}$ and radius $\sigma_{rms} = 150\,\mu\mathrm{m}$, which are typical values for a molasses cooled ensemble in the optical dipole trap loading sequence. While loading an ensemble into the trap the PSD can be conserved if the trap and the cloud are mode matched [89]. For a harmonic trap with stiffness κ_{trap},

$$U_{harm.}(r) = \frac{1}{2} m \omega_{\mathrm{trap}}^2 r^2 = \frac{1}{2} \kappa_{trap} r^2 \quad , \tag{4.3}$$

mode matching is fulfilled if:

$$\kappa_{trap} = \kappa_{atoms} = \frac{k_B T}{\sigma_G^2} \quad , \tag{4.4}$$

with σ_G the rms radius of the Gaussian atom distribution. A too stiff trap leads to heating of the ensemble due to non-adiabatic compression, left side of the dotted lines in **figure 4.2**. If the trap is too loose the cloud will expand non-adiabatically, right side of the dotted lines. In both cases the phase space density will be reduced. The mode match parameter (p_{mm}) can be estimated using [123]:

$$p_{mm} = \frac{8 \left(\frac{\kappa_{trap}}{\kappa_{atoms}} \right)^{3/2}}{\left(1 + \frac{\kappa_{trap}}{\kappa_{atoms}} \right)^3} \quad , \tag{4.5}$$

p_{mm} is the ratio of the PSD of the initial and trapped atomic ensemble. The outcome of **equation (4.5)** is displayed in **figure 4.2** (b) for the case of horizontal center-position modulation.

The mode match parameter p_{mm} gives an estimation how well the phase space density is conserved while loading the atomic cloud into the trap. During the evaporative cooling process the PSD is enhanced by rejecting the hottest atoms. Therefore loading a high number of atoms into a nicely mode matched trap is desirable. To find the optimal parameters of the trap in terms of atom number and mode match the product of p_N and p_{mm} is calculated as:

$$\gamma_{op} = p_N \cdot p_{mm} \quad . \tag{4.6}$$

The CPM-power interplay of γ_{op} is displayed in **figure 4.2** (c).

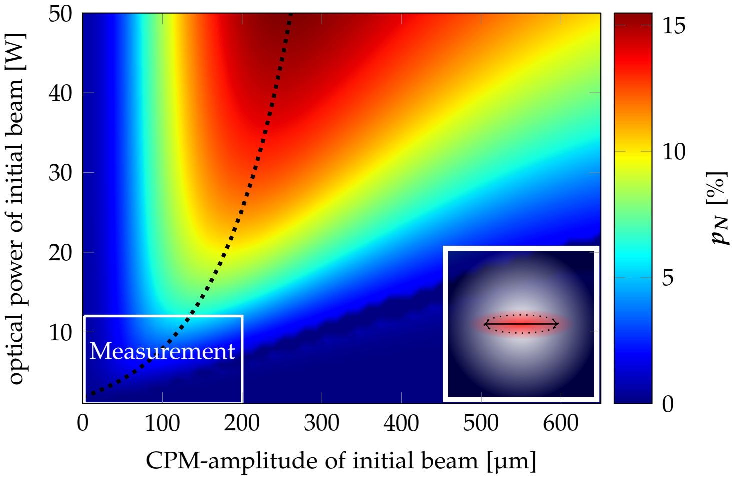

(a) Loading efficiency with 2D modulation

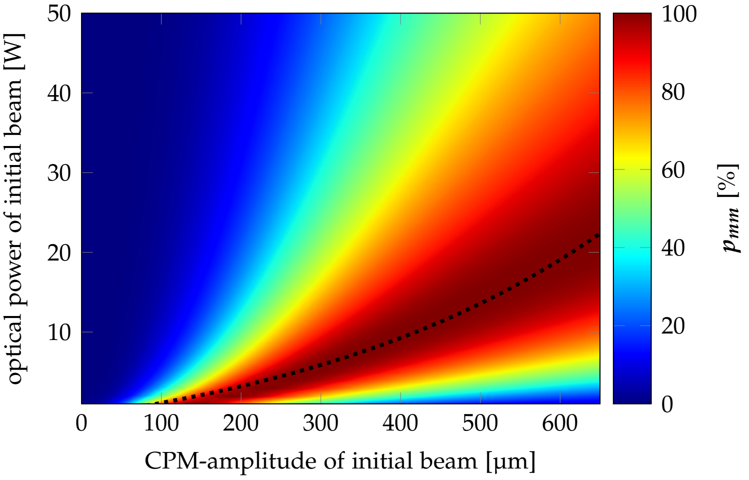

(b) PSD ratio with 2D modulation

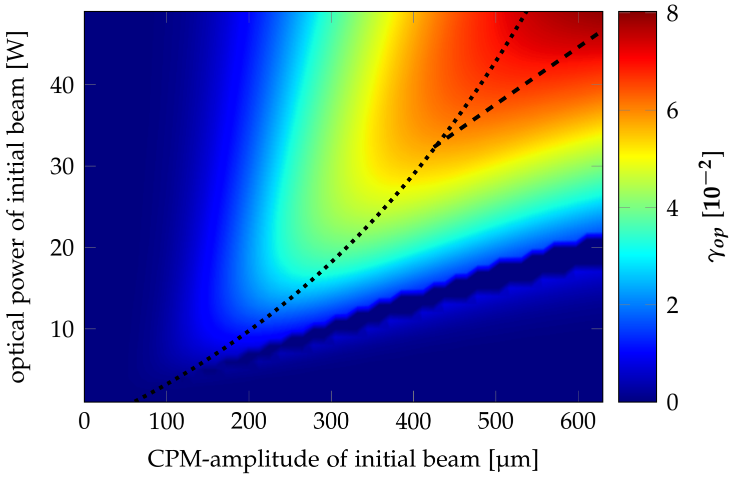

(c) Optimal loading parameter for 2D modulation

Figure 4.2: Simulation of the loading efficiency (a) and ratio of PSD before and after loading the atoms into the time-averaged potential (TAP) trap (b). The simulation is done for center-position modulation in two dimensions, represented by the inlay in the right lower corner of (a). For an initial atom number $N_0 = 4 \times 10^8$ the measurement (**figure 4.1**), surrounded by a white box, is in good agreement with the simulation of p_N. Figure (c) displays the weighted loading parameter. The dashed lines in the plots are fitted exponential curves through the maxima. In figure (c) the result differs from the exponential behavior for powers and CPM-amplitudes above 30 W and 400 µm and shows a linear behavior stressed by the dashed line.

4.2 RAPID PRODUCTION OF BOSE-EINSTEIN CONDENSATES IN TIME-AVERAGED POTENTIALS

After loading the atoms into the time-averaged potential, evaporative cooling is performed. This section includes an overview of the basic calculations needed to describe the evaporative cooling process as well as a numerical model of the time evolution of the main quantities. A full theoretical description can be found in other publications such as Ref. [89, 124, 125].

4.2.1 *Evaporative Cooling*

The DE BROGLIE wavelength of a particle in a thermal ensemble is given as:

$$\lambda_{dB} = \sqrt{\frac{2\pi\hbar^2}{mk_BT}} \quad . \tag{4.7}$$

For temperatures larger than the critical temperature ($T \gg T_c$) the distance between the atoms is much higher than the DE BROGLIE wavelength. For lower temperatures the wave functions spread further and start to overlap at the critical temperature. The density of wave functions, the phase space density, is defined as:

$$\Lambda = n_0 \lambda_{dB}^3 \quad , \tag{4.8}$$

where

$$n_0 = N \left(\frac{m\bar{\omega}_{\text{trap}}^2}{2\pi k_B T} \right)^{3/2} \tag{4.9}$$

is the peak density of a trapped atomic cloud which depends on the number of particles N and the temperature of the ensemble T, both quantities are measured via absorption imaging. The mean trap frequency $\bar{\omega}_{\text{trap}} = (\omega_x \omega_y \omega_z)^{1/3}$ is based on the simulation of the time-averaged potential, section 3.5.1. For a trapped ensemble in a pure state condensation takes place if the PSD fulfills

$$\Lambda \geq \zeta(3/2) \approx 2.612 \quad , \tag{4.10}$$

where $\zeta(x)$ is the RIEMANN zeta function[1]. The critical temperature at the phase transition is therefore given as:

$$T_c = \frac{\hbar\bar{\omega}}{k_B} \left(\frac{N}{\zeta(3/2)} \right)^{1/3} \quad . \tag{4.11}$$

In our case the trapped atoms are distributed over the m_F-manifold, resulting in three possible states. Therefore we assume the phase transition to happen at $\Lambda = 3\zeta(3/2) \approx 7.8$. Since the PSD is proportional to N/T^3 BOSE-EINSTEIN condensation can be achieved by lowering the trapped ensemble's temperature while maintaining the particle number. There are reports on direct laser cooling below the critical temperature [126–128], but the most common way is to use evaporative cooling described hereinafter.

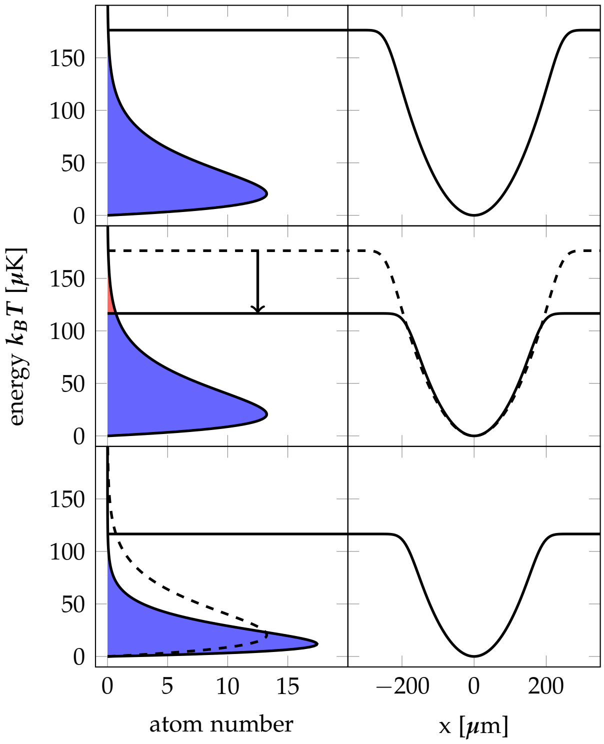

Figure 4.3: Process of evaporative cooling from top to bottom. On the left the distribution of kinetic energy and on the right the trapping potential in x direction.

The energy distribution of the atoms before condensation follows a MAXWELL-BOLTZMANN distribution (**equation (4.1)**), depicted in **figure 4.3**. Evaporative cooling is forced by the reduction of the trap depth. This leads to a truncation of the most energetic part of the distribution and expels the hottest particles. The residual atoms rethermalize and develop a distribution with a lower mean energy. Thus one can reduce the energy until nearly all atoms populate the ground state of the potential. The reduction of trap depth in optical dipole traps is done by lowering the optical power. The remaining atoms in the trap thermalize due to elastic collisions. The collision rate of this process is given by [129]:

$$\Gamma_{el} = \sqrt{2}\bar{v} n_0 \sigma_{coll} \quad , \tag{4.12}$$

were $\sigma_{coll} = 4\pi a^2$ is the collision cross section[2] and $\sqrt{2}\bar{v} = \sqrt{16 k_B T / \pi m}$ is the average relative velocity between two particles. Using the atomic density from **equation (4.9)** the rethermalization time is

$$\tau_{rt} \simeq \frac{2.7}{\Gamma_{el}} \propto \frac{T}{N \bar{\omega}^3_{\text{trap}}} \quad . \tag{4.13}$$

The factor 2.7 arises from the mean number of elastic collisions the atoms need until the gas is rethermalized [131]. One notices the rethermalization time scales with

---

[1] $\Lambda \geq \zeta(3/2) \approx 2.612$ is the solution for a ideal gas in a harmonic isotropic trap, while $\Lambda \geq \zeta(3) \approx 1.202$ is the solution for a free gas.

[2] $a \simeq 100 a_0$ is the s-wave scattering length for ^{87}Rb in the $|5^2S_{1/2}, F = 1\rangle$ state [130] with the BOHR radius of $a_0 = 5.3 \times 10^{-11}$ m

$\bar{\omega}_{\text{trap}}^{-3}$. Thus a relaxation of the trap extends the evaporation time. In a static trap, lowering the optical power reduces the trap depth and the trap frequency. Contrary dynamic time-averaged potential enable for preservation of trap frequency while lowering the potential depth.

4.2.2 *Numerical Simulation*

During the evaporation process the trap depth is exponentially reduced

$$U_{td}(t) = U_{td}(t=0)e^{-\chi t} \quad . \tag{4.14}$$

The constant χ depends on the initial trap depth $U_{td}(t=0)$, final trap depth $U_{td}(t=t_{ev})$, and the duration of evaporation t_{ev}. Following 3.4 and 3.5.1 the trap depth and frequency is simulated, and the evaporation process numerically modeled using the scaling laws given in Ref. [83, 132–134]:

$$\frac{dN}{dt} = -\left(\Gamma_{ev} + \Gamma_{3b} + \Gamma_{bg}\right) N \tag{4.15}$$

$$\frac{dT}{dt} = -\left(\frac{\Gamma_{ev}}{3}(\eta + \alpha - 3) - \frac{\Gamma_{3b}}{3} - \frac{\dot{\bar{\omega}}}{\bar{\omega}}\right) T + \frac{\Gamma_{sc} E_r}{3k_B} \quad , \tag{4.16}$$

where $\alpha = (\eta - 5)/(\eta - 4)$, Γ_{ev} is the evaporation rate, Γ_{bg} the background collision rate, Γ_{3b} the three-body collision rate, Γ_{sc} the scattering rate of photons of the optical dipole trap, E_r the recoil energy, and η the evaporation parameter. The terms in **equation (4.15)** and **(4.16)** will be discussed in the following.
The rethermalization of the truncated MAXWELL-BOLTZMANN distribution happens due to elastic collisions, which appear with the rate Γ_{el}. Therefore the evaporation rate is given by:

$$\Gamma_{ev} = \Gamma_{el}\eta e^{-\eta} \tag{4.17}$$

with the evaporation parameter

$$\eta = -U_{td}/k_B T \quad . \tag{4.18}$$

Contrary to the elastic collisions, inelastic collisions lead to atom loss and increase the temperature. The three body collisions Γ_{3b} become important for high densities while two body losses are still negligible [135]. Three body collisions occur with rates [129]:

$$\Gamma_{3b} = K_3^{nc} \frac{n_0^2}{\sqrt{27}} \tag{4.19}$$

for $T > T_c$ with $K_3^{nc} = 4.30(18) \times 10^{-29}\,\text{cm}^6/\text{s}$ and

$$\Gamma_{3b} = K_3^{c} \frac{8n_0^2}{21} \tag{4.20}$$

for $T < T_c$ with $K_3^c = 5.80(19) \times 10^{-30}\,\text{cm}^6/\text{s}$ for ^{87}Rb .
The background collisions Γ_{bg} are one body collisions and arise from collisions

with the background vapor. They are independently determined by a lifetime measurement to be

$$\Gamma_{bg} = \frac{1}{\tau_{lt}} \tag{4.21}$$

with $\tau_{lt} = 30\,\mathrm{s}$.
The term $(\dot{\bar{\omega}}_{\text{trap}}/\bar{\omega}_{\text{trap}})T$ describes the temperature change due to compression or relaxation of the trap.
The final term in **equation (4.16)** stands for heating due to reabsorption of scattered photons from the trapping laser. The intensity dependent scattering rate is given by

$$\Gamma_{sc} = \sum_i \frac{U_0 \Gamma_i}{\hbar \delta_i} \quad , \tag{4.22}$$

were Γ_i are the line width of the atomic transitions and δ_i the detunings of the trapping laser to the transitions. **Equation (4.22)** is simplified under the assumption that the atoms are located in the center of the trap and experience the peak intensity. The scattering rate is summed over all possible transitions of the D_1-, and D_2-lines. For the 2 µm dipole trap the heating rate due to the scattered photons at the beginning of the evaporation process, trap depth of 100 µK, is on the order of about 10 nK/s. Hence the effective heating during evaporation is negligible. For traps operated closer to resonance, eg. 1 µm, and higher optical powers, trap depth 1 mK, the effect can rise to the order of hundreds of nK/s and becomes non-negligible.

4.2.3 *Comparing Dynamic and Quasi Static Traps*

In this section a direct comparison of the evaporative cooling performance of a dynamic and a quasi static trap is given. In order to have comparable starting conditions both settings begin with a modulated trap, $h_0 = 140\,\mu\mathrm{m}$. In the quasi static trap the modulation is kept on a constant level while in the dynamic case the modulation amplitude is reduced exponentially in time. The trajectories of the CPM-amplitude to the optical power is depicted in **figure 4.4**. For every trap depth (a) on the evaporation trajectory the trap frequency (b) is known. The black line in **figure 4.4** shows the trajectory with the best trap frequency preservation.
After loading the optical dipole trap the atoms are kept for about 500 ms to allow for thermalization and spontaneous evaporation. The holding time was experimentally optimized for highest PSD and yields $\Lambda \approx 5 \times 10^{-4}$. Then evaporative cooling is forced by lowering the trap depth.
The main quantities of the time evolution are depicted in **figure 4.5** for two data sets. One of which was taken with a dynamic trap, the other in a quasi static trap configuration. Both result in a BEC of about 2×10^5 condensed atoms, but the dynamic trap in a shorter time. The Evaporation has been performed for different χ, see **equation (4.14)**, in order to test the time dependency of the evaporation efficiency for dynamic and quasi static traps, see **figure 4.6**.

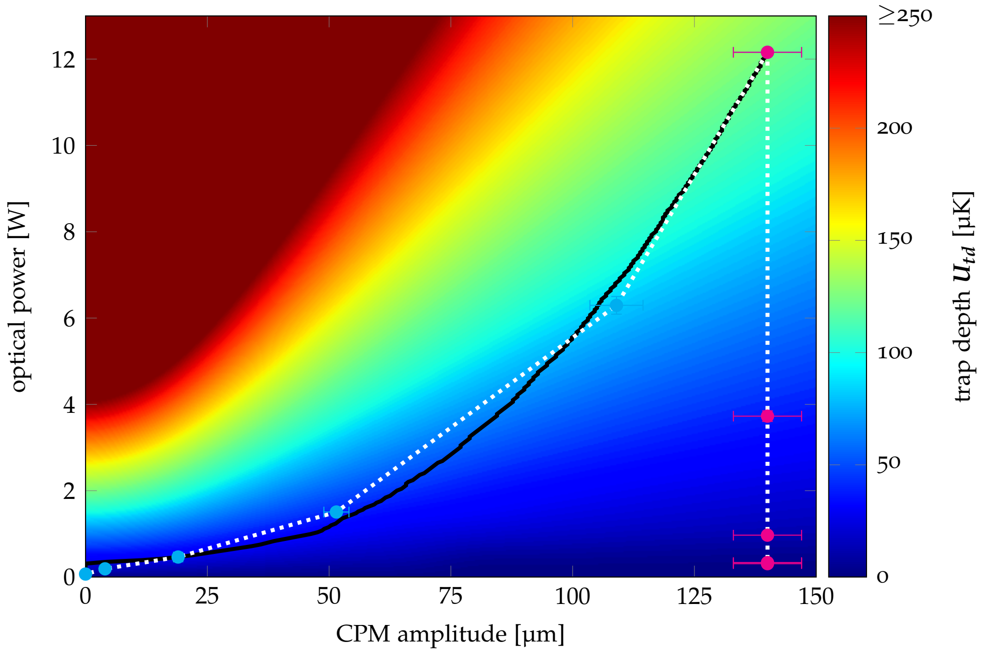

(a) Trap depth

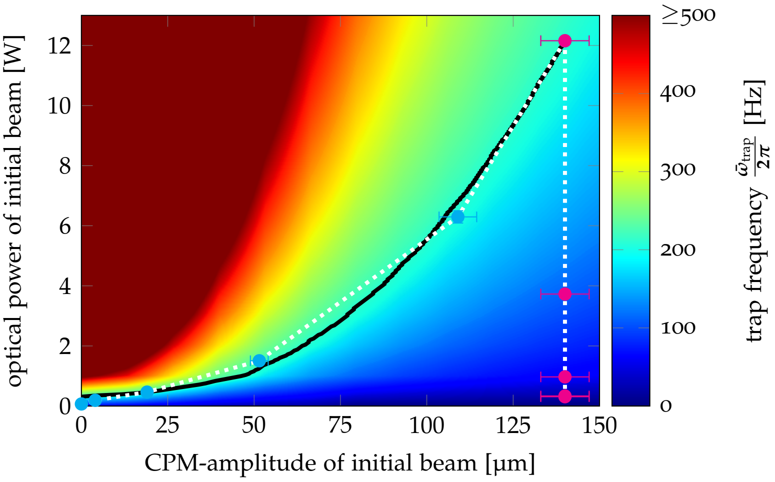

(b) Trap frequency

Figure 4.4: Trap depth (a) and trap frequency (b) and the evaporation trajectories in terms of optical power and CPM amplitude for the dynamic trap (cyan color), the quasi static trap (magenta color), and the optimized trajectory (black) with the lowest variation of the trapping frequency.

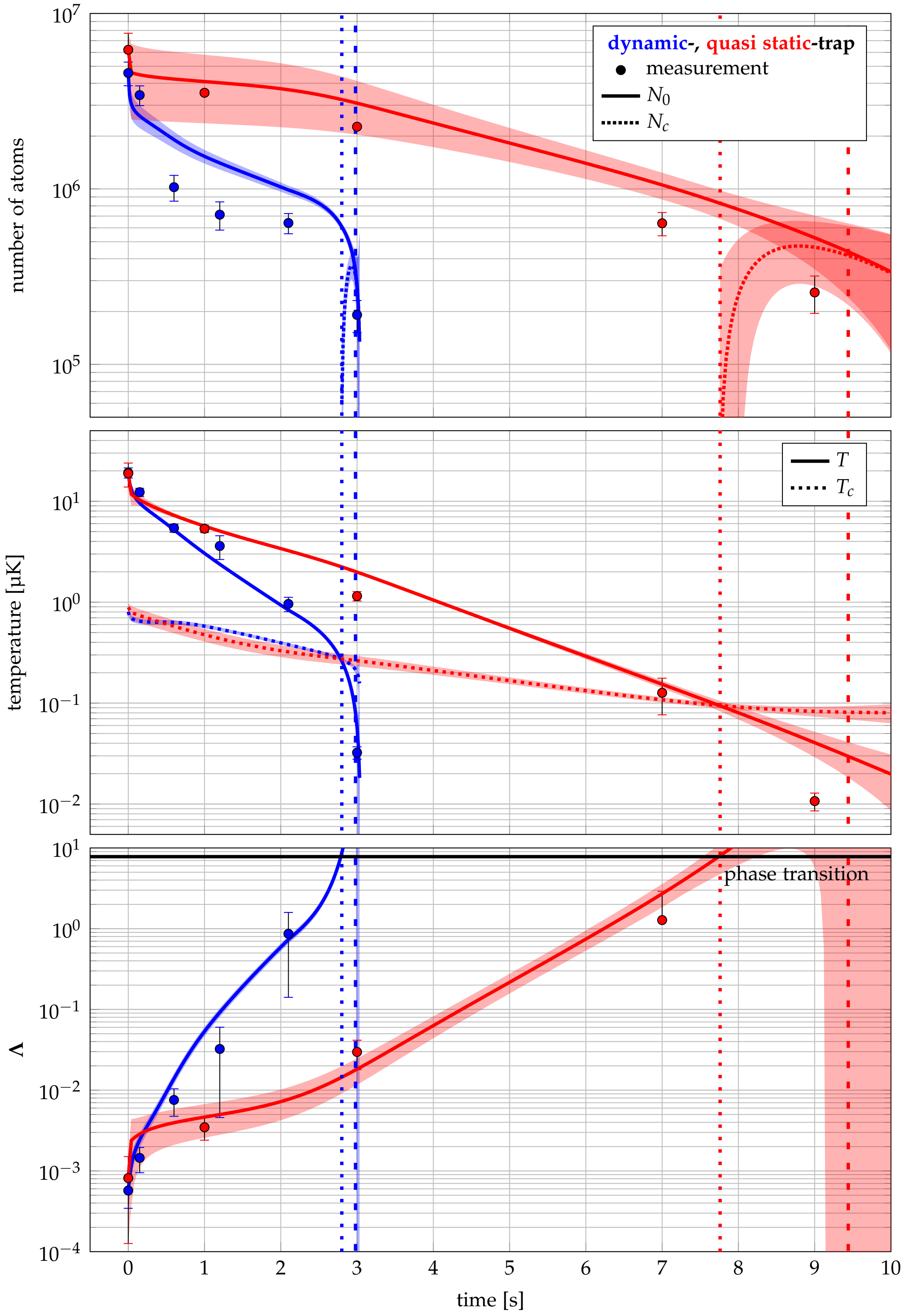

Figure 4.5: Comparison of the numerical simulation (solid lines) and measurements (data points) of evaporative cooling over time for a dynamic (blue) and a quasi static (red) trap. The shaded areas correspond to a one-sigma error estimation. The top graph displays the atom number. The temperature evolution is shown in the center as well as the critical temperature (dotted lines). At the bottom graph the PSD is displayed. The black solid line marks the critical PSD at which the phase transition occurs. The time of the phase transition is marked by the dotted line, while the dashed line shows the time where the quasi pure BEC ($N_c/N_0 > 0.95$) occurs for the dynamic (blue) and the quasi static (red) trap.

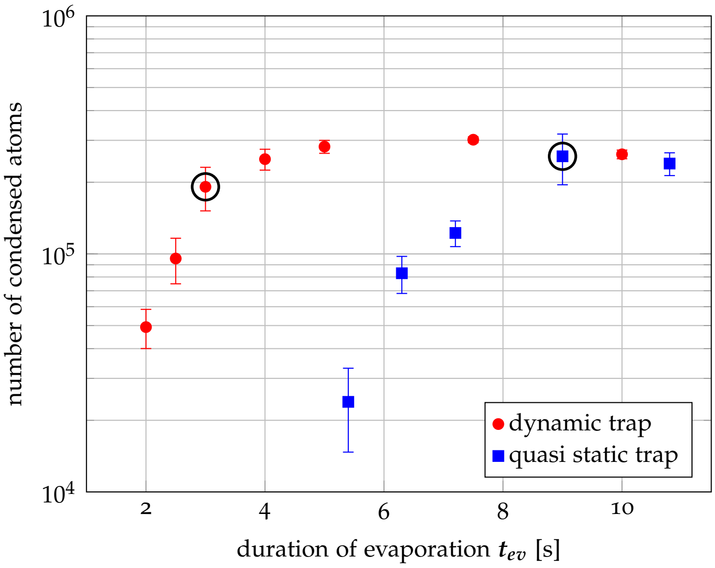

Figure 4.6: Comparison of the BEC performance of the dynamic and quasi static trap. Circles mark the two cases compared in the previous sections.

In order to quantify the purity of the BEC the ratio of condensed atoms can be estimated by [136]:

$$\frac{N_c}{N_0} = \begin{cases} 1 - \left(\frac{T}{T_c}\right)^3 & , T < T_c \\ 0 & , T > T_c \end{cases} \tag{4.23}$$

In order to reach the nearly pure BEC ($N_c/N_0 > 0.95$) only the final ramp step was optimized in terms of optical power.

Over the course of optimizing the experimental parameters for efficient BEC production it was even possible to generate quasi pure BECs with up to 4×10^5 atoms within 5 s of evaporation. This result is marked with (3) in **figure** 4.9.

4.2.4 *Prediction for an Advanced Scenario*

Supported by the results of this chapter a new setup is build up as a ^{87}Rb source system for the VLBAI experiment [65, 66]. It will operate with a 1064 nm optical dipole trap laser with up to 50 W. The center-position modulation for the time-averaged potential is generated by an acousto-optical deflector yielding modulation amplitudes of about 1 mm in two dimensions. Using a crossed optical dipole trap with 2D-modulated beams enables the control of the trap parameters in all three dimensions. Preliminary studies of the system show that it is possible to load the MOT with above 10^9 atoms within 200 ms.

The simulation result of the 3D modulated trap is displayed in **figure** 4.7. For a molasses cooled ensemble with 10 µK and a *rms* radius of 500 µm it is possible to load above 2.5×10^8 atoms into the trap assuming a moderate optical power of 25 W and a modulation amplitude of 600 µm. While this are the best parameters to load the time-averaged potential the trap frequencies are low. This effects the rethermalization rate and slows down the evaporative cooling sequence. Therefore

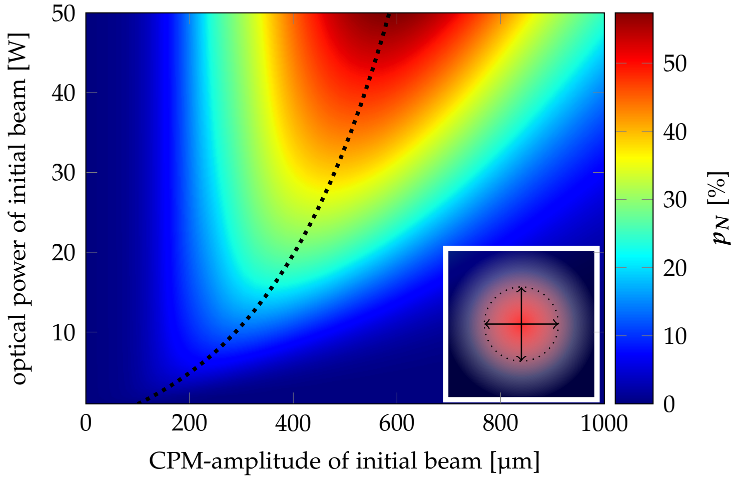

;

(a) Loading efficiency with 3D modulation

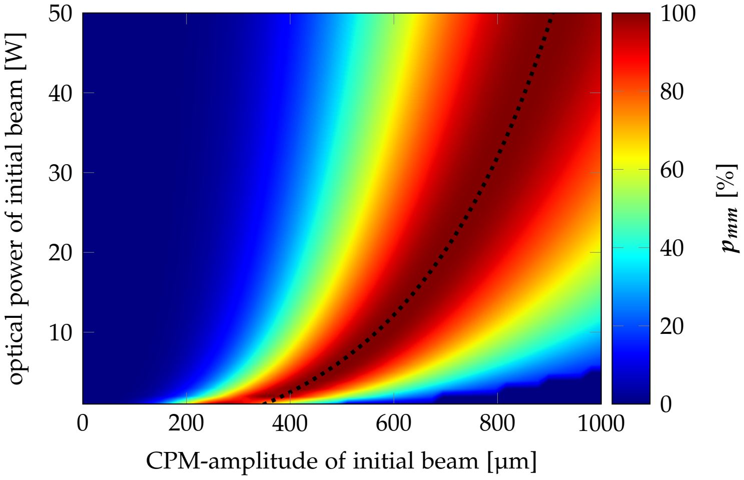

(b) PSD ratio with 3D modulation

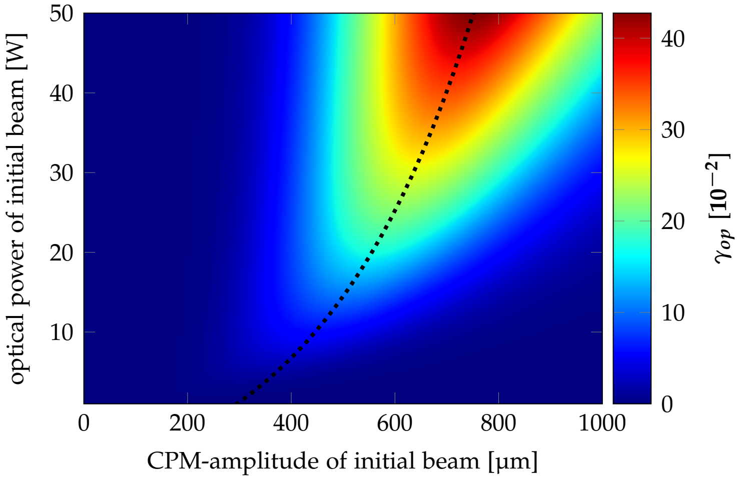

(c) Optimal loading parameter 3D modulation

Figure 4.7: Simulation of the loading efficiency (a) and ratio of PSD before and after loading the atoms into the TAP trap (b). The simulation is done for center-position modulation in three dimensions, represented by the inlay in the right lower corner of (a). Figure (c) displays the weighted loading parameter. The dashed lines in the plots are fitted exponential curves through the maxima.

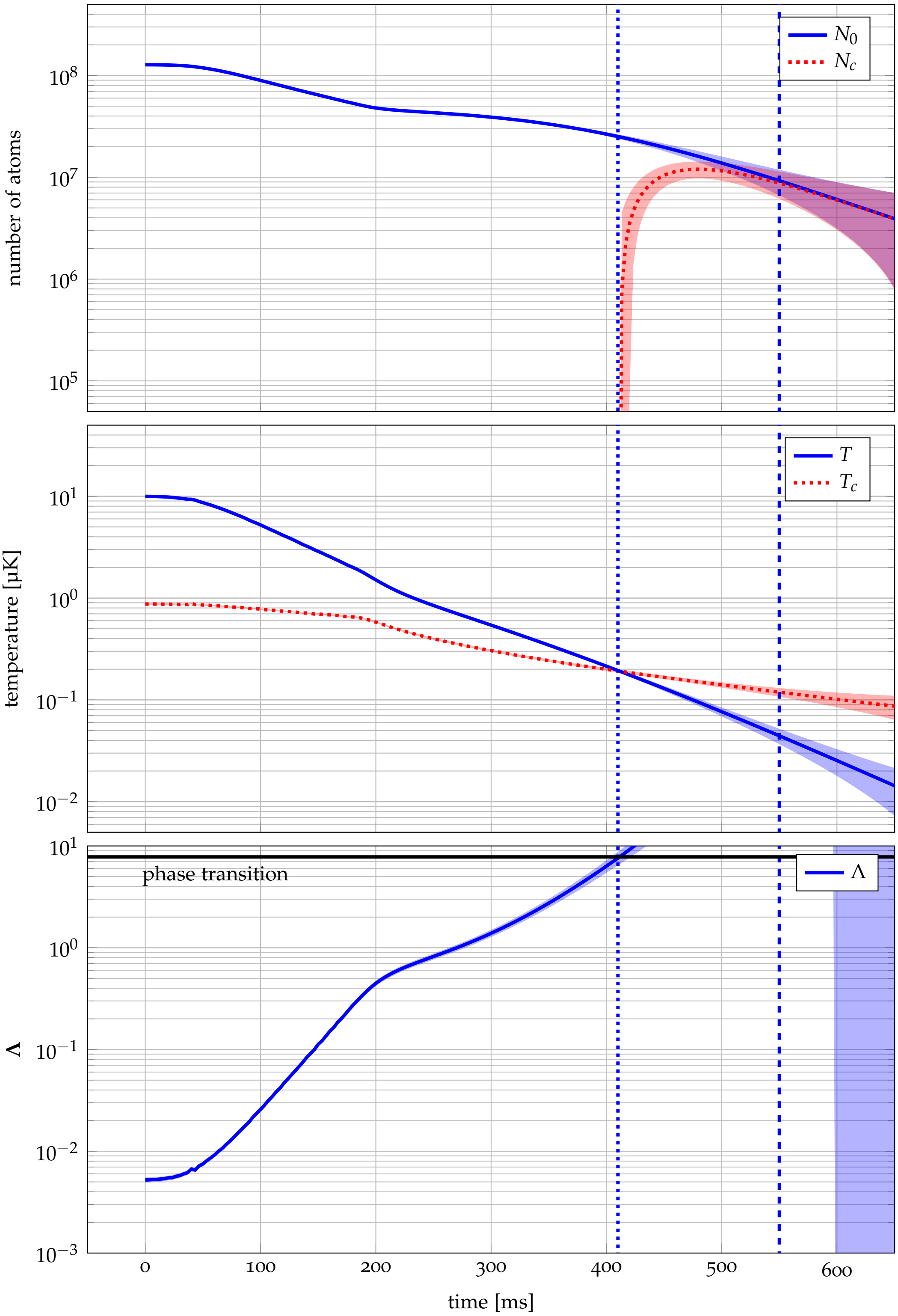

Figure 4.8: Simulation of the evaporation process in the new VLBAI setup. The simulation was performed for a trap with wavelength λ =1064 nm at 25 W, and an initial CPM amplitude of 200 µm in all spatial dimensions.

a modulation amplitude of 200 µm was chosen as the starting conditions for the simulation shown in **figure 4.8**. It is still possible to load above 10^8 atoms into the trap and to generate BECs with above 10^6 atoms below one second of evaporative cooling. The outcome of this simulation is marked as advanced scenario in **figure 4.9**.

BECs with a higher particle number can be generated by increasing the size of the trap and thus the loading efficiency, **equation (4.2)**. But higher spatial modulation amplitudes lead to lower trap frequencies. Hence the rethermalization time increases and the evaporation speed slows down. To a certain point this can be compensated by increasing the optical power. Another possible way is to choose a modulation amplitude for best loading efficiency. Subsequent to loading an adiabatic compression of the trap is performed [89]. This way one gains in PSD already before the actual evaporation process. This way one combines the high loading efficiency of the broad trap and the evaporation in a stiffer trap.

4.3 COMPARISON WITH OTHER BEC SOURCES

Neutral atoms are typically trapped in magnetic or optical potentials. Both allow for generation of BOSE-EINSTEIN condensates. A comparison of different BEC sources is given in **figure 4.9**. The first observations of BECs were achieved by performing evaporative cooling in magnetic traps [86–88]. The fields for those traps are classically generated by solenoids outside of the vacuum chamber. To achieve trapping confinements, capable of holding and evaporative cooling the atoms, large currents are needed [152]. For higher confinements the evaporation rate is faster. Therefore the generation of BECs can take a few tens of seconds [149, 150].

To speed up the flux of quantum degenerate gases and to reduce the power consumption the preparation of BOSE-EINSTEIN condensates is performed on so called atom-chips. These atom-chips, which are placed inside the vacuum chamber very close to the atoms, use micrometer wire structures to generate high magnetic gradients near the chip's surface. This leads to a lower power intake and enables the setup of transportable BEC sources [139, 146] that can be even operated in space[72, 75]. To date, chip based experiments are the sources with the highest BEC flux.

Compared to magnetic traps, optical dipole traps can capture all atomic species, with a dynamic polarizability, magnetically non-susceptible atomic species, e.g. ytterbium in VLBAI, and their sub-states. The latter allows to further cool the atoms by means of laser cooling inside the far-off-resonance trap. DOPPLER-cooling on a narrow transition of ^{84}Sr to quantum degeneracy was reported [126] in a crossed optical dipole trap with a tight confinement in the center. Also by RAMAN sideband cooling it is possible to reach the transition to BEC [128]. The confinement of atoms by an optical potential permits tuning the inter-atomic interaction strength via FESHBACH-resonances driven by magnetic field. By tuning the interaction strength of ^{39}K the RAMSAUER minimum can be compensated enabling direct evaporation [143].

While in magnetic traps the evaporative cooling is usually performed by coupling the trapped and untrapped atomic states with energy selective RF-photons, which

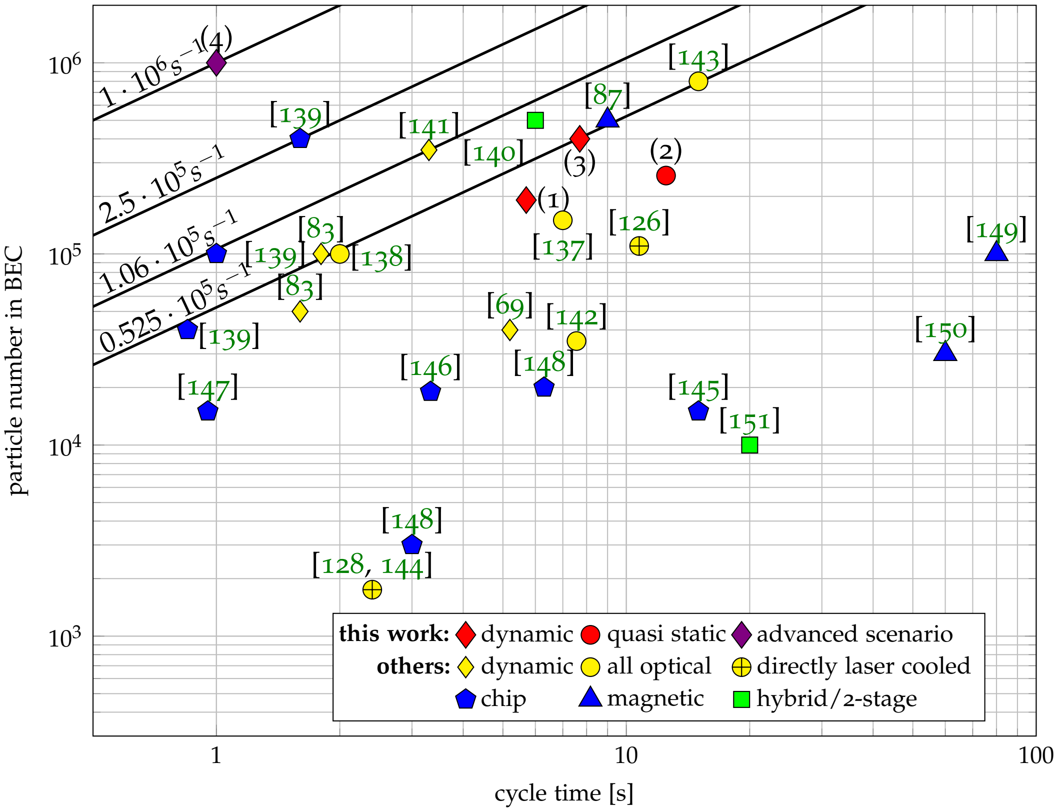

Figure 4.9: Comparison of different BEC sources. The red marker present the results of this thesis: (1) and (2) show the compared data discussed in 4.2.3, (3) presents the BEC with the highest achieved number of condensed atoms. (4) depicts the outcome of the numerical simulation for the advanced scenario 4.2.4. Yellow markers stand for all optical BEC generation. Diamond shaped points stand for dynamic traps, and circles for quasi static traps. Directly laser cooled BECs are depicted as yellow crossed circles. Blue markers stand for magnetic traps, pentagons for atom chip traps, and triangles for classical magnetic traps. Green squares represent hybrid approaches uniting optical and magnetic potentials.

maintains the trapping frequency over the entire evaporation process, evaporation in optical dipole traps is typically forced by lowering the optical power and thus reducing the trap confinement. This leads to a decrease in trap frequency and lowers the rethermalization rate. To overcome this limitation dynamic trap configurations can be used. By shifting the focus positions of the beams of a crossed optical dipole trap one can start with a rather large trapping volume and compensate for the loss in trap frequency during the lowering of the potential [141].

4.4 CONCLUSION

The results from section 4.2.3 show, that by reducing the center-position modulation-amplitude during the evaporation process the time needed for evaporative cooling can be shortened by a factor of about 3. Overall it was possible to improve the previous result [151] of generating BECs in the ODT setup by a factor of up to 40 in condensed atom number and up to four in repetition rate.

Even with comparable condensed atom number the repetition rate of the presented setup is still slower than the other comparable BEC sources. To improve the phase space density in the beginning of evaporation the population of only one magnetic sub-state, for subsequent interferometry the $m_F = 0$ state, is favorable. This can be achieved by optical pumping, an adiabatic-rapid-passage [153, 154] or a sequence of state preparation repetitions [155].
Besides the evaporation, loading the MOT is the most time-consuming time interval in the experimental sequence. In the new setup, presented in 4.2.4, this limitation is removed. An increased flux in the 2D-MOT loads up to 2×10^9 atoms within 200 ms. This is an improvement of about a factor of 20 to the experiment setup presented in this work. The simulation shows, that Bose-Einstein condensates with above 1×10^6 atoms can be produced with an repetition rate of about 1 Hz, thus outperforming today's best BEC sources.

5

MATTER-WAVE LENSING IN TIME-AVERAGED OPTICAL POTENTIALS

After evaporative cooling, the ensemble's temperature is on the order of a few tens of nanokelvin. This results in expansion rates of more than $1.5\,\mathrm{mm\,s^{-1}}$. To further reduce the expansion the dynamic character of the time-averaged potential is used to enable matter-wave lensing. Contrary to Delta-Kick collimation, where the atoms are released from the trap to allow for free expansion, which is stopped by a subsequent pulse of the trapping potential.
Under the influence of gravity such techniques are limited by the free expansion time, since the atomic cloud drops out of the trapping region. In the scheme presented in this chapter a different approach to collimate the expansion of the ensemble by means of matter-wave lensing is performed. The atoms are released

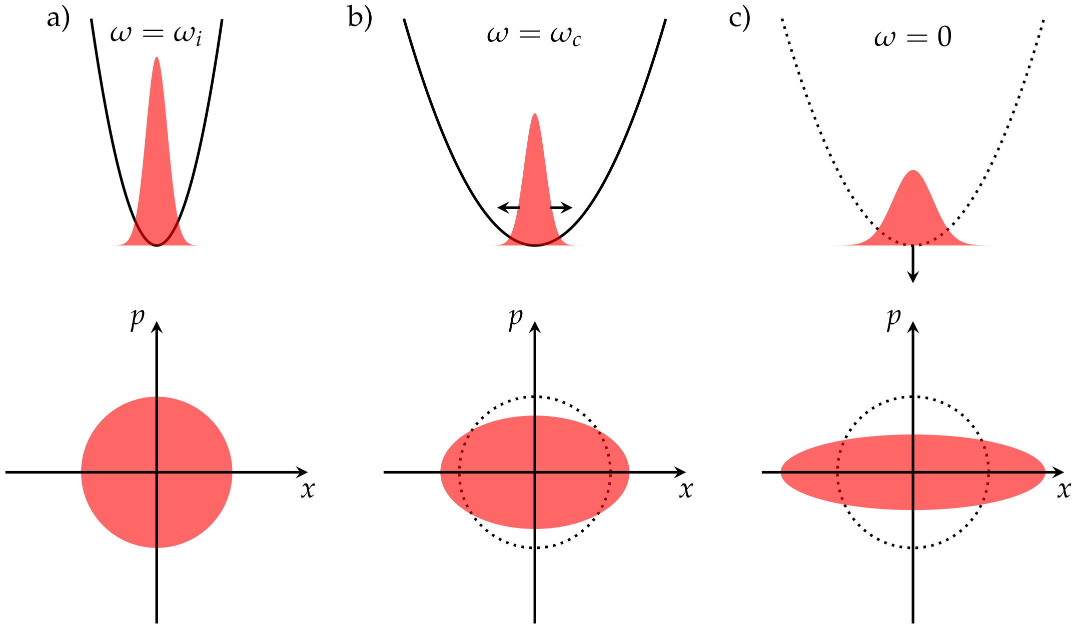

Figure 5.1: Cartoon of the matter-wave lens and the corresponding phase space diagrams for each step. The sequence starts in the initial trap ω_i (a)), the distribution in phase space is equally distributed. When the confinement is rapidly changed to the collimation trap ω_c (b)) the ensemble size starts to oscillate in the shallower trap. The momentum p is decreased while the atoms convert kinetic into potential energy rolling up the collimation potential. At the turning point of the size oscillation (c)) the trap is turned off $\omega = 0$. The momentum distribution is reduced to a minimum while the size of the atomic ensemble is the largest.

from the initial trap into a spatially extended trap, at this time the atoms size starts to oscillate in the collimation trap with frequency $2\omega_c$. After a certain time

$$t_{hold} = \left(n + \frac{1}{2}\right)\frac{\pi}{\omega_c} \quad , n \in \mathbb{N} \quad , \tag{5.1}$$

the size reaches a maximum. At this turning point the kinetic expansion energy is minimized and the potential is turned off and the atoms are released into free fall (**figure 5.2**). In this matter-wave lens configuration a collimation of the expansion of the wave-packet is archived. The reduction of the ensemble's expansion depends on the ratio of the squared trap frequencies of the initial trap (ω_0) and the collimation potential (ω_c) [94].

$$\frac{\sigma^2_{v,c}}{\sigma^2_{v,0}} = \frac{\omega^2_c}{\omega^2_0} = \frac{\sigma^2_{r,0}}{\sigma^2_{r,c}} \tag{5.2}$$

For low collimation trap frequencies the ensemble can expand to larger sizes and the reduction of expansion velocity is stronger, this is analogue to Delta-Kick collimation.

To describe the size evolution of the trapped and freely expanding ensemble the scaling approach is used.

5.1 SCALING APPROACH

The dynamics of an ideal gas can be described using the scaling approach. Here the formulas and a brief description are given, for more details see Ref. [156]. From Ref. [157] we get

$$\ddot{b_i} + \omega^2_{c,i} b_i - \omega^2_{0,i}\frac{\theta_i}{b_i} + \omega^2_{0,i}\xi\left(\frac{\theta_i}{b_i} - \frac{1}{b_i \prod_j b_j}\right) = 0 \tag{5.3}$$

$$\dot{\theta_i} + 2\frac{\dot{b_i}}{b_i}\theta_i + \frac{1}{\tau}\left(\theta_i - \frac{1}{3}\sum_j \theta_j\right) = 0 \quad , \tag{5.4}$$

where $b_i(t)$ is the dimensionless scaling factor describing the time evolution of the ensemble size and θ_i acts as an effective temperature in the directions $i \in x, y, z$. The angular trap frequency $\omega_{c,i}$ defines the collimation potential and $\omega_{0,i}$ the initial potential. This system of six coupled differential equations contains the mean field interaction, given by the factor [158]:

$$\xi = \frac{E_{mf}}{E_{mf} + k_B T} \quad , \tag{5.5}$$

with

$$E_{mf} = \frac{4\pi\hbar^2 a n_0}{m} \quad , \tag{5.6}$$

were a is the s-wave scattering length, n_0 the peak density (**equation (4.9)**) and m the mass of a single atom. Collision effects are also taken into account by

$$\tau = \tau_0 \times \left(\prod_j b_j\right) \times \left(\frac{1}{3}\sum_k \theta_k\right) \quad , \tag{5.7}$$

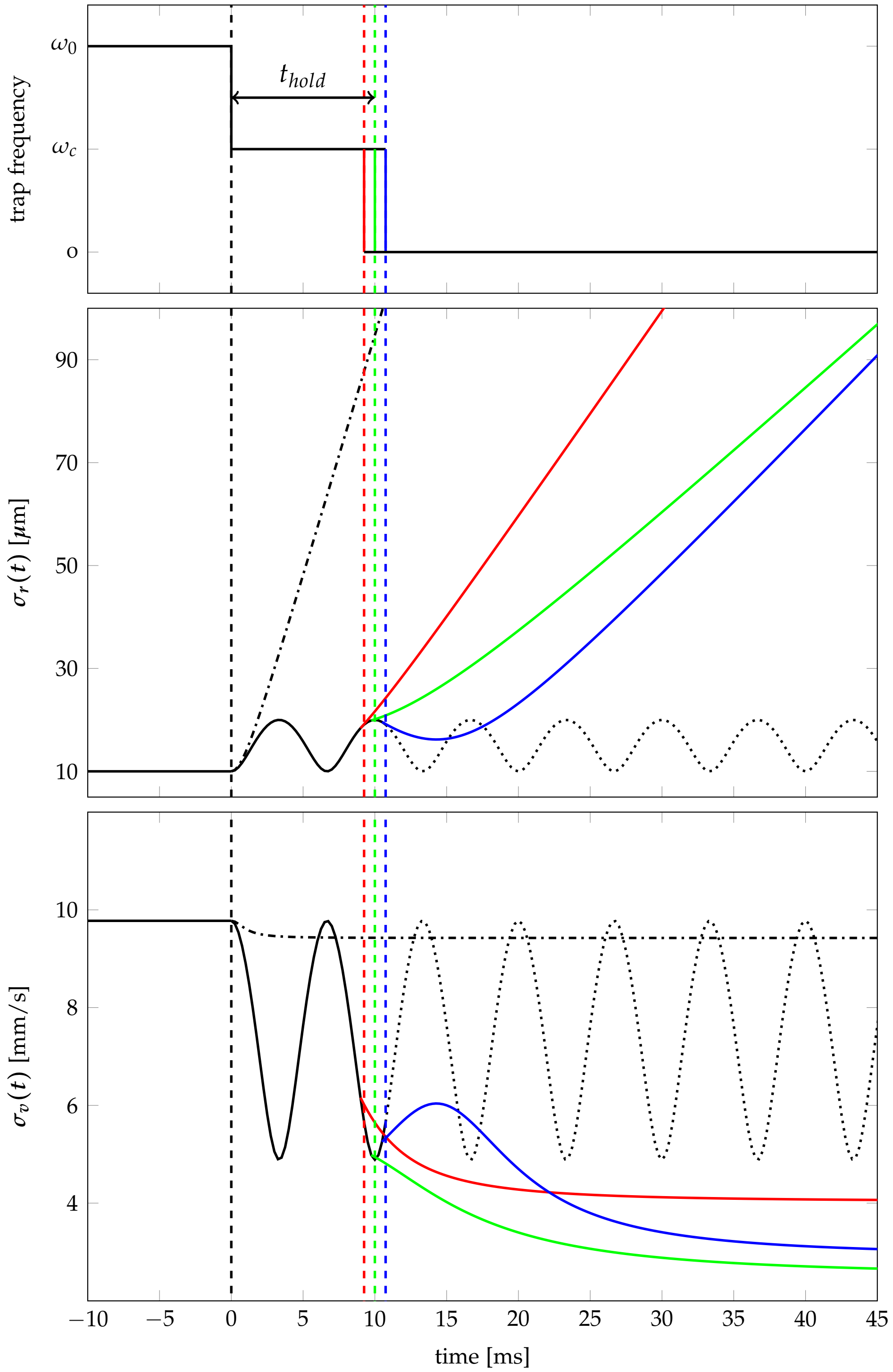

Figure 5.2: Time evolution of the size and expansion velocity during the Delta-Kick collimation sequence for a thermal ensemble with $T = 1\,\mu\text{K}$, $\sigma_0 = 10\,\mu\text{m}$, and $N = 1 \times 10^7$ in one dimension for three different holding times. The top graph shows the trap frequency behavior during the Delta-Kick collimation, ω_0 for the initial trap at the end of the evaporation process, and ω_c for the trap used for the collimation. In the middle the size evolution is depicted for four different scenarios. The black dashed dotted line corresponds to the free size evolution without Delta-Kick collimation, in green the atoms are released after an holding time (t_{hold}), optimal for lowest expansion rate. The red (blue) curves show the behavior for a too early (late) release. The bottom graph shows the expansion velocity evolution.

with the relaxation time

$$\tau_0 = \frac{5}{4\gamma} \tag{5.8}$$

and [157]

$$\gamma = \frac{2}{\sqrt{2\pi}} n_0 \sigma_{coll} \sqrt{\frac{k_B T}{m}} \quad . \tag{5.9}$$

For the special case of a BEC the mean field energy is large, compared to the ensembles thermal energy ($\xi \approx 1$) and the time scale on which collisions appear goes to zero ($\tau \approx 0$). **Equation (5.3)** will turn into the form known from Ref. [159]. With this set of equations one can simulate the time evolution of the ensemble's size (σ_{r_i}) and velocity distribution (σ_{v_i}) during the entire sequence of matter-wave lensing by [156]

$$\sigma_{r_i}(t) = \sigma_{r_i}(0) \times b_i(t) \quad , \tag{5.10}$$

and

$$\sigma_{v_i}(t) = \sqrt{\sigma_{v_i}^2(0) \times \theta_i(t) + \sigma_{r_i}^2(0) \times \dot{b}_i^2(t)} \quad . \tag{5.11}$$

For a long enough freely evolving ensemble the expansion rate is given by the velocity distribution which can be transformed into an effective temperature using **equation (3.14)**.

For the case of a thermal ensemble the time evolution of the size and velocity spread in 1D is depicted in **figure** 5.2 for three different holding times(t_{hold}). One can see the importance of a well timed release.

5.2 EXPERIMENTAL SEQUENCE AND RESULTS

Subsequent to loading of the dipole trap and evaporative cooling the matter-wave lens is performed. Before rapidly changing the trap frequency ($\omega_0 \rightarrow \omega_c$) the atoms are kept in the initial trap, given by the final evaporation trap, for 50 ms. The switching from the initial trap to the collimation trap is performed using the AOM control (**figure** 3.7). For the matter-wave lens the spatial modulation of the trapping beams is increased to the maximum achievable amplitude. Since the modulation only takes place in the horizontal plane the collimation trap parameters are chosen that the vertical confinement is kept constant in order to suppress uncontrolled oscillations and atom loss. This is realized by increasing the optical intensity via the AOMs RF-power.

In order to find the right holding time (t_{hold}), measurements of the ensemble's radius with iterating t_{hold} and different time of flight (1.5 ms, 2.5 ms, 4.5 ms, 10 ms, 15 ms, 20 ms, 25 ms, 30 ms) were performed, see **figure** 5.3. From these 8 data sets the expansion velocity for each holding time is extracted using the method from 3.3. The optimal holding time was chosen to be the time with the minimal radial expansion velocity. This measurement was performed at different points within the evaporative cooling process, named "Set 1" to "Set 7". Only for "Set 7" the evaporative cooling was completed and the matter-wave lens was performed on a BEC. Since the radii of the BECs of "Set 7" scale with atom number by a factor of $N^{1/5}$, the evaluated radii were re-scaled to the mean atom number of the data set. The measurements of the oscillating velocity distribution are shown in the **figures** 5.4.

The results of the measurements as well as the trapping parameters are summed up in **table** 5.1.
The expected oscillations of the expansion rate, emanating from the numerical simulations of **equation** (5.3) and (5.4), are also shown in the graphs of 5.4. The simulation depends in sum on twelve parameters which are provided with an one-sigma error, see A.4. Due to computational reasons the simulation is not capable to propagate these error estimations. Therefore different combinations of randomly chosen normal distributed input parameters were fed into the model. For each set the simulation was performed in a loop for 1000 times and the mean value and standard deviation of the resulting curves was calculated for each point in time. The damping in the oscillation can be explained by the anisotropicity of the trap and the coupling between the differently directed motions. The simulation does not take into account the effects of gravity on the trapped atomic ensemble as well as anharmonicities in the trapping potential, which lead to the divergence of the measurements and simulations.
A reduction of the expansion rate is observed over all temperature regimes without significant atom number loss. **Figure** 5.5 shows the atom number of the initial and

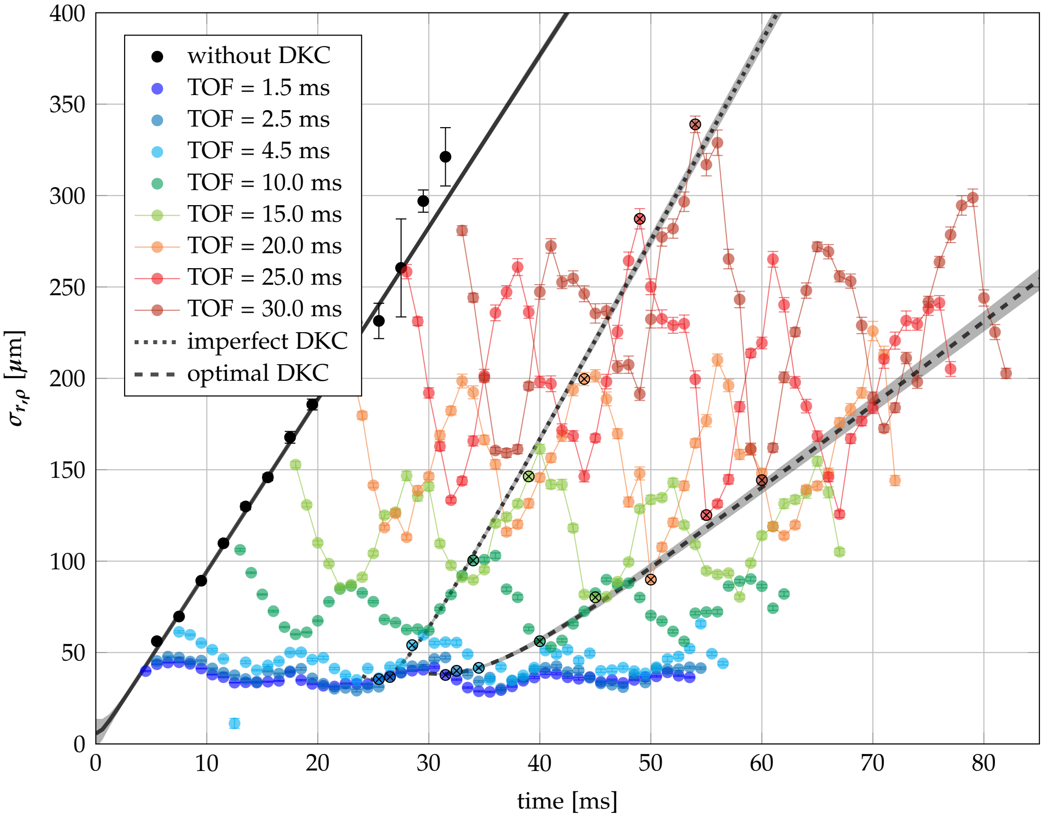

Figure 5.3: Measurement of the radial ensemble size oscillation for different TOF, see legend for color code, over time for different holding times $t_{hold} = t - TOF$. The black data points show the ensemble expansion without matter-wave lensing, with an initial temperature of T_ρ =930(10)nK. The curves represent exemplary expansion simulations for imperfect (dotted, t_{hold} =24 ms, T_ρ =1195(100)nK) and optimal (dashed, t_{hold} =30 ms, T_ρ =194(18)nK) holding time fitted to the highlighted data points.

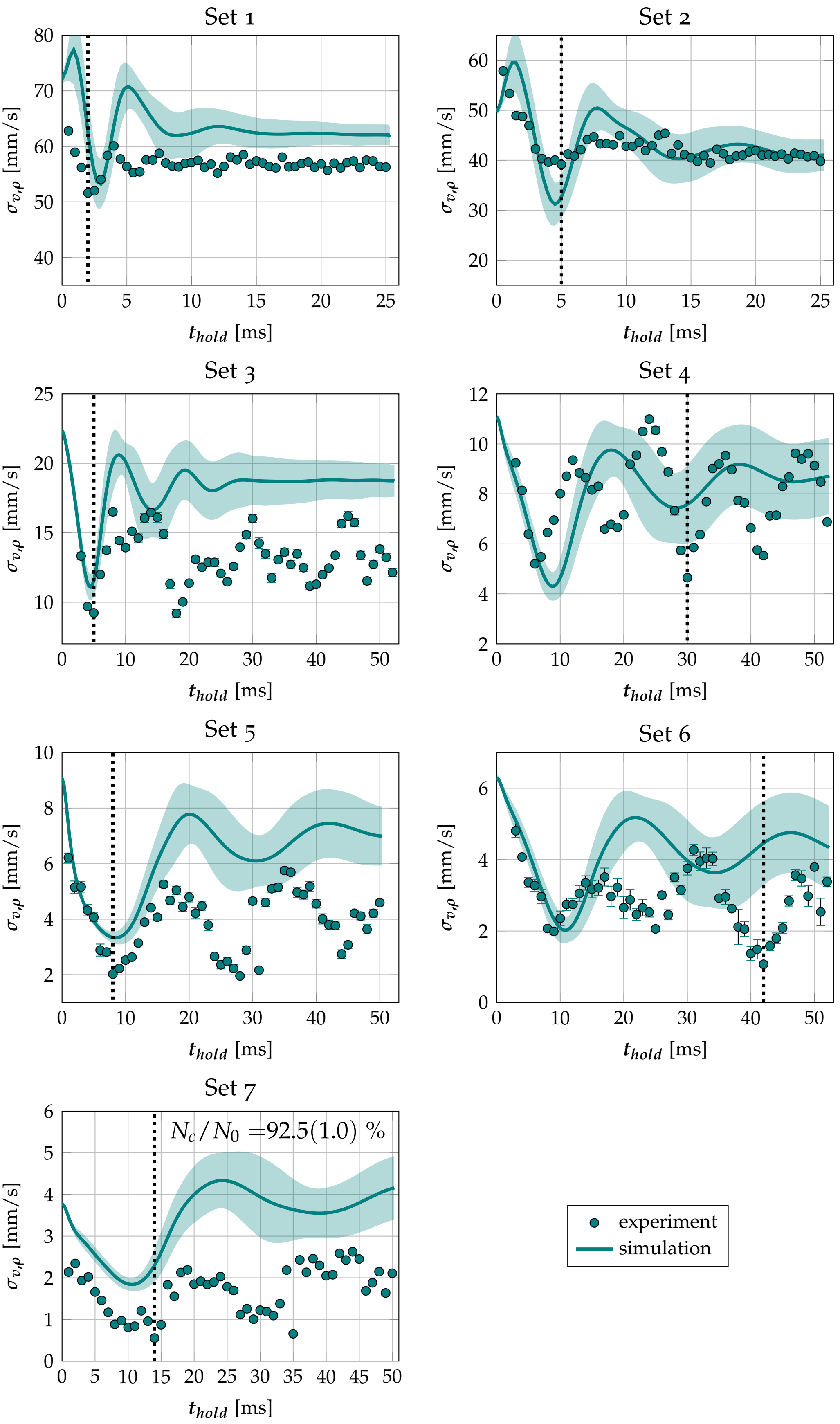

Figure 5.4: Oscillations of the expansion rate over holding time for different initial kinetic temperatures. "Set 1" to "Set 6" present data for thermal ensembles, $N_c/N_0 = 0$. "Set 7" shows the expansion rate oscillation for a BEC with 92.5 % condensed atomic fraction. The experiment parameters for all sets are summed in **table 5.1**. Vertical dotted lines display the optimal holding time due to the measured data. The shaded areas give an error estimation of the radial expansion rate.

final expansion velocity after the matter-wave lens. The lowest expansion rate is achieved with 553(49) $\mu\mathrm{m\,s^{-1}}$ with a related effective temperature of 3.2(0.6) nK at an atom number of $4.24(0.02) \times 10^5$. This is a more than one magnitude lower temperature than achieved by evaporative cooling, with a comparable atom number.

5.3 CONCLUSION

The collimation of the expansion rate by means of matter-wave lensing is applicable to atomic ensembles captured by time-averaged potential in all initial temperature regimes. A reduction of the kinetic temperature of the clouds by a factor of up to 30 within tens of milliseconds is achieved. Still the results presented in this chapter do not present the theoretically achievable values.

Anharmonicities of the trapping potential are likely to appear due to the narrow AOM frequency bandwidth, see **figure** 5.6 and appendix A.3, which leads to amplitude modulations over the center-position modulation transit. This leads to spatial dephasing of the atomic ensemble's motion. To fully understand the dynamics of the atoms a second imaging system, observing along a vertical path, would be required.

Matter-wave lensing relies on the elimination of the trapping potential precisely at the turning point of the size oscillation, **figure** 5.2. The angle of intersection of the here presented crossed optical dipole trap beams is 70°. Even for perfectly power

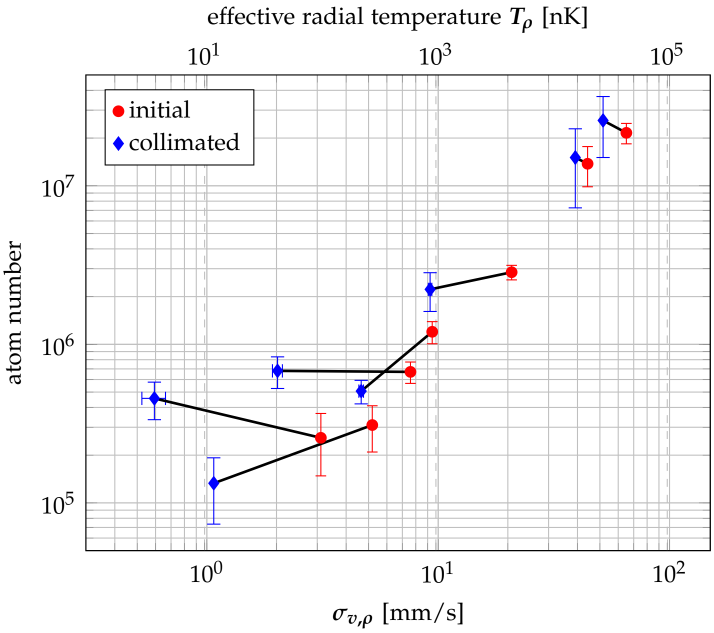

Figure 5.5: Atom numbers of the ensemble before (red circles) and after (blue diamonds) matter-wave lensing. The black lines connect the affiliated points from the same data set. The corresponding effective temperature is displayed on the top x-scale. No significant change in atom number was observed by the matter-wave lens. Since the modulation only acts in the horizontal plane only the radial expansion rate is displayed in this graph, the results in vertical direction are shown in **table** 5.1.

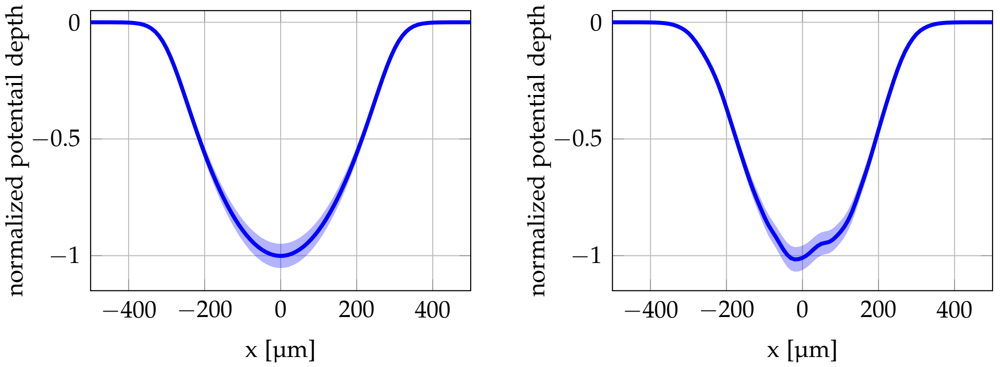

(a) Normalized potential shape without frequency dependent diffraction efficiency of the AOM.

(b) Normalized potential shape with frequency dependent diffraction efficiency of the AOM.

Figure 5.6: Normalized trapping potentials (a) without the frequency dependent diffraction efficiency of the AOM, and (b) with imperfections in the diffraction efficiency of the AOM.

balanced and equally focused beams this leads to different trapping frequencies in x- and y-direction and thus dephasing of the size oscillations. Efficient matter-wave lensing can only be applied if the optimal holding time (**equation (5.1)**) matches for all axes. This restriction can be overcome either by an angle of intersection of 90° for beams with equal properties or by using two independently modulated crossed beams. The latter would also increase the need for optical power by a factor of two. Besides this, the narrow bandwidth of the AOM leads to an anharmonic potential. This can be compensated by precisely adjusting the optical power during the modulation transit. Another approach can be the utilization of acousto optical deflectors (AODs). Here the broader frequency range will reduce the amplitude modulation.

The performance of the collimation process in three dimensions is mainly limited by the spatial dimensions of the time-averaged optical potential. The currently not implemented modulation of the optical dipole trap beam in the vertical direction limits the potential width to approximately 45 µm. To hold the atoms against gravity the trap frequency in this direction should not drop below $\omega_z/2\pi \approx 140\,\mathrm{Hz}$. For a Gaussian shaped vertical potential the estimated trap depth can be found in **figure 5.7**. The larger the effective potential width, the lower the possible trap frequency capable of counteracting gravity. For a time-averaged potential with parabolic shape the vertical trapping frequency can be lowered further than in the gaussian case. Since the expansion rate reduction due to the matter-wave lens scales with the ratio of the trap frequencies, modulating the vertical axes will improve the performance of the collimation. Ultimately it allows for cancellation of gravity by a linear vertical potential gradient [160]. Under this conditions even lower trap frequencies are feasible as well as a Delta-Kick collimation scheme which will be only limited by the extension of the gravity compensating potential. The modulation of the vertical beam position can be achieved using an orthogonal acousto-optical modulator subsequently to the existing one. Implementing a second AOM will lead to an additional intensity loss while the modulation in the extra additional would require a higher

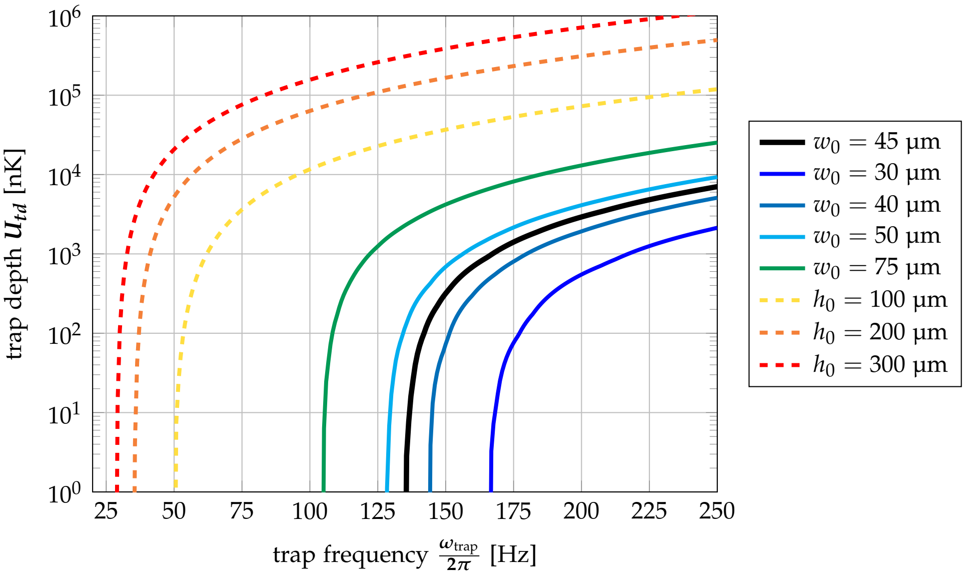

Figure 5.7: Dependency of the trap depth on the trapping frequency and the potential size. The solid lines show the behavior of unmodulated GAUSSIAN potentials formed by a beam with waist w_o, and the dashed lines for a time-averaged potential of parabolic shape with radius h_0. The black line displays the behavior for a potential formed by a GAUSSIAN beam with vertical waist of $w_0 = 45$ µm, which is close to the vertical beam waist estimated in 3.5.1.

intensity. Therefore also this setup would be mainly limited by the available optical power.

Set:		$\omega_x/2\pi$	$\omega_y/2\pi$	$\omega_z/2\pi$	$\sigma_{v,\rho}$	$\sigma_{v,z}$	T_ρ	T_z	N
	Unit:	Hz			$\mathrm{mm\,s^{-1}}$		nK		
1	initial	142.8(15.5)	203.9(19.7)	777.9(35.5)	65.08(0.5)	46.29(0.08)	44312.8(680.74)	22421.57(81.33)	2.28(0.00) $\times 10^7$
	lensed	83.9(9.7)	119.6(13.1)	656.9(30.0)	**51.61(0.18)**	40.73(0.01)	**27873.08(197.54)**	17355.42(6.42)	**2.20(0.00) $\times 10^7$**
2	initial	131.8(13.4)	187.6(16.0)	557.3(25.5)	44.24(0.51)	33.35(0.11)	20476.16(467.87)	11636.47(80.19)	1.27(0.00) $\times 10^7$
	lensed	53.7(6.2)	76.6(8.4)	420.4(19.2)	**39.15(0.22)**	28.06(0.06)	**16041.11(177.09)**	8237.84(36.84)	**9.72(0.01) $\times 10^6$**
3	initial	164.9(15.9)	218.1(10.5)	268.9(12.4)	20.77(0.15)	12.64(0.05)	4514.6(66.62)	1670.83(12.33)	2.70(0.01) $\times 10^6$
	lensed	52.3(5.7)	74.6(7.1)	268.3(12.3)	**9.23(0.16)**	12.88(0.18)	**890.75(31.0)**	1735.72(47.51)	**2.57(0.00) $\times 10^6$**
4	initial	138.0(14.9)	181.4(8.8)	209.9(9.8)	9.42(0.06)	8.59(0.04)	928.81(12.68)	771.36(7.09)	7.70(0.02) $\times 10^5$
	lensed	26.5(3.3)	37.8(4.2)	207.7(9.6)	**4.65(0.11)**	8.35(0.06)	**225.91(10.48)**	728.72(11.23)	**7.40(0.02) $\times 10^5$**
5	initial	124.1(13.6)	162.7(8.0)	187.9(8.8)	7.59(0.14)	7.29(0.11)	602.68(21.7)	555.66(16.36)	9.80(0.01) $\times 10^5$
	lensed	24.0(3.1)	34.2(3.8)	187.9(8.7)	**2.02(0.1)**	6.27(0.11)	**42.75(4.22)**	410.8(14.51)	**9.73(0.01) $\times 10^5$**
6	initial	111.7(12.5)	146.4(7.3)	168.9(8.0)	5.19(0.09)	5.2(0.08)	281.65(9.35)	282.72(8.28)	8.70(0.10) $\times 10^4$
	lensed	21.5(2.9)	30.6(3.4)	168.0(7.8)	**1.07(0.0)**	4.16(0.21)	**12.0(0.01)**	181.19(18.01)	**1.52(0.01) $\times 10^5$**
7	initial	105.2(11.8)	137.9(6.9)	159.1(7.5)	3.11(0.01)	3.13(0.01)	101.22(0.76)	102.82(0.97)	4.32(0.01) $\times 10^5$
	lensed	20.3(2.8)	28.9(3.2)	158.8(7.4)	**0.55(0.05)**	2.17(0.06)	**3.2(0.56)**	49.25(2.78)	**4.24(0.02) $\times 10^5$**

Table 5.1: Results of the Delta-Kick collimation.

6

CONCLUSION

Dynamic time-averaged optical potentials can accelerate the process of evaporative cooling and allow for the creation of Bose-Einstein condensates with more than 10^5 atoms. Together with a further reduction of the expansion rate by means of matter-wave lensing this will improve the performance of the dual-species atom interferometer and lowers the susceptibility of it to systematic errors such as wavefront aberration.

In the scope of this thesis, the existing optical dipole trap setup [115, 120, 151] was upgraded to a crossed ODT. Center position modulation of the dipole trap beams enables the generation of time-averaged potentials to dynamically control the trapping parameters in the horizontal directions.

Those time-averaged potentials improved the number of atoms loaded into the trap from the optical molasses by a factor of 2 by increasing the effective waists of the crossed optical dipole trap beams. With these starting conditions and the dynamic control of the trap size it is possible to efficiently cool the trapped ensembles by means of evaporative cooling. This way the production of BECs with up to $4.2(0.1) \times 10^5$ atoms within 5 s of evaporation was achieved, which corresponds to a flux of about 5×10^4 atoms/s. In only 3 s still $1.9(0.4) \times 10^5$ atoms were achieved. The ensembles have a kinetic temperature of $T = 29.2(1.3)$ nK. Numerical simulations show the possibility to generate BECs containing above 10^6 atoms with a 1 Hz repetition rate, in an advanced scenario with faster trap loading ($>10^8$ atoms in about 200 ms) and center-position modulation in horizontal and vertical direction. Furthermore the dynamic properties enable the use of the time-averaged potential trap for optical matter-wave lensing. The expansion rate of the ensemble is reduced in two dimensions as low as $553(49)\ \mu\mathrm{m\,s^{-1}}$ resulting in an effective temperature of $3.2(0.6)$ nK, while the expansion in the vertical dimension stayed nearly the same.

6.1 CURRENT LIMITATIONS AND WAYS TO IMPROVE

The final results, summarized in the former section, result from the optimization methods described in this thesis. Limitations due to technical reasons as well as ways to improve the performance will be discussed in this section.

6.1.1 *Technical Limitations*

The current setup underlies some technical limitations arising from the dimensions, the size and shape, as well as the optical parameters of the trap and will be discussed in the following.

6.1.1.1 *Shape of the Trap*

ISOTROPICITY

The center-position modulation is only applied in the horizontal plane. This leads to a highly anisotropic disc shaped trapping potential. By modulating the dipole beams also in the orthogonal direction isotropic traps can be created. This will increase the effective trap volume and improve the mode match for the transfer into the trap. Especially the matter-wave lensing will benefit from an isotropic harmonic potential. In a three dimensional isotropic potential, the cloud sizes oscillate in phase at the same frequency in all directions. This will simplify the optimization of the optimal holding time due to the reduction of beating originating from the coupling of the oscillation axes and clears the routes toward picokelvin temperatures, see section 6.1.2.2.

SIZE AND DEFORMATION

The size of the time-averaged potential depends on the spatial modulation amplitude of the dipole beams. The AOM used in the here presented setup provides a rather small center-position modulation amplitude of about 200 µm. Up to $h_0 \approx 430\,\mu\mathrm{m}$ would be feasible with a different lens system and the AOM closer to the vacuum chamber[1], see **figure 2.2**. The waist of the beam at the position of the atoms would be $w_0 \approx 80\,\mu\mathrm{m}$ and limited by the aperture of the AOM. This would allow for larger traps and improve the loading efficiency.

The expansion rates after optical matter-wave lensing depend on the ratios of trap frequencies of the initial and final traps. By increasing the modulation amplitude, and thus decreasing the trapping frequencies, the matter-wave lensing performance will improve due to the larger amplitude of size oscillations. The spatial modulation amplitude of the current setup is highly limited by the narrow frequency response of the AOM. This also leads to amplitude variations over the course of the modulation transit and deforms the time-averaged potential, see section 5.3. To achieve larger frequency bandwidths AODs are more suitable. Here center-position modulation amplitudes of $h_0 \approx 3.3\,\mathrm{mm}$ are feasible in a similar setup. Another advantage of AODs is that they provide nearly constant diffraction efficiency over a broad frequency range and thus reduce deformation of the potentials. At the time of writing, no AODs for a wavelength of 1960 nm were available. However, suitable deflectors are standard elements for lasers at a wavelength of 1064 nm, which are appropriate for optical dipole traps and will be used in the setup described in section 4.2.4.

6.1.1.2 *Optical Power*

The optical power determines the depth of the trapping potential. In the experiment, optical power is reduced by several components: The Pockels-cell, employed for stabilization and control of the optical power, and the assoiated optics cause a loss of about 40 %, due to imperfect coatings of the optical components. Another 40 %

---

[1] This value is based on a of 150 mm and $\delta\Theta/\delta f = 0.36\,\mathrm{mrad\,MHz^{-1}}$ with a modulation amplitude of 8 MHz.

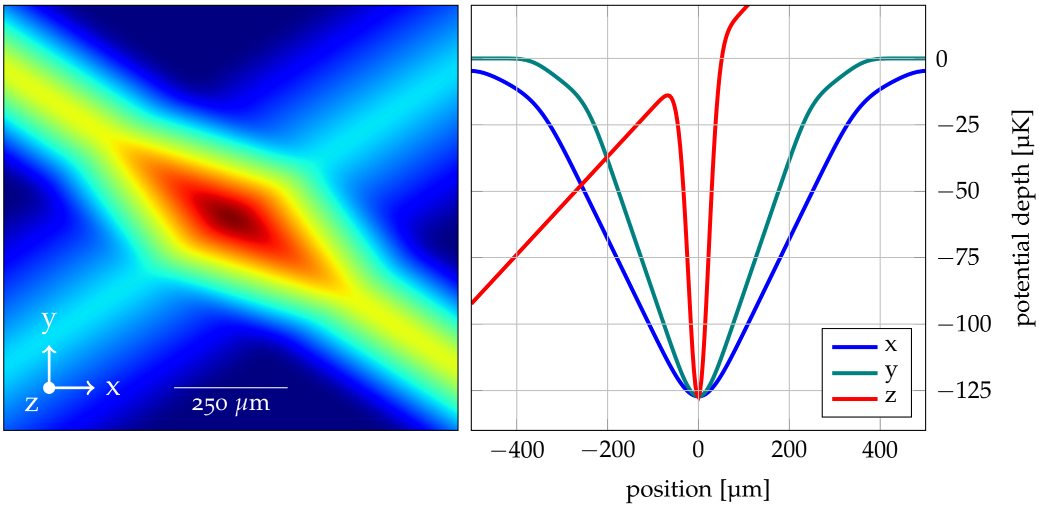

Figure 6.1: Left side: 2D simulation of a linear potential created by center-position modulation of the optical dipole trap beams. Right side: potential shapes cutting through the center. The corresponding axes are depicted by the coorinate system in the left image.

is lost due to the diffraction efficiency of the AOM. In order to reduce heating, due to interference, the polarizations of the light beams are cleaned up before passing through the vacuum chamber. This reduces the power by another 30 % leading to a final optical power at the atoms of only 12.5 W (25 % of the laser's output power).

By performing intensity control and stabilization with the AOM instead of the Pockels-cell, and using high quality polarization optics (estimated loss of 15 %) it will be possible to use up to 45 % of the laser power to manipulate the atoms. This will increase the loading efficiency and simplifies the system.
In order to keep the vertical trap parameters constant when releasing the atoms into the collimation trap, the optical power needs to be increased. In the current setup this is done via the VCA for the RF-power of the AOM. If the AOM is the actuator for the intensity control, the optical power could be adjusted over the full range. This will be crucial when utilizing 2D-AODs for large isotropic traps.

6.1.2 *Ways to Improve*

Besides the reduction of technical limitations an improvement of the experiment is possible by adapting the parameters of the time-averaged potential to the needs of the experimental phase. In the potential used in this work is parabolic shaped, but loading the atoms into a box-shaped potential can be beneficial due to a constant AC-Stark shift. Thus the laser cooling is undisturbed over a larger volume. Also linear potentials, see section 6.1.2.1, or potentials with a linear gradient, section 5.3, can improve the generation of low-expanding quantum gases.

6.1.2.1 *Evaporative Cooling in Linear Potentials*

This work shows that the production of BECs in optical traps can be sped up using dynamically shaped harmonic traps. A further improvement is possible by using a

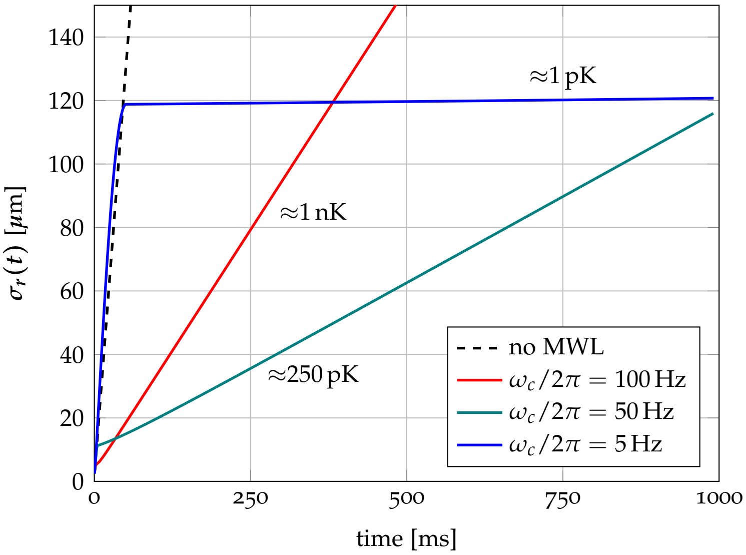

Figure 6.2: Expansion of the ensemble for different collimation trap frequencies (ω_c) with optimal holding times. The simulation was performed for an isotropic harmonic trap with initial trapping frequency of $\omega_i/2\pi = 200\,\text{Hz}$ and an ensemble of ^{87}Rb atoms with temperature $T = 100\,\text{nK}$.

different trap geometry.

The energy taken away by one evaporated atom (ϵ_{out}) scales with the parameter ξ as [125]:

$$\epsilon_{out} \propto \xi + \frac{3}{2} \quad . \tag{6.1}$$

The parameter ξ is defined by the geometry of the trapping potential and is $\xi = 0$ for a box potential with infinitely high walls, $\xi = 3/2$ for an isotropic harmonic potential, and $\xi = 3$ for an isotropic three dimensional linear potential. Also the reduction of effective trap volume, which scales as $V \propto T^{\xi}$, by lowering the temperature is faster for bigger ξ. As a result the density grows faster and the elastic collision rate increases. This speeds up the rethermalization and accelerates the evaporative cooling process. In **figure 6.1** a linear potential in two dimensions is depicted, as it can be realized by the current setup. Analogue to **equation (2.16)** the shape of the potential is determined by the function:

$$g(f') = 1 - (abs(f')/h_0) \quad . \tag{6.2}$$

Dynamic time-averaged potentials offer the possibility to further investigate different trap configurations under comparable conditions.

6.1.2.2 *Matter-Wave Lensing by Low Frequency Traps*

The optical matter-wave lens in a dynamic time-averaged potential is a straightforward technique to efficiently reduce the expansion rate of atomic ensembles, and is applicable in all temperature ranges reachable by laser and evaporative cooling. Matter-wave lensing can be used to short-cut the preparation sequence for slow expanding quantum gases. This improves the performance of atom interferometers,

by increasing the repetition rate, and is not limited to optical dipole traps but can be also used in magnetic traps capable of fast potential changes.
The expansion after the lens highly depends on the trapping frequency (ω_c) of the collimation trap, and is depicted in **figure** 6.2 for the case of an isotropic trap and different ω_c. Holding against gravity requires a minimum vertical trap frequency, see **figure** 5.7. And hence, to lower the frequency further, gravity has to be compensated by employing a linear potential gradient. This can be implemented via optical painting [160]. Another way is the operation in μg-environments. By reducing the collimation trap frequency to values as low as $\omega_c/2\pi = 5\,\mathrm{Hz}$ expansion temperatures on the order of picokelvin are within reach.
Without compensating gravity, frequencies $\omega_c/2\pi = 50\,\mathrm{Hz}$ to $150\,\mathrm{Hz}$ are feasible and still expansion temperatures on the order of a few hundred pK are reasonable.

6.2 OUTLOOK

Wave front aberration is the dominant contribution in the current test of the Universality of Free Fall, performed with the dual-species atom interferometer presented in this work [50]. This systematic effect arises through an imperfect and varying overlap of the spatial distribution of the atomic clouds and the beam splitting light fields. Also disturbances of the wave fronts by the optical components play a role. This results in an uncertainty on the Eötvös ratio of $\delta\eta = 3 \times 10^{-7}$. The error can be reduced by superimposing the expansion of the two atomic ensembles by means of matter-wave lensing.
For the two species ^{39}K and ^{87}Rb the relation of the trap frequencies is given by:

$$\frac{m_\mathrm{K}}{\alpha_\mathrm{K}}\bar{\omega}_\mathrm{K}^2 = \frac{m_\mathrm{Rb}}{\alpha_\mathrm{Rb}}\bar{\omega}_\mathrm{Rb}^2 \quad , \tag{6.3}$$

were the α's are the real parts of the complex polarizabilities of the $^2S_{1/2}$ ground state[2]. By switching the collimation potential off at a common turning point the expansion of both species can be collimated. This does not necessarily imply that the size and expansion of the ensembles are overlapped to a sufficient degree. To do so one can still find a trade-off where the sizes of the clouds are nearly the same over long time of flights. In this case the temperatures do not reach their possible minima[3]. In the simulation this holding time could be found at $t_{hold} = 10.075\,\mathrm{ms}$ reaching effective temperatures of $T_\mathrm{Rb} = 61.6\,\mathrm{nK}$ and $T_\mathrm{K} = 28.3\,\mathrm{nK}$ with a cloud size of $\sigma_\mathrm{Rb} = 2411\,\mu\mathrm{m}$ and $\sigma_\mathrm{K} = 2478\,\mu\mathrm{m}$ after 1 s time of flight. The outcome of this simulation is depicted in **figure** 6.3.

By performing a dual species matter-wave lens the uncertainty on the Eötvös ratio due to wave front aberrations will be lowered, and thus resolving the main source of uncertainty in the current systematic analysis of performing tests of the Universality of Free Fall with potassium and rubidium [50]. Additionally, the release of the different ensembles from a common trap leads to an improved overlap of

---

[2] For ^{87}Rb this is $\Re(\alpha(5^2S_{1/2})) = 6.2 \times 10^{-39}\,\mathrm{C\,m^2\,V^{-1}}$ and for ^{39}K $\Re(\alpha(4^2S_{1/2})) = 5.5 \times 10^{-39}\,\mathrm{C\,m^2\,V^{-1}}$

[3] This statement is based on simulating the matter-wave collimation for one dimension with the following starting parameter: $T_\mathrm{K} = 10\,\mu\mathrm{K}$, $T_\mathrm{Rb} = 1\,\mu\mathrm{K}$, $\bar{\omega}_{\mathrm{Rb},0} = 300 \cdot 2 \cdot \pi$ Hz and $\bar{\omega}_{\mathrm{Rb},c} = 52.5 \cdot 2 \cdot \pi$ Hz. The initial cloud sizes are defined by the temperature and the trapping frequencies.

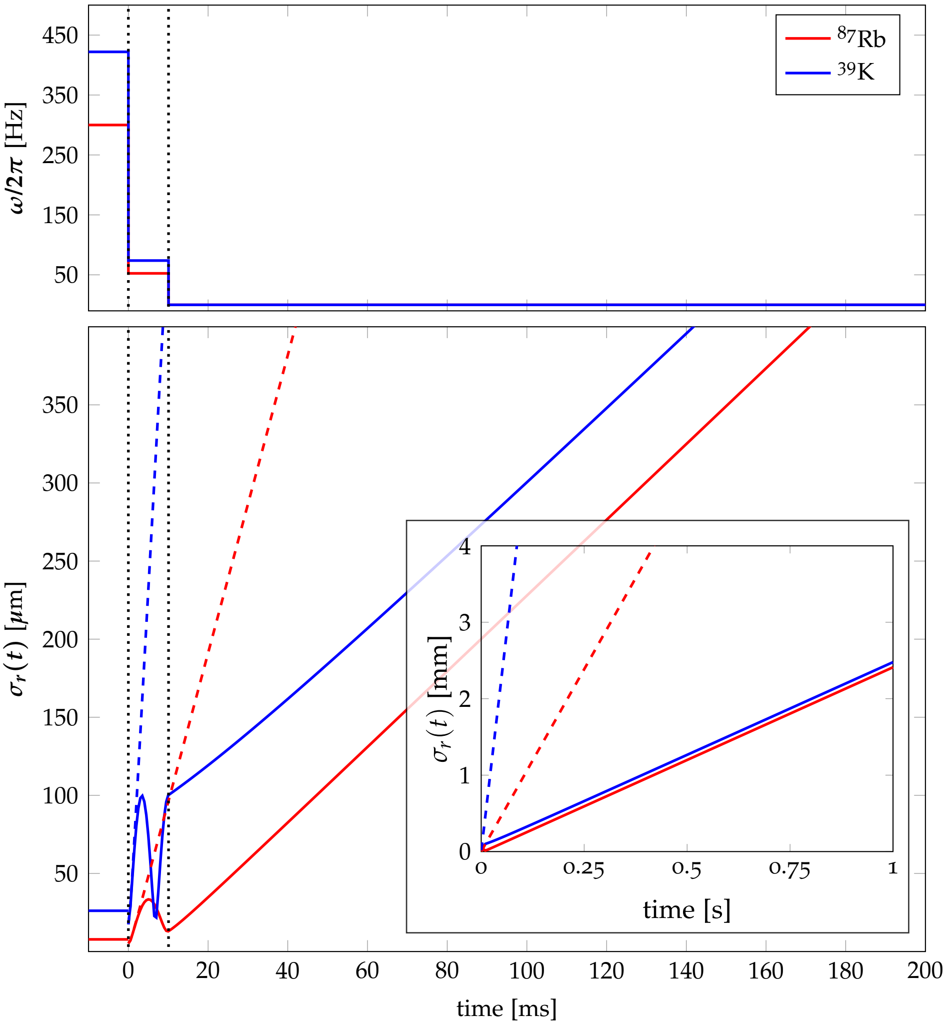

Figure 6.3: Time evolution of the size and expansion velocity during the matter-wave lensing sequence for two thermal ensembles with $T_{\mathrm{Rb}} = 1\,\mu\mathrm{K}$ and $T_{\mathrm{K}} = 10\,\mu\mathrm{K}$ in one dimension. The trap parameters are chosen to adjust the free expansion of ^{87}Rb (red curve) and ^{39}K (blue curve). The black dotted lines set the time at which the potential changes. The top graph shows the trap frequency behavior during the matter-wave lens. The bottom graph shows the size evolution. The behavior without matter-wave lensing is depicted as dashed lines. Insets show the behavior for longer time scales up to 1 s.

the center-of-mass motion. Systematic effects, stemming from gradients, are thus suppressed by the enhanced overlay of the trajectories of the atomic test masses. With the high flexibility and possibility to adapt the in this work presented schemes to various multi species experiments, applications at a range of precision measurements are possible. The presented techniques paves the path for UFF tests with unprecedented accuracy in ground based experiments, for example in the VLBAI facility. But also experiments in μg, like the PRIMUS experiment in Bremen [68, 161], will benefit from superimposed ensembles with low expansion rates.

A

APPENDIX

A.1 PARASITIC OPTICAL PUMPING INTO F=2

The laser used has a line width of about 80 GHz (1 nm spectral width). Based on the results presented in [162] the stimulated pumping between the two hyperfine ground states has been observed. In this publication a similar laser `[IPG, YLR-50-1070-LR]` with a spectral width (FWHM) of 2 nm at a wavelength of 1070 nm has been used. Since the laser used in this thesis has a larger detuning as well as a smaller line width a reduced scattering rate is expected. Figure A.1 shows the population evolution of the two states F=1 and F=2 and the fitted solutions of the rate equations A.1.

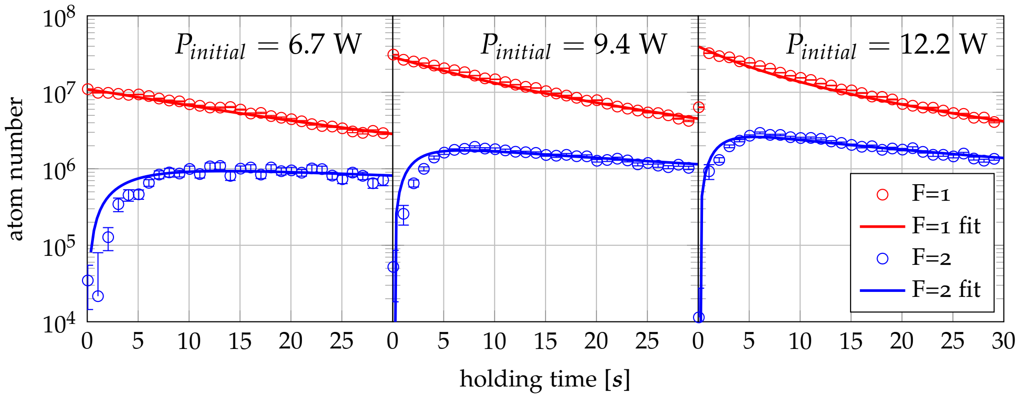

Figure A.1: Population of the F=1 and F=2 states over holding time in the trap for different powers. The solid line is a fit of the coupled-system loss rate equations solution to the acquired data.

$$\begin{aligned} \dot{N_1} &= -p(N_1 - N_2) - \beta_{11}\frac{N_1^2}{V_{eff}} - \beta_{12}\frac{N_1 N_2}{V_{eff}}, \\ \dot{N_2} &= +p(N_1 - N_2) - \beta_{22}\frac{N_2^2}{V_{eff}} - \beta_{12}\frac{N_1 N_2}{V_{eff}}, \end{aligned} \tag{A.1}$$

with $V_{eff} = (2\pi k_B T/m)^{3/2}/\bar{\omega}^3$ being the effective volume with $\bar{\omega}$ the mean trap frequency. The coefficients β_{ij} describe the two-body loss rates for collisions of atoms in the $F = i, j$ state. The impact of spontaneous Raman scattering [163] should be negligible in our setup since it scales with $1/\Delta^4$.

The pumping rate (p) is shown in **figure** A.2. The pumping rate increases with about $2.5 \times 10^{-3}\,\mathrm{W}^{-1}$. The dashed line in **figure** A.2 displays the spontaneous photon scattering in the trap. The hyperfine state changing scattering rate is expected to be orders of magnitude lower than the spontaneous photon scattering. Therefore it is likely that the broad bandwidth laser stimulates RAMAN transitions that change the hyperfine state.

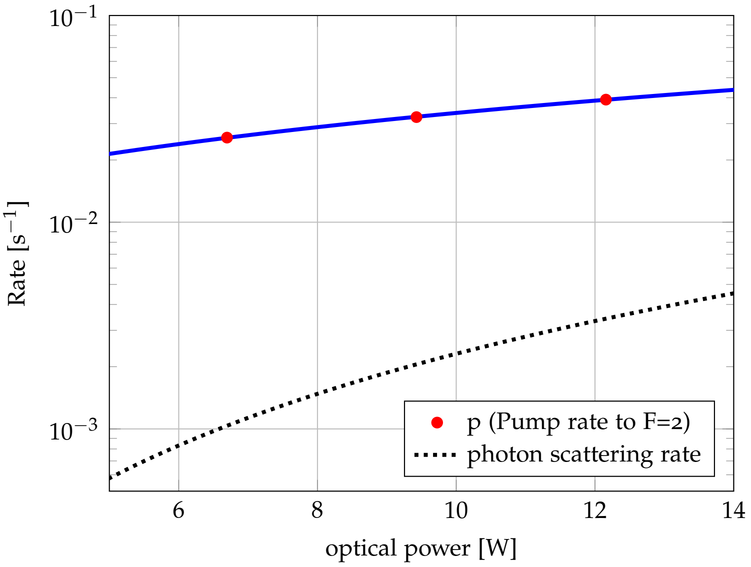

Figure A.2: Pump rate into F=2

A.2 2 µm LASER

The measurements presented in this work have been taken with two different lasers (Laser1 and 2). **Table** A.1 summarizes the lasers, which all deliver 50 W with a line width of 1 nm. The main difference between Laser1 and 2 are the construction year and the wavelength difference of 20 nm. Laser3 was borrowed from our cooperating experiment in Bremen to replace the broken Laser1. Unfortunately we observed high power fluctuations and could not operate the dipole trap with it. The two remaining lasers are prone to failures. **Figure** A.3 shows the time line of laser operation as well as the dates of the measurements presented in this work.

Laser	Product	Construction year	Wavelength [nm]
Laser1	IPG TLR-50-1960-LP	2007	1960
Laser2	IPG TLR-50-1940-LP	2016	1940
Laser3	IPG TLR-50-1940-LP	2016	1940

Table A.1: List of lasers used in this work.

A.2.1 *Characterization of the Laser*

Laser 2 was characterized before the system was set up. The beam diameter measurements are shown in **figure** A.4. To measure the profile of the beam, a razor blade is moved through the beam and the passing optical power behind the blade is measured. The measurement was performed by passing through the beam horizontally and vertically at different positions, **table** A.2, after the laser's output collimator. From the measurements of the beam diameter the transverse beam

Position	distance from collimator [cm]
1	38
2	77
3	122

Table A.2: Positions of beam profile measurement.

profile can be estimated, see **figure A.5**. The outcome of this measurement was used for the estimation of the center-position modulation in section 3.4.2.

A.3 CHARACTERIZATION OF THE AOM FOR 2 µm

The generation of time-averaged potential relies on the sweep of the diffraction angle of the AOM, see 2.2. **Figure A.6** shows the separation of the 0th and 1st order of the AOM output at a distance of 15 cm. The frequency dependent diffraction is shown in **graph A.7** also for a distance of 15 cm. The AOM used in the setup

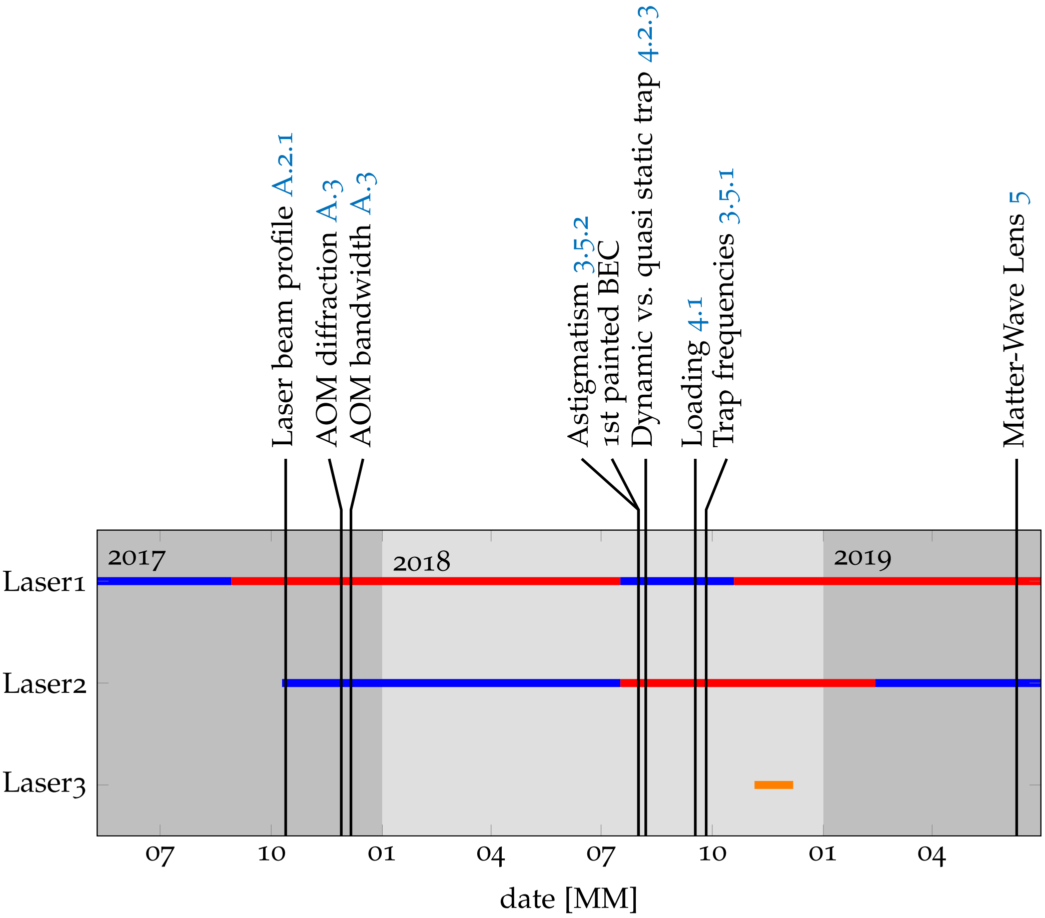

Figure A.3: Timeline of laser operation. The up-time is drawn in blue. Times of repair or failures are drawn in red. The orange line displays the time in which Laser 3 was tested. The black vertical lines mark the dates of the measurements.

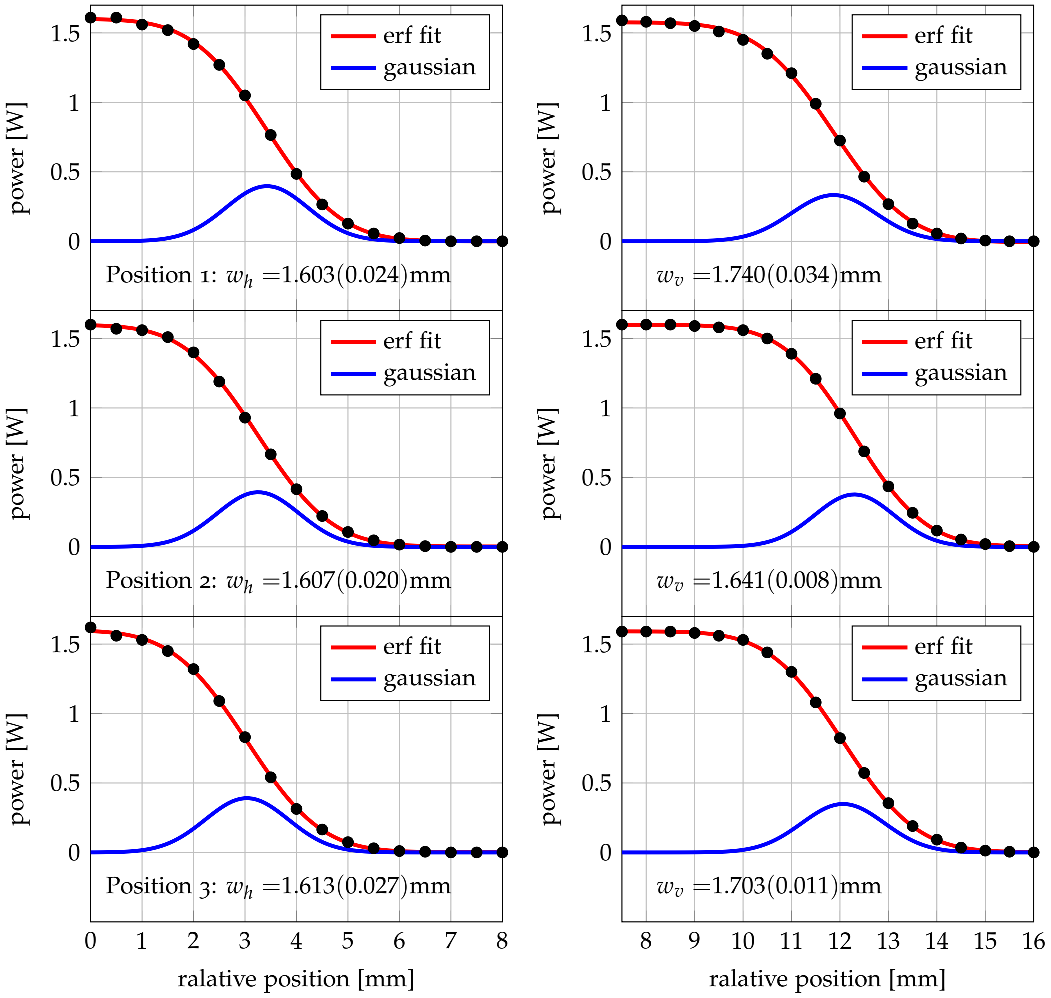

Figure A.4: Beam radius measurements of Laser 2. In red the power measured with the razor blade method. In blue the derivative of the error-function fit through data points.

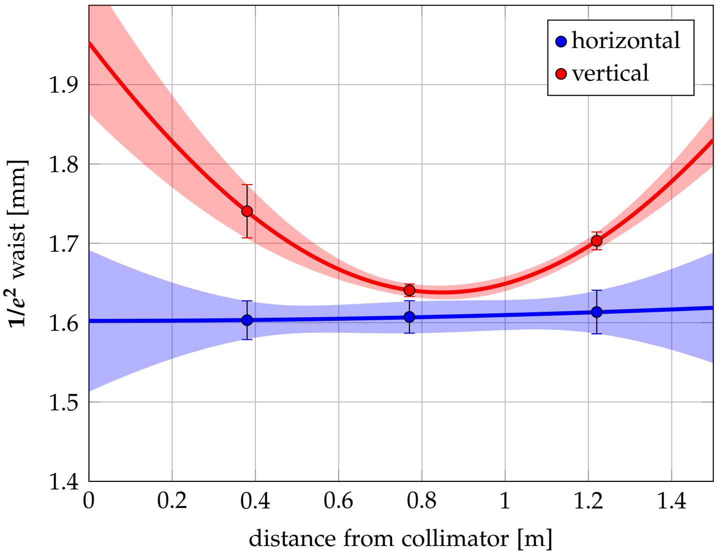

Figure A.5: Waist of the beam after the laser collimator and the corresponding fitted functions.

described in this thesis has a quite narrow frequency response. **Figure A.8** shows the diffraction efficiency over the RF-frequency. The RF-frequency is modulated with about ±4 MHz around the maximum. The narrow frequency response of the AOM will lead to amplitude modulations during the transit of the center-position modulation as shown in **figure 5.6**. There was no power variation of the **RF!** (**RF!**)-source observed over the modulated frequency range.

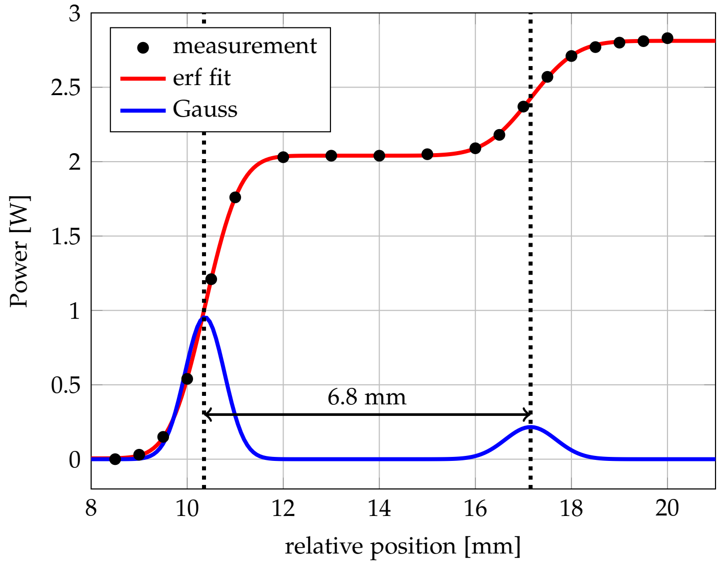

Figure A.6: Diffraction angle of AOM. In red the power measured with the razor blade method. In blue the derivative of the error-function fit through data points.

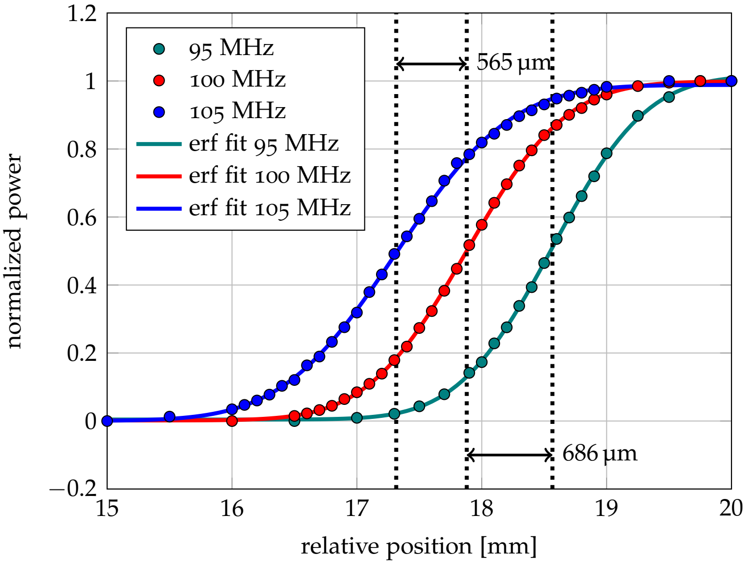

Figure A.7: Beam diffraction for different frequencies, measured with the razor blade method.

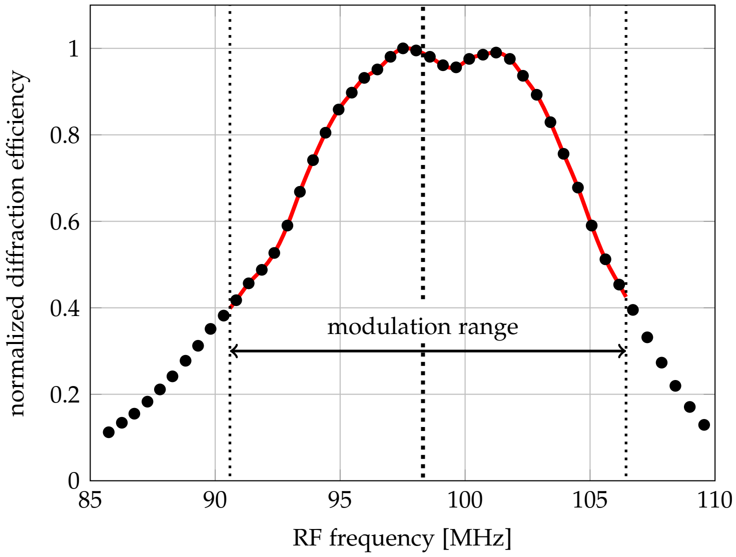

Figure A.8: Diffraction efficiency over frequency.

A.4 INPUT PARAMETERS FOR DKC SIMULATION

The simulation for the matter-wave lens displayed in 5.4 were performed using input values shown in **table** A.3. The detection angle is set to $14(1)^{\circ}$.

Set:		$\omega_x/2\pi$	$\omega_y/2\pi$	$\omega_z/2\pi$	$\sigma_{r,x}$	$\sigma_{r,y}$	$\sigma_{r,z}$	T_{3D}	N
	Unit:		Hz			µm		nK	
1	initial	142.8(15.5)	203.9(19.7)	777.9(35.5)	122.0(4.0)	59.9(2.0)	18.7(0.6)	37015.73(454.64)	$2.28(0.00) \times 10^7$
	lensed	83.9(9.7)	119.6(13.1)	656.9(30.0)	—	—	—	—	—
2	initial	131.8(13.4)	187.6(16.0)	557.3(25.5)	90.7(2.4)	44.7(1.2)	18.0(0.5)	17529.6(313.06)	$1.27(0.00) \times 10^7$
	lensed	53.7(6.2)	76.6(8.4)	420.4(19.2)	—	—	—	—	—
3	initial	164.9(15.9)	218.1(10.5)	268.9(12.4)	16.6(0.3)	9.5(0.2)	14.3(0.6)	3566.68(44.61)	$2.70(0.01) \times 10^6$
	lensed	52.3(5.7)	74.6(7.1)	268.3(12.3)	—	—	—	—	—
4	initial	138.0(14.9)	181.4(8.8)	209.9(9.8)	9.0(0.3)	5.2(0.2)	14.7(0.7)	876.33(8.78)	$7.70(0.02) \times 10^5$
	lensed	26.5(3.3)	37.8(4.2)	207.7(9.6)	—	—	—	—	—
5	initial	124.1(13.6)	162.7(8.0)	187.9(8.8)	3.3(0.2)	1.9(0.1)	12.4(0.7)	587.01(15.46)	$9.80(0.01) \times 10^5$
	lensed	24.0(3.1)	34.2(3.8)	187.9(8.7)	—	—	—	—	—
6	initial	111.7(12.5)	146.4(7.3)	168.9(8.0)	6.6(0.2)	3.8(0.1)	12.4(0.6)	282.0(6.82)	$8.70(0.10) \times 10^4$
	lensed	21.5(2.9)	30.6(3.4)	168.0(7.8)	—	—	—	—	—
7	initial	105.2(11.8)	137.9(6.9)	159.1(7.5)	3.3(0.1)	1.9(0.0)	11.0(0.3)	101.75(0.6)	$4.32(0.01) \times 10^5$
	lensed	20.3(2.8)	28.9(3.2)	158.8(7.4)	—	—	—	—	—

Table A.3: Input Parameters for the DKC Simulation

BIBLIOGRAPHY

[1] Thomas Young. “II. The Bakerian Lecture. On the theory of light and colours.” In: *Philosophical Transactions of the Royal Society of London* 92 (1802), pp. 12–48. DOI: 10.1098/rstl.1802.0004 (cit. on p. 1).

[2] Albert A. Michelson. “XXVIII. Interference phenomena in a new form of refractometer.” In: *The London, Edinburgh, and Dublin Philosophical Magazine and Journal of Science* 13.81 (1882), pp. 236–242. DOI: 10.1080/14786448208627176 (cit. on p. 1).

[3] Albert A. Michelson and Edward W. Morley. “LVIII. On the relative motion of the earth and the luminiferous Æther.” In: 24.151 (1887), pp. 449–463. DOI: 10.1080/14786448708628130 (cit. on p. 1).

[4] A. Einstein. “Zur Elektrodynamik bewegter Körper [AdP 17, 891 (1905)].” In: *Annalen der Physik* 14.S1 (2005), pp. 194–224. DOI: 10.1002/andp.200590006 (cit. on p. 1).

[5] Jagannath Nayak. “Fiber-optic gyroscopes: from design to production [Invited].” In: *Applied Optics* 50.25 (2011), E152. DOI: 10.1364/ao.50.00e152 (cit. on p. 1).

[6] C. Schubert et al. “Comparison of interferometric all-optical switches for demultiplexing applications in high-speed OTDM systems.” In: *Journal of Lightwave Technology* 20.4 (2002), pp. 618–624. DOI: 10.1109/50.996581 (cit. on p. 1).

[7] ESO. *The Very Large Telescope Interferometer*. Apr. 30, 2020. URL: http://www.eso.org/sci/facilities/paranal/telescopes/vlti.html (cit. on p. 1).

[8] Louis De Broglie. “Recherches sur la théorie des Quanta.” In: *Annales de Physique* 10.3 (1925), pp. 22–128. DOI: 10.1051/anphys/192510030022 (cit. on p. 1).

[9] G. Möllenstedt and H. Düker. “Fresnelscher Interferenzversuch mit einem Biprisma für Elektronenwellen.” In: *Die Naturwissenschaften* 42.2 (1955), pp. 41–41. DOI: 10.1007/bf00621530 (cit. on p. 1).

[10] H. Maier-Leibnitz and T. Springer. “Ein Interferometer für langsame Neutronen.” In: *Zeitschrift für Physik* 167.4 (1962), pp. 386–402. DOI: 10.1007/bf01378119 (cit. on p. 1).

[11] O. Carnal and J. Mlynek. “Young’s double-slit experiment with atoms: A simple atom interferometer.” In: *Physical Review Letters* 66.21 (1991), pp. 2689–2692. DOI: 10.1103/physrevlett.66.2689. URL: http://link.aps.org/doi/10.1103/PhysRevLett.66.2689 (cit. on p. 1).

[12] Mark Kasevich and Steven Chu. “Atomic interferometry using stimulated Raman transitions.” In: *Physical Review Letters* 67.2 (1991), pp. 181–184. DOI: 10.1103/physrevlett.67.181. URL: https://journals.aps.org/prl/abstract/10.1103/PhysRevLett.67.181 (cit. on pp. 1, 4).

[13] Sven Abend, Matthias Gersemann, Christian Schubert, Dennis Schlippert, Ernst M. Rasel, Matthias Zimmermann, Maxim A. Efremov, Albert Roura, Frank A. Narducci, and Wolfgang P. Schleich. "Atom interferometry and its applications." In: *Proceedings of the International School of Physics "Enrico Fermi" Course 197 "Foundations of Quantum Theory", edited by Ernst M. Rasel, Wolfgang P. Schleich, and Sabine Wölk (IOS, Amsterdam; SIF, Bologna; 2019), pp. 345-392* (Jan. 29, 2020). arXiv: `http://arxiv.org/abs/2001.10976v1 [physics.atom-ph]` (cit. on p. 1).

[14] G. W. Biedermann, X. Wu, L. Deslauriers, S. Roy, C. Mahadeswaraswamy, and M. A. Kasevich. "Testing gravity with cold-atom interferometers." In: *Physical Review A* 91.3 (2015). DOI: `10.1103/physreva.91.033629`. URL: `\url{http://link.aps.org/doi/10.1103/PhysRevA.91.033629}` (cit. on p. 1).

[15] M. Snadden, J. McGuirk, P. Bouyer, K. Haritos, and M. Kasevich. "Measurement of the Earth's Gravity Gradient with an Atom Interferometer-Based Gravity Gradiometer." In: *Physical Review Letters* 81.5 (1998), pp. 971–974. DOI: `10.1103/physrevlett.81.971`. URL: `\url{http://link.aps.org/doi/10.1103/PhysRevLett.81.971}` (cit. on p. 1).

[16] J. B. Fixler, G. T. Foster, J. M. McGuirk, and M. A. Kasevich. "Atom Interferometer Measurement of the Newtonian Constant of Gravity." In: *Science* 315.5808 (2007), pp. 74–77. DOI: `10.1126/science.1135459`. URL: `\url{http://www.sciencemag.org/content/315/5808/74}` (cit. on p. 1).

[17] G. Rosi, F. Sorrentino, L. Cacciapuoti, M. Prevedelli, and G. M. Tino. "Precision measurement of the Newtonian gravitational constant using cold atoms." In: *Nature* 510.7506 (2014), pp. 518–521. DOI: `10.1038/nature13433` (cit. on p. 1).

[18] Pierre Cladé, Estefania de Mirandes, Malo Cadoret, Saïda Guellati-Khélifa, Catherine Schwob, François Nez, Lucile Julien, and François Biraben. "Precise measurement h over mRb Bloch oscillations in a vertical optical lattice: Determination of the fine-structure constant." In: *Physical Review A* 74.5 (2006). DOI: `10.1103/physreva.74.052109` (cit. on p. 1).

[19] H. Müller, S.-W. Chiow, Q. Long, C. Vo, and S. Chu. "A new photon recoil experiment: towards a determination of the fine structure constant." In: *Applied Physics B* 84.4 (2006), pp. 633–642. DOI: `10.1007/s00340-006-2279-x` (cit. on p. 1).

[20] Rym Bouchendira, Pierre Cladé, Saïda Guellati-Khélifa, François Nez, and François Biraben. "New Determination of the Fine Structure Constant and Test of the Quantum Electrodynamics." In: *Physical Review Letters* 106.8 (2011). DOI: `10.1103/physrevlett.106.080801`. URL: `\url{http://link.aps.org/doi/10.1103/PhysRevLett.106.080801}` (cit. on p. 1).

[21] D. Hanneke, S. Fogwell, and G. Gabrielse. "New Measurement of the Electron Magnetic Moment and the Fine Structure Constant." In: *Physical Review Letters* 100.12 (2008). DOI: `10.1103/physrevlett.100.120801`. URL: `http://link.aps.org/doi/10.1103/PhysRevLett.100.120801` (cit. on p. 1).

[22] T. L. Gustavson, P. Bouyer, and M. A. Kasevich. “Precision Rotation Measurements with an Atom Interferometer Gyroscope.” In: *Physical Review Letters* 78.11 (1997), pp. 2046–2049. DOI: `10.1103/physrevlett.78.2046`. URL: `\url{http://link.aps.org/doi/10.1103/PhysRevLett.78.2046}` (cit. on p. 1).

[23] P. Berg, S. Abend, G. Tackmann, C. Schubert, E. Giese, W. P. Schleich, F. A. Narducci, W. Ertmer, and E. M. Rasel. “Composite-Light-Pulse Technique for High-Precision Atom Interferometry.” In: *Physical Review Letters* 114.6 (2015). DOI: `10.1103/physrevlett.114.063002` (cit. on p. 1).

[24] A. Gauguet, B. Canuel, T. Lévèque, W. Chaibi, and A. Landragin. “Characterization and limits of a cold-atom Sagnac interferometer.” In: *Physical Review A* 80.6 (2009). DOI: `10.1103/physreva.80.063604` (cit. on p. 1).

[25] Achim Peters, Keng Yeow Chung, and Steven Chu. “Measurement of gravitational acceleration by dropping atoms.” In: *Nature* 400.6747 (1999), pp. 849–852. ISSN: 0028-0836. DOI: `10.1038/23655`. URL: `http://dx.doi.org/10.1038/23655` (cit. on p. 1).

[26] Hayden J. McGuinness, Akash V. Rakholia, and Grant W. Biedermann. “High data-rate atom interferometer for measuring acceleration.” In: *Applied Physics Letters* 100.1 (2012), p. 011106. DOI: `10.1063/1.3673845`. URL: `\url{http://dx.doi.org/10.1063/1.3673845}` (cit. on p. 1).

[27] V. N. Baryshev and I. Yu. Blinov. “Application of Atomic Interferometers in Gravimetry.” In: *Measurement Techniques* 57.12 (2015), pp. 1333–1337. DOI: `10.1007/s11018-015-0630-5` (cit. on p. 1).

[28] B Barrett, A Bertoldi, and P Bouyer. “Inertial quantum sensors using light and matter.” In: *Physica Scripta* 91.5 (2016), p. 053006. DOI: `10.1088/0031-8949/91/5/053006`. URL: `https://doi.org/10.1088%2F0031-8949%2F91%2F5%2F053006` (cit. on p. 1).

[29] J. M. McGuirk, G. T. Foster, J. B. Fixler, M. J. Snadden, and M. A. Kasevich. “Sensitive absolute-gravity gradiometry using atom interferometry.” In: *Physical Review A* 65.3 (2002). DOI: `10.1103/physreva.65.033608`. URL: `http://link.aps.org/doi/10.1103/PhysRevA.65.033608` (cit. on p. 1).

[30] G. Lamporesi, A. Bertoldi, L. Cacciapuoti, M. Prevedelli, and G. M. Tino. “Determination of the Newtonian Gravitational Constant Using Atom Interferometry.” In: *Physical Review Letters* 100.5 (2008). DOI: `10.1103/physrevlett.100.050801`. URL: `http://link.aps.org/doi/10.1103/PhysRevLett.100.050801` (cit. on p. 1).

[31] Ludwig Zehnder. “Ein neuer Interferenzrefraktor.” In: *11. Jahrgang* 11. (1891). Ed. by A. Westphal, pp. 275–285. URL: `https://archive.org/details/zeitschriftfrin11gergoog/page/n289` (visited on 12/05/2019) (cit. on p. 1).

[32] Ludwig Mach. “Über einen Interferenzrefraktor.” In: *12. Jahrgang* 12 (1892). Ed. by A. Westphal, pp. 89–93. URL: `https://archive.org/details/zeitschriftfrin14gergoog/page/n103` (visited on 12/05/2019) (cit. on p. 1).

[33] P Gillot, O Francis, A Landragin, F Pereira Dos Santos, and S Merlet. “Stability comparison of two absolute gravimeters: optical versus atomic interferometers.” In: *Metrologia* 51.5 (2014), pp. L15–L17. DOI: `10.1088/0026-1394/51/5/l15` (cit. on p. 2).

[34] R. P. Middlemiss, A. Samarelli, D. J. Paul, J. Hough, S. Rowan, and G. D. Hammond. “Measurement of the Earth tides with a MEMS gravimeter.” In: *Nature* 531.7596 (2016), pp. 614–617. DOI: `10.1038/nature17397` (cit. on p. 2).

[35] A. Einstein. “Die Grundlage der allgemeinen Relativitätstheorie.” In: *Ann. Phys.* 49 (1916), pp. 769–822 (cit. on p. 2).

[36] Donato Bramanti. “Perihelion Precession of Mercury.” In: *Nature* 219.5149 (1968), pp. 47–48. DOI: `10.1038/219047a0` (cit. on p. 2).

[37] C. Davidson Frank Watson Dyson Arthur Stanley Eddington. “IX. A determination of the deflection of light by the sun’s gravitational field, from observations made at the total eclipse of May 29, 1919.” In: *Philosophical Transactions of the Royal Society of London. Series A, Containing Papers of a Mathematical or Physical Character* 220.571-581 (1920), pp. 291–333. DOI: `10.1098/rsta.1920.0009` (cit. on p. 2).

[38] A. Einstein. “Über Gravitationswellen.” In: *Sitzungsbericht Kgl. Preuss. Akad. Wiss.* (1918) (cit. on p. 2).

[39] B. P. Abbott et al. “Observation of Gravitational Waves from a Binary Black Hole Merger.” In: *Physical Review Letters* 116.6 (Feb. 2016). DOI: `10.1103/physrevlett.116.061102` (cit. on p. 3).

[40] A. Einstein. “Prinzipielles zur allgemeinen Relativitätstheorie [AdP 55, 241 (1918)].” In: *Annalen der Physik* 14.S1 (2005), pp. 577–581. DOI: `10.1002/andp.200590046` (cit. on p. 3).

[41] C. Lämmerzahl. “The search for quantum gravity effects I.” In: *Applied Physics B* 84.4 (2006), pp. 551–562. ISSN: 0946-2171. DOI: `10.1007/s00340-006-2374-z`. URL: `\url{http://dx.doi.org/10.1007/s00340-006-2374-z}` (cit. on p. 3).

[42] David Mattingly. “Modern Tests of Lorentz Invariance.” In: *Living Reviews in Relativity* 8.1 (Dec. 3, 2019). DOI: `10.12942/lrr-2005-5` (cit. on p. 3).

[43] Pacôme Delva et al. “A new test of gravitational redshift using Galileo satellites: The GREAT experiment.” In: *Comptes Rendus Physique* 20.3 (2019), pp. 176–182. DOI: `10.1016/j.crhy.2019.04.002` (cit. on p. 3).

[44] Galileo Galilei. *Unterredungen und mathematische Demonstrationen über zwei neue Wissenszweige, die Mechanik und die Fallgesetze betreffend. Arcetri, 6. März 1638 / von Galileo Galilei. Aus dem Ital. und Latein. übers. und hrsg. von Arthur von Oettingen ; [1]: Erster und zweiter Tag*. Deutsch, Italienisch, Latein. Trans. Italian by Arthur J. Oettingen. Leipzig: Engelmann, 1890, p. 142. URL: `https://archive.org/details/unterredungenun00oettgoog/page/n2/mode/2up` (visited on 02/05/2020) (cit. on p. 3).

[45] Loránd Eötvös. "Über die Anziehung der Erde auf verschiedene Substanzen. Mathematische und naturwissenschaftliche Berichte aus Ungarn." In: Bd.8: Oct.1889-Oct.1890 (1891) (1890). Ed. by Königliche Ungarische naturwissenschaftliche Gesellschaft. and Magyar Tudományos Akadémia., pp. 65–68. URL: `https://www.biodiversitylibrary.org/item/97254` (cit. on p. 3).

[46] S. Schlamminger, K.-Y. Choi, T. A. Wagner, J. H. Gundlach, and E. G. Adelberger. "Test of the Equivalence Principle Using a Rotating Torsion Balance." In: *Physical Review Letters* 100.4 (2008). DOI: `10.1103/physrevlett.100.041101`. URL: `\url{http://link.aps.org/doi/10.1103/PhysRevLett.100.041101}` (cit. on p. 3).

[47] F Hofmann and J Müller. "Relativistic tests with lunar laser ranging." In: *Classical and Quantum Gravity* 35.3 (2018), p. 035015. DOI: `10.1088/1361-6382/aa8f7a` (cit. on p. 3).

[48] Pierre Touboul et al. "MICROSCOPE Mission: First Results of a Space Test of the Equivalence Principle." In: *Physical Review Letters* 119.23 (2017). DOI: `10.1103/physrevlett.119.231101` (cit. on p. 3).

[49] T. M. Niebauer, M. P. McHugh, and J. E. Faller. "Galilean test for the fifth force." In: *Physical Review Letters* 59.6 (1987), pp. 609–612. DOI: `10.1103/physrevlett.59.609`. URL: `\url{http://link.aps.org/doi/10.1103/PhysRevLett.59.609}` (cit. on p. 3).

[50] H. Albers et al. "Quantum test of the Universality of Free Fall using rubidium and potassium." In: (Mar. 2, 2020). DOI: `10.1140/epjd/e2020-10132-6`. arXiv: `http://arxiv.org/abs/2003.00939v1 [physics.atom-ph]` (cit. on pp. 4, 63).

[51] S Merlet, Q Bodart, N Malossi, A Landragin, F Pereira Dos Santos, O Gitlein, and L Timmen. "Comparison between two mobile absolute gravimeters: optical versus atomic interferometers." In: *Metrologia* 47.4 (2010), pp. L9–L11. DOI: `10.1088/0026-1394/47/4/l01` (cit. on p. 4).

[52] Ke Zhang, Min-Kang Zhou, Yuan Cheng, Le-Le Chen, Qin Luo, Wen-Jie Xu, Lu-Shuai Cao, Xiao-Chun Duan, and Zhong-Kun Hu. "Testing the Universality of Free Fall at 10^{-10} level by Comparing the Atoms in Different Hyperfine States with Bragg Diffraction." In: (May 20, 2018). arXiv: `http://arxiv.org/abs/1805.07758v2 [quant-ph]` (cit. on p. 4).

[53] Lin Zhou et al. "Test of Equivalence Principle at 10^{-8} Level by a Dual-Species Double-Diffraction Raman Atom Interferometer." In: *Physical Review Letters* 115.1 (2015). DOI: `10.1103/physrevlett.115.013004`. URL: `http://link.aps.org/doi/10.1103/PhysRevLett.115.013004` (cit. on p. 4).

[54] Luca Pezzè, Augusto Smerzi, Markus K. Oberthaler, Roman Schmied, and Philipp Treutlein. "Quantum metrology with nonclassical states of atomic ensembles." In: *Reviews of Modern Physics* 90.3 (2018). DOI: `10.1103/revmodphys.90.035005` (cit. on p. 4).

[55] Onur Hosten, Nils J. Engelsen, Rajiv Krishnakumar, and Mark A. Kasevich. "Measurement noise 100 times lower than the quantum-projection limit using entangled atoms." In: *Nature* 529.7587 (2016), pp. 505–508. DOI: `10.1038/nature16176` (cit. on p. 4).

[56] Leonardo Salvi, Nicola Poli, Vladan Vuletić, and Guglielmo M. Tino. "Squeezing on Momentum States for Atom Interferometry." In: *Physical Review Letters* 120.3 (2018). DOI: `10.1103/physrevlett.120.033601` (cit. on p. 4).

[57] I. Kruse et al. "Improvement of an Atomic Clock using Squeezed Vacuum." In: *Physical Review Letters* 117.14 (2016). DOI: `10.1103/physrevlett.117.143004` (cit. on p. 4).

[58] C. V. Raman and N. S. Nagendra Nathe. "The diffraction of light by high frequency sound waves: Part I." In: *Proceedings of the Indian Academy of Sciences - Section A* 2.4 (1935), pp. 406–412. DOI: `10.1007/bf03035840` (cit. on p. 4).

[59] David L. Butts, Krish Kotru, Joseph M. Kinast, Antonije M. Radojevic, Brian P. Timmons, and Richard E. Stoner. "Efficient broadband Raman pulses for large-area atom interferometry." In: *Journal of the Optical Society of America B* 30.4 (2013), p. 922. DOI: `10.1364/josab.30.000922` (cit. on p. 4).

[60] M. Kozuma, L. Deng, E. W. Hagley, J. Wen, R. Lutwak, K. Helmerson, S. L. Rolston, and W. D. Phillips. "Coherent Splitting of Bose-Einstein Condensed Atoms with Optically Induced Bragg Diffraction." In: *Physical Review Letters* 82.5 (1999), pp. 871–875. DOI: `10.1103/physrevlett.82.871` (cit. on p. 4).

[61] T. Lévèque, A. Gauguet, F. Michaud, F. Pereira Dos Santos, and A. Landragin. "Enhancing the Area of a Raman Atom Interferometer Using a Versatile Double-Diffraction Technique." In: *Physical Review Letters* 103.8 (2009). DOI: `10.1103/physrevlett.103.080405` (cit. on p. 4).

[62] Felix Bloch. "Über die Quantenmechanik der Elektronen in Kristallgittern." In: *Zeitschrift für Physik* 52.7-8 (1929), pp. 555–600. DOI: `10.1007/bf01339455` (cit. on p. 4).

[63] Pierre Cladé, Saïda Guellati-Khélifa, François Nez, and François Biraben. "Large Momentum Beam Splitter Using Bloch Oscillations." In: *Physical Review Letters* 102.24 (2009). DOI: `10.1103/physrevlett.102.240402` (cit. on p. 4).

[64] Martina Gebbe et al. "Twin-lattice atom interferometry." In: (July 19, 2019). arXiv: `http://arxiv.org/abs/1907.08416v1 [quant-ph]` (cit. on p. 5).

[65] J Hartwig, S Abend, C Schubert, D Schlippert, H Ahlers, K Posso-Trujillo, N Gaaloul, W Ertmer, and E M Rasel. "Testing the universality of free fall with rubidium and ytterbium in a very large baseline atom interferometer." In: *New Journal of Physics* 17.3 (2015), p. 035011. DOI: `10.1088/1367-2630/17/3/035011` (cit. on pp. 5, 6, 43).

[66] D. Schlippert et al. "Ground Tests of Einstein's Equivalence Principle: From Lab-based to 10-m Atomic Fountains." In: (July 21, 2015). arXiv: `http://arxiv.org/abs/1507.05820v1 [physics.atom-ph]` (cit. on pp. 5, 43).

[67] H. Müntinga et al. “Interferometry with Bose-Einstein Condensates in Microgravity.” In: *Physical Review Letters* 110.9 (2013). DOI: `10.1103/physrevlett.110.093602` (cit. on pp. 5–7).

[68] Christian Vogt, Marian Woltmann, Henning Albers, Dennis Schlippert, Sven Herrmann, Ernst M. Rasel, and Claus Lämmerzahl. “Evaporative cooling from an optical dipole trap in microgravity.” In: (Sept. 9, 2019). arXiv: `http://arxiv.org/abs/1909.03800v1 [physics.atom-ph]` (cit. on pp. 5, 65).

[69] G. Condon et al. “All-Optical Bose-Einstein Condensates in Microgravity.” In: *Physical Review Letters* 123.24 (2019). DOI: `10.1103/physrevlett.123.240402` (cit. on pp. 5, 6, 47).

[70] Christoph Lotz, Yvonne Wessarges, Jörg Hermsdorf, Wolfgang Ertmer, and Ludger Overmeyer. “Novel active driven drop tower facility for microgravity experiments investigating production technologies on the example of substrate-free additive manufacturing.” In: *Advances in Space Research* 61.8 (2018), pp. 1967–1974. DOI: `10.1016/j.asr.2018.01.010` (cit. on p. 5).

[71] Brynle Barrett, Laura Antoni-Micollier, Laure Chichet, Baptiste Battelier, Thomas Lévèque, Arnaud Landragin, and Philippe Bouyer. “Dual Matter-Wave Inertial Sensors in Weightlessness.” In: *Nat. Commun. 7, 13786 (2016)* (Sept. 12, 2016). DOI: `10.1038/ncomms13786` (cit. on p. 5).

[72] Dennis Becker et al. “Space-borne Bose–Einstein condensation for precision interferometry.” In: *Nature* 562.7727 (2018), pp. 391–395. DOI: `10.1038/s41586-018-0605-1` (cit. on pp. 5, 46).

[73] Maike Lachmann. *Atom Interferometrie on first MAIUS flight*. private communication. 2020 (cit. on p. 5).

[74] N. Lundblad, R. A. Carollo, C. Lannert, M. J. Gold, X. Jiang, D. Paseltiner, N. Sergay, and D. C. Aveline. “Shell potentials for microgravity Bose–Einstein condensates.” In: *npj Microgravity* 5.1 (2019). DOI: `10.1038/s41526-019-0087-y` (cit. on p. 5).

[75] Kai Frye et al. “The Bose-Einstein Condensate and Cold Atom Laboratory.” In: (Dec. 10, 2019). arXiv: `http://arxiv.org/abs/1912.04849 [physics.atom-ph]` (cit. on pp. 5, 46).

[76] Harald F. Hess. “Evaporative cooling of magnetically trapped and compressed spin-polarized hydrogen.” In: *Physical Review B* 34.5 (1986), pp. 3476–3479. DOI: `10.1103/physrevb.34.3476` (cit. on p. 5).

[77] Wolfgang Ketterle and N.J. Van Druten. “Evaporative Cooling of Trapped Atoms.” In: *Advances In Atomic, Molecular, and Optical Physics*. Elsevier, 1996, pp. 181–236. DOI: `10.1016/s1049-250x(08)60101-9` (cit. on p. 5).

[78] Kendall B. Davis, Marc-Oliver Mewes, Michael A. Joffe, Michael R. Andrews, and Wolfgang Ketterle. “Evaporative Cooling of Sodium Atoms.” In: *Physical Review Letters* 74.26 (1995), pp. 5202–5205. DOI: `10.1103/physrevlett.74.5202` (cit. on p. 5).

[79] Charles S. Adams, Heun Jin Lee, Nir Davidson, Mark Kasevich, and Steven Chu. "Evaporative Cooling in a Crossed Dipole Trap." In: *Physical Review Letters* 74.18 (1995), pp. 3577–3580. DOI: `10.1103/physrevlett.74.3577` (cit. on p. 5).

[80] D. J. Han. "Microwave-induced Evaporation in a Crossed Dipole Trap." In: *Journal of the Physical Society of Japan* 76.2 (2007), p. 023301. DOI: `10.1143/jpsj.76.023301` (cit. on p. 5).

[81] I. D. Setija, H. G. C. Werij, O. J. Luiten, M. W. Reynolds, T. W. Hijmans, and J. T. M. Walraven. "Optical cooling of atomic hydrogen in a magnetic trap." In: *Physical Review Letters* 70.15 (1993), pp. 2257–2260. DOI: `10.1103/physrevlett.70.2257` (cit. on p. 5).

[82] Naoto Masuhara, John M. Doyle, Jon C. Sandberg, Daniel Kleppner, Thomas J. Greytak, Harald F. Hess, and Greg P. Kochanski. "Evaporative Cooling of Spin-Polarized Atomic Hydrogen." In: *Physical Review Letters* 61.8 (1988), pp. 935–938. DOI: `10.1103/physrevlett.61.935` (cit. on p. 5).

[83] Richard Roy, Alaina Green, Ryan Bowler, and Subhadeep Gupta. "Rapid cooling to quantum degeneracy in dynamically shaped atom traps." In: *Phys. Rev. A* 93 (4 2016), p. 043403. DOI: `10.1103/PhysRevA.93.043403`. URL: `https://link.aps.org/doi/10.1103/PhysRevA.93.043403` (cit. on pp. 6, 11, 13, 39, 47).

[84] A. Einstein. *Quantentheorie des einatomigen idealen Gases. Zweite Abhandlung*. 1924. DOI: `10.1002/3527608958.ch28` (cit. on p. 6).

[85] Bose. "Plancks Gesetz und Lichtquantenhypothese." In: *Zeitschrift fuer Physik* 26.1 (1924), pp. 178–181. DOI: `10.1007/bf01327326`. URL: `https://doi.org/10.1007/BF01327326` (cit. on p. 6).

[86] M.H. Anderson, J.R. Ensher, M.R. Matthews, C.E. Wieman, and E.A. Cornell. "Observation of Bose-Einstein Condensation in a Dilute Atomic Vapor." In: *Science* 269.5221 (1995), pp. 198–201. DOI: `10.1126/science.269.5221.198`. eprint: `\url{http://www.sciencemag.org/cgi/reprint/269/5221/198.pdf}`. URL: `\url{http://www.sciencemag.org/cgi/content/abstract/269/5221/198}` (cit. on pp. 6, 46).

[87] K.B. Davis, M.-O. Mewes, M.R. Andrews, N.J. van Druten, D.S. Durfee, D.M. Kurn, and W. Ketterle. "Bose-Einstein Condensation in a Gas of Sodium Atoms." In: *Phys. Rev. Lett.* 75.22 (1995), pp. 3969–3973. DOI: `10.1103/PhysRevLett.75.3969` (cit. on pp. 6, 46, 47).

[88] C. C. Bradley, C. A. Sackett, J. J. Tollett, and R. G. Hulet. "Evidence of Bose-Einstein Condensation in an Atomic Gas with Attractive Interactions." In: *Physical Review Letters* 75.9 (1995), pp. 1687–1690. DOI: `10.1103/physrevlett.75.1687`. URL: `http://link.aps.org/doi/10.1103/PhysRevLett.75.1687` (cit. on pp. 6, 46).

[89] Ketterle W., Durfee D.S., and Stamper-Kurn D.M. “Making, probing and understanding Bose-Einstein condensates.” In: *Proceedings of the International School of Physics &ldquo;Enrico Fermi&rdquo;* 140.Bose-Einstein Condensation in Atomic Gases (1999), pp. 67–176. ISSN: 0074-784X. DOI: 10.3254/978-1-61499-225-7-67 (cit. on pp. 6, 35, 37, 46).

[90] S S Szigeti, J E Debs, J J Hope, N P Robins, and J D Close. “Why momentum width matters for atom interferometry with Bragg pulses.” In: *New Journal of Physics* 14.2 (2012), p. 023009. DOI: 10.1088/1367-2630/14/2/023009. URL: \url{http://stacks.iop.org/1367-2630/14/i=2/a=023009} (cit. on p. 6).

[91] M. R. Andrews. “Observation of Interference Between Two Bose Condensates.” In: *Science* 275.5300 (1997), pp. 637–641. DOI: 10.1126/science.275.5300.637. eprint: \url{http://www.sciencemag.org/cgi/reprint/275/5300/637.pdf}. URL: \url{http://www.sciencemag.org/cgi/content/abstract/275/5300/637} (cit. on p. 6).

[92] Y. Shin, M. Saba, T. A. Pasquini, W. Ketterle, D. E. Pritchard, and A. E. Leanhardt. “Atom Interferometry with Bose-Einstein Condensates in a Double-Well Potential.” In: *Physical Review Letters* 92.5 (2004), p. 050405. DOI: 10.1103/physrevlett.92.050405. URL: http://link.aps.org/doi/10.1103/PhysRevLett.92.050405 (cit. on p. 6).

[93] Susannah M. Dickerson, Jason M. Hogan, Alex Sugarbaker, David M. S. Johnson, and Mark A. Kasevich. “Multiaxis Inertial Sensing with Long-Time Point Source Atom Interferometry.” In: *Physical Review Letters* 111.8 (2013). DOI: 10.1103/physrevlett.111.083001 (cit. on pp. 6, 7).

[94] S. Chu, J. E. Bjorkholm, A. Ashkin, J. P. Gordon, and L. W. Hollberg. “Proposal for optically cooling atoms to temperatures of the order of 10^{-6} K.” In: *Optics Letters* 11.2 (1986), p. 73. DOI: 10.1364/ol.11.000073 (cit. on pp. 6, 7, 50).

[95] H. Ammann and N. Christensen. “Delta Kick Cooling: A New Method for Cooling Atoms.” In: *Phys. Rev. Lett.* 78 (1997), pp. 2088–2091. DOI: 10.1103/PhysRevLett.78.2088. URL: http://link.aps.org/doi/10.1103/PhysRevLett.78.2088 (cit. on p. 6).

[96] M. Morinaga, I. Bouchoule, J.-C. Karam, and C. Salomon. “Manipulation of Motional Quantum States of Neutral Atoms.” In: *Physical Review Letters* 83.20 (1999), pp. 4037–4040. DOI: 10.1103/physrevlett.83.4037 (cit. on p. 6).

[97] S. H. Myrskog, J. K. Fox, H. S. Moon, J. B. Kim, and A. M. Steinberg. “Modified “δ-kick cooling” using magnetic field gradients.” In: *Physical Review A* 61.5 (2000). DOI: 10.1103/physreva.61.053412 (cit. on p. 6).

[98] T. Aoki, T. Kato, Y. Tanami, and H. Nakamatsu. “δ-kick cooling using the Ioffe-Pritchard potential.” In: vol. 73. 6. American Physical Society (APS), 2006. DOI: 10.1103/physreva.73.063603 (cit. on p. 6).

[99] Tian Luan, Yufan Li, Xuesong Zhang, and Xuzong Chen. “Realization of two-stage crossed beam cooling and the comparison with Delta-kick cooling in experiment.” In: *Review of Scientific Instruments* 89.12 (2018), p. 123110. DOI: 10.1063/1.5046815 (cit. on p. 6).

[100] F. L. Moore, J. C. Robinson, C. F. Bharucha, Bala Sundaram, and M. G. Raizen. "Atom Optics Realization of the Quantum Delta-Kicked Rotor." In: *Physical Review Letters* 75.25 (1995), pp. 4598–4601. DOI: `10.1103/physrevlett.75.4598` (cit. on p. 6).

[101] Tim Kovachy, Jason M. Hogan, Alex Sugarbaker, Susannah M. Dickerson, Christine A. Donnelly, Chris Overstreet, and Mark A. Kasevich. "Matter Wave Lensing to Picokelvin Temperatures." In: *Physical Review Letters* 114.14 (2015). DOI: `10.1103/physrevlett.114.143004` (cit. on pp. 6, 7).

[102] J. Rudolph. "Matter-Wave Optics with Bose-Einstein Condensates in Microgravity." Dissertation. Leibniz Universität Hannover, 2016 (cit. on p. 7).

[103] Christoph Grzeschik. "Experiments with Bose-Einstein Condensates in Microgravity." PhD thesis. Humboldt-Universität zu Berlin, Mathematisch-Naturwissenschaftliche Fakultät, 2017. DOI: `http://dx.doi.org/10.18452/18037`. URL: `https://edoc.hu-berlin.de/handle/18452/18701` (cit. on p. 7).

[104] Tammo Sternke. "An ultracold high-flux source for matter-wave interferometry in microgravity." PhD thesis. 2018. URL: `http://oops.uni-oldenburg.de/3576/` (cit. on p. 7).

[105] G. D. McDonald, C. C. N. Kuhn, S. Bennetts, J. E. Debs, K. S. Hardman, M. Johnsson, J. D. Close, and N. P. Robins. "$80\hbar k$ momentum separation with Bloch oscillations in an optically guided atom interferometer." In: *Physical Review A* 88.5 (2013). DOI: `10.1103/physreva.88.053620` (cit. on p. 7).

[106] Susannah Moore Dickerson. "Long-Time Atom Interferometry for Precision Tests of Fundamental Physics." PhD thesis. 2014. URL: `http://web.stanford.edu/group/kasevich/cgi-bin/wordpress/wp-content/uploads/2016/10/DickersonThesis_WebVersion.pdf` (cit. on p. 7).

[107] Richard J. Roy. "Ytterbium and Lithium Quantum Gases:Heteronuclear Molecules and Bose-Fermi Superuid Mixtures." PhD thesis. 2017 (cit. on p. 11).

[108] Rudolf Grimm, Matthias Weidemüller, and Yurii B. Ovchinnikov. "Optical Dipole Traps for Neutral Atoms." In: *Advances In Atomic, Molecular, and Optical Physics*. Vol. 42. Elsevier, 2000, pp. 95–170. DOI: `10.1016/s1049-250x(08)60186-x` (cit. on p. 11).

[109] M. Zaiser. "Eine Quelle quantenentarteter Gase für die Atominterferometrie." Dissertation. Leibniz Universität Hannover, 2010 (cit. on pp. 11, 17, 33).

[110] D. Schlippert. "Quantum test of the Universality of Free Fall." Dissertation. Leibniz Universität Hannover, 2014. URL: `http://nbn-resolving.de/urn:nbn:de:gbv:089-8070795375` (cit. on pp. 17, 18).

[111] J.M. Hartwig. "Analyse eines atomaren Gravimeters hinsichtlich eines Quantentests des Äquivalenzprinzips." Dissertation. Leibniz Universität Hannover, 2013. URL: `http://nbn-resolving.de/urn:nbn:de:gbv:089-73556132X9` (cit. on p. 17).

[112] L. Richardson. “Inertial Noise Post-Correction in Atom Interferometers Measuring the Local Gravitational Acceleration.” Dissertation. Leibniz Universität Hannover, 2018 (cit. on p. 17).

[113] Daniel Adam Steck. “Rubidium 87 D Line Data. revision 2.2.1, 21 November 2019.” In: 2019. URL: `https://steck.us/alkalidata/` (visited on 12/19/2019) (cit. on p. 18).

[114] R Corgier, S Amri, W Herr, H Ahlers, J Rudolph, D Guéry-Odelin, E M Rasel, E Charron, and N Gaaloul. “Fast manipulation of Bose–Einstein condensates with an atom chip.” In: *New J. Phys.* 20.5 (May 2018), p. 055002. DOI: `10.1088/1367-2630/aabdfc` (cit. on p. 21).

[115] J. Matthias. “Analyse einer optischen Dipolfalle für Kalium und Rubidium als Quelle für die Atominterferometrie.” Diplomarbeit. Leibniz Universität Hannover, 2013 (cit. on pp. 23, 59).

[116] K Henderson, C Ryu, C MacCormick, and M G Boshier. “Experimental demonstration of painting arbitrary and dynamic potentials for Bose–Einstein condensates.” In: *New Journal of Physics* 11.4 (2009), p. 043030. DOI: `10.1088/1367-2630/11/4/043030` (cit. on p. 27).

[117] S. Friebel, C. D’Andrea, J. Walz, M. Weitz, and T. W. Hänsch. “$CO2$-laser optical lattice with cold rubidium atoms.” In: *Phys. Rev. A* 57.1 (Jan. 1998), R20–R23. DOI: `10.1103/PhysRevA.57.R20` (cit. on p. 27).

[118] D. Meschede. *Optik, Licht und Laser*. 3. Teubner, 2008. ISBN: 978-3-8351-0143-2 (cit. on p. 31).

[119] Wolfgang Petrich, Michael H. Anderson, Jason R. Ensher, and Eric A. Cornell. “Behavior of atoms in a compressed magneto-optical trap.” In: *J. Opt. Soc. Am. B* 11.8 (1994), pp. 1332–1335. URL: `\url{http://josab.osa.org/abstract.cfm?URI=josab-11-8-1332}` (cit. on p. 33).

[120] D. Schlippert. “Bose-Einstein-Kondensation in einer optischen Dipolfalle bei einer Wellenlänge von 2 μm.” Diplomarbeit. Leibniz Universität Hannover, 2010. URL: `https://www.iqo.uni-hannover.de/fileadmin/iqo/Forschung/Publikationen/Diplomarbeit_Dennis_Schlippert.pdf` (cit. on pp. 33, 59).

[121] Paul D. Lett, Richard N. Watts, Christoph I. Westbrook, William D. Phillips, Phillip L. Gould, and Harold J. Metcalf. “Observation of Atoms Laser Cooled below the Doppler Limit.” In: *Physical Review Letters* 61.2 (1988), pp. 169–172. DOI: `10.1103/physrevlett.61.169` (cit. on p. 33).

[122] Normand Laurendeau. *Statistical Thermodynamics*. Cambridge University Press, 2005, pp. 289–300. DOI: `10.1017/cbo9780511815928` (cit. on p. 34).

[123] Marc-Oliver Mewes. “Bose-Einstein condensation of sodium atoms.” PhD thesis. Massachusetts Institute of Technology. Dept. of Physics, 1997. URL: `http://hdl.handle.net/1721.1/10768` (visited on 10/15/2019) (cit. on p. 35).

[124] Y. Castin. *Course 1: Bose-Einstein Condensates in Atomic Gases: Simple Theoretical Results*. Springer, 2001 (cit. on p. 37).

[125] Peter van der Straten Harold Metcalf. *Laser Cooling and Trapping*. Springer-Verlag GmbH, Nov. 1, 1999. ISBN: 0387987282. URL: https://www.ebook.de/de/product/3251789/harold_metcalf_peter_van_der_straten_laser_cooling_and_trapping.html (cit. on pp. 37, 62).

[126] S. Stellmer, B. Pasquiou, R. Grimm, and F. Schreck. "Laser Cooling to Quantum Degeneracy." In: *Phys. Rev. Lett.* 110 (2013), p. 263003. DOI: 10.1103/PhysRevLett.110.263003. URL: http://link.aps.org/doi/10.1103/PhysRevLett.110.263003 (cit. on pp. 37, 46, 47).

[127] Jiazhong Hu, Alban Urvoy, Zachary Vendeiro, Valentin Crépel, Wenlan Chen, and Vladan Vuletić. "Creation of a Bose-condensed gas of 87Rb by laser cooling." In: *Science* 358.6366 (2017), pp. 1078–1080. ISSN: 0036-8075. DOI: 10.1126/science.aan5614. eprint: http://science.sciencemag.org/content/358/6366/1078.full.pdf. URL: http://science.sciencemag.org/content/358/6366/1078 (cit. on p. 37).

[128] Alban Urvoy, Zachary Vendeiro, Joshua Ramette, Albert Adiyatullin, and Vladan Vuletić. "Direct Laser Cooling to Bose-Einstein Condensation in a Dipole Trap." In: *Physical Review Letters* 122.20 (2019). DOI: 10.1103/physrevlett.122.203202 (cit. on pp. 37, 46, 47).

[129] M. S. Chang. "Coherent Spin Dynamics of a Spin-1 Bose-Einstein Condensate." PhD thesis. Georgia Institute of Technology, 2006. URL: http://hdl.handle.net/1853/10547 (cit. on pp. 38, 39).

[130] M. Egorov, B. Opanchuk, P. Drummond, B. V. Hall, P. Hannaford, and A. I. Sidorov. "Measurement ofs-wave scattering lengths in a two-component Bose-Einstein condensate." In: *Physical Review A* 87.5 (2013). DOI: 10.1103/physreva.87.053614 (cit. on p. 38).

[131] C. R. Monroe, E. A. Cornell, C. A. Sackett, C. J. Myatt, and C. E. Wieman. "Measurement of Cs-Cs elastic scattering at T=30 μK." In: *Phys. Rev. Lett.* 70 (4 1993), pp. 414–417. DOI: 10.1103/PhysRevLett.70.414. URL: https://link.aps.org/doi/10.1103/PhysRevLett.70.414 (cit. on p. 38).

[132] K. M. O'Hara, M. E. Gehm, S. R. Granade, and J. E. Thomas. "Scaling laws for evaporative cooling in time-dependent optical traps." In: *Physical Review A* 64.5 (2001), p. 051403. DOI: 10.1103/physreva.64.051403 (cit. on p. 39).

[133] M. Yan, R. Chakraborty, A. Mazurenko, P. G. Mickelson, Y. N. Martinez de Escobar, B. J. DeSalvo, and T. C. Killian. "Numerical modeling of collisional dynamics of Sr in an optical dipole trap." In: *Physical Review A* 83.3 (2011). DOI: 10.1103/physreva.83.032705 (cit. on p. 39).

[134] O. J. Luiten, M. W. Reynolds, and J. T. M. Walraven. "Kinetic theory of the evaporative cooling of a trapped gas." In: *Physical Review A* 53.1 (1996), pp. 381–389. DOI: 10.1103/physreva.53.381 (cit. on p. 39).

[135] E. A. Burt, R. W. Ghrist, C. J. Myatt, M. J. Holland, E. A. Cornell, and C. E. Wieman. "Coherence, Correlations, and Collisions: What One Learns about Bose-Einstein Condensates from Their Decay." In: *Physical Review Letters* 79.3 (1997), pp. 337–340. DOI: 10.1103/physrevlett.79.337 (cit. on p. 39).

[136] C.J. Foot. *Atomic Physics*. Oxford University Press, 2005 (cit. on p. 43).

[137] J.-F. Clément, J.-P. Brantut, M. Robert-de Saint-Vincent, R. A. Nyman, A. Aspect, T. Bourdel, and P. Bouyer. "All-optical runaway evaporation to Bose-Einstein condensation." In: *Phys. Rev. A* 79 (6 2009), p. 061406. DOI: `10.1103/PhysRevA.79.061406`. URL: `http://link.aps.org/doi/10.1103/PhysRevA.79.061406` (cit. on p. 47).

[138] Simon Stellmer, Rudolf Grimm, and Florian Schreck. "Production of quantum-degenerate strontium gases." In: *Physical Review A* 87.1 (2013). DOI: `10.1103/physreva.87.013611` (cit. on p. 47).

[139] J. Rudolph et al. "A high-flux BEC source for mobile atom interferometers." In: *New J. Phys.* 17.6 (2015), p. 065001. ISSN: 1367-2630. DOI: `10.1088/1367-2630/17/6/065001`. URL: `\url{http://iopscience.iop.org/1367-2630/17/6/065001}` (visited on 06/17/2015) (cit. on pp. 46, 47).

[140] Q. Bouton, R. Chang, A. L. Hoendervanger, F. Nogrette, A. Aspect, C. I. Westbrook, and D. Clément. "Fast production of Bose-Einstein condensates of metastable helium." In: *Phys. Rev. A* 91 (6 2015), p. 061402. DOI: `10.1103/PhysRevA.91.061402`. URL: `https://link.aps.org/doi/10.1103/PhysRevA.91.061402` (cit. on p. 47).

[141] T. Kinoshita, T. Wenger, and D.S. Weiss. "All-optical Bose-Einstein condensation using a compressible crossed dipole trap." In: *Phys. Rev. A* 71.1 (2005), p. 011602. DOI: `10.1103/PhysRevA.71.011602` (cit. on p. 47).

[142] M. D. Barrett, J. A. Sauer, and M. S. Chapman. "All-Optical Formation of an Atomic Bose-Einstein Condensate." In: *Physical Review Letters* 87.1 (2001). DOI: `10.1103/physrevlett.87.010404` (cit. on p. 47).

[143] M. Landini, S. Roy, G. Roati, A. Simoni, M. Inguscio, G. Modugno, and M. Fattori. "Direct evaporative cooling of ^{39}K atoms to Bose-Einstein condensation." In: *Physical Review A* 86.3 (2012). DOI: `10.1103/physreva.86.033421`. URL: `\url{http://link.aps.org/doi/10.1103/PhysRevA.86.033421}` (cit. on pp. 46, 47).

[144] Alban Urvoy. *About the experiment sequence cycle time.* E-Mails from 27.11.2019 and 29.11.2019. private communication (cit. on p. 47).

[145] S. Abend et al. "Atom-Chip Fountain Gravimeter." In: *Phys. Rev. Lett.* 117 (2016), p. 203003. DOI: `10.1103/PhysRevLett.117.203003` (cit. on p. 47).

[146] Daniel M. Farkas, Kai M. Hudek, Evan A. Salim, Stephen R. Segal, Matthew B. Squires, and Dana Z. Anderson. "A compact, transportable, microchip-based system for high repetition rate production of Bose–Einstein condensates." In: *Applied Physics Letters* 96.9 (2010), p. 093102. DOI: `10.1063/1.3327812` (cit. on pp. 46, 47).

[147] D.M. Farkas, E.A. Salim, and J. Ramirez-Serrano. "Production of Rubidium Bose-Einstein Condensates at a 1 Hz Rate." In: *ArXiv* (2014). URL: `https://arxiv.org/abs/1403.4641v2` (cit. on p. 47).

[148] M. Horikoshi and K. Nakagawa. “Atom chip based fast production of Bose–Einstein condensate.” In: *Applied Physics B* 82.3 (2006), pp. 363–366. DOI: 10.1007/s00340-005-2083-z (cit. on p. 47).

[149] U Ernst, A Marte, F Schreck, J Schuster, and G Rempe. “Bose-Einstein condensation in a pure Ioffe-Pritchard field configuration.” In: *Europhysics Letters (EPL)* 41.1 (1998), pp. 1–6. DOI: 10.1209/epl/i1998-00107-2 (cit. on pp. 46, 47).

[150] J Arlt, O Maragò, E Hodby, S A Hopkins, G Hechenblaikner, S Webster, and C J Foot. “Bose-Einstein condensation in a rotating anisotropic TOP trap.” In: *Journal of Physics B: Atomic, Molecular and Optical Physics* 32.24 (1999), pp. 5861–5869. DOI: 10.1088/0953-4075/32/24/320 (cit. on pp. 46, 47).

[151] M. Zaiser, J. Hartwig, D. Schlippert, U. Velte, N. Winter, V. Lebedev, W. Ertmer, and E. M. Rasel. “Simple method for generating Bose-Einstein condensates in a weak hybrid trap.” In: *Phys. Rev. A* 83 (2011), p. 035601. DOI: 10.1103/PhysRevA.83.035601. URL: \url{http://link.aps.org/doi/10.1103/PhysRevA.83.035601} (cit. on pp. 47, 59).

[152] K.L. Moore, T.P. Purdy, K.W. Murch, K.R. Brown, K. Dani, S. Gupta, and D.M. Stamper-Kurn. “Bose–Einstein condensation in a mm-scale Ioffe–Pritchard trap.” In: *Applied Physics B* 82.4 (2006), pp. 533–538. DOI: 10.1007/s00340-005-2101-1 (cit. on p. 46).

[153] Tim Kovachy, Sheng wey Chiow, and Mark A. Kasevich. “Adiabatic-rapid-passage multiphoton Bragg atom optics.” In: *Physical Review A* 86.1 (2012). DOI: 10.1103/physreva.86.011606. URL: \url{http://link.aps.org/doi/10.1103/PhysRevA.86.011606} (cit. on p. 48).

[154] Ekkehard Peik, Maxime Ben Dahan, Isabelle Bouchoule, Yvan Castin, and Christophe Salomon. “Bloch oscillations of atoms, adiabatic rapid passage, and monokinetic atomic beams.” In: *Physical Review A* 55.4 (1997), pp. 2989–3001. DOI: 10.1103/physreva.55.2989. URL: http://link.aps.org/doi/10.1103/PhysRevA.55.2989 (cit. on p. 48).

[155] L. Antoni-Micollier, B. Barrett, L. Chichet, G. Condon, B. Battelier, A. Landragin, and P. Bouyer. “Generation of high-purity low-temperature samples of K39 for applications in metrology.” In: *Physical Review A* 96.2 (2017). DOI: 10.1103/physreva.96.023608 (cit. on p. 48).

[156] Robin Corgier. “Engineered atomic states for precision interferometry.” PhD thesis. IQ, 2019, p. 192. DOI: https://doi.org/10.15488/5152. URL: https://www.repo.uni-hannover.de/handle/123456789/5199 (cit. on pp. 50, 52).

[157] P. Pedri, D. Guéry-Odelin, and S. Stringari. “Dynamics of a classical gas including dissipative and mean-field effects.” In: *Physical Review A* 68.4 (2003). DOI: 10.1103/physreva.68.043608 (cit. on pp. 50, 52).

[158] D. Guéry-Odelin. “Mean-field effects in a trapped gas.” In: *Physical Review A* 66.3 (2002). DOI: 10.1103/physreva.66.033613 (cit. on p. 50).

[159] Y. Castin and R. Dum. “Bose-Einstein Condensates in Time Dependent Traps.” In: *Physical Review Letters* 77.27 (1996), pp. 5315–5319. DOI: 10.1103/physrevlett.77.5315. URL: http://link.aps.org/doi/10.1103/PhysRevLett.77.5315 (cit. on p. 52).

[160] Kosuke Shibata, Hidehiko Ikeda, Ryota Suzuki, and Takuya Hirano. “Compensation of gravity on cold atoms by a linear optical potential.” In: *Physical Review Research* 2.1 (2020). DOI: 10.1103/physrevresearch.2.013068 (cit. on pp. 56, 63).

[161] Sascha Kulas et al. “Miniaturized Lab System for Future Cold Atom Experiments in Microgravity.” In: *Microgravity Science and Technology* 29.1-2 (Oct. 31, 2016), pp. 37–48. DOI: 10.1007/s12217-016-9524-7 (cit. on p. 65).

[162] T. Lauber, J. Küber, O. Wille, and G. Birkl. “Optimized Bose-Einstein-condensate production in a dipole trap based on a 1070-nm multifrequency laser: Influence of enhanced two-body loss on the evaporation process.” In: *Phys. Rev. A* 84 (4 2011), p. 043641. DOI: 10.1103/PhysRevA.84.043641. URL: https://link.aps.org/doi/10.1103/PhysRevA.84.043641 (cit. on p. 67).

[163] R. A. Cline, J. D. Miller, M. R. Matthews, and D. J. Heinzen. “Spin relaxation of optically trapped atoms by light scattering.” In: *Opt. Lett.* 19.3 (1994), pp. 207–209. DOI: 10.1364/OL.19.000207. URL: http://ol.osa.org/abstract.cfm?URI=ol-19-3-207 (cit. on p. 67).

CURRICULUM VITAE

PERSONALIEN:

Name: Henning Albers
Geboren: 17. Mai 1986 in Bückeburg (Niedersachsen)
Nationalität: deutsch

PROMOTION:

12/2013 - heute	Wissenschaftlicher Mitarbeiter in der Arbeitsgruppe Prof. Dr. Ernst Maria Rasel am Institut für Quantenoptik, Leibniz Universität Hannover

STUDIUM:

November 2013	Abschluss: Master of Science Thema der Masterarbeit: "Atominterferometrie mit ^{39}K ", durchgeführt in der Arbeitsgruppe Prof. Dr. Ernst Maria Rasel am Institut für Quantenoptik, Leibniz Universität Hannover
10/2007 - 11/2013	Leibniz Universität Hannover, Studium der Physik

ZIVILDIENST:

08/2006- 05/2007	im Kindergarten am Kammweg der Stadt Obernkirchen

SCHULBILDUNG:

Juni 2006	Abschluss: Abitur, allgmeine Hochschulreife
08/2003- 06/2006	Fachgymnasium Technik an den Berufsbildenden Schulen Stadthagen

PUBLICATIONS

Publications in peer-reviewed journals:

- D. Schlippert, J. Hartwig, **H. Albers**, L. L. Richardson, C. Schubert, A. Roura, W. P. Schleich, W. Ertmer, and E. M. Rasel:
  Quantum Test of the Universality of Free Fall.
  Phys. Rev. Lett. 112, 203002 (2014)
- C. Vogt, M. Woltmann, S. Herrmann, C. Lämmerzahl, **H. Albers**, D. Schlippert, and E. M. Rasel:
  Evaporative cooling from an optical dipole trap in microgravity.
  Phys. Rev. A 101, 013634 (2020)
- *Accepted for publication in "The European Physical Journal D" (EPJ D):*
  H. Albers, A. Herbst, L. L. Richardson, H. Heine, D. Nath, J. Hartwig, C. Schubert, C. Vogt, M. Woltmann, C. Lämmerzahl, S. Herrmann, W. Ertmer, E. M. Rasel, D. Schlippert:
  Quantum test of the Universality of Free Fall using rubidium and potassium.
  DOI: *10.1140/epjd/e2020-10132-6*
  pre-print version: *arXiv:2003.00939 (2020)*

Others:

- D. Schlippert, **H. Albers**, L. L. Richardson, D. Nath, H. Heine, C. Meiners, E. Wodey, A. Billon, J. Hartwig, C. Schubert, N. Gaaloul, W. Ertmer, and E. M. Rasel:
  Ground Tests of Einstein's Equivalence Principle: From Lab-based to 10-m Atomic Fountains.
  arXiv:1507.05820 (2015)
- L. L. Richardson, D. Nath, A. Rajagopalan, **H. Albers**, C. Meiners, C. Schubert, D. Tell, E. Wodey, S. Abend, M. Gersemann, W. Ertmer, D. Schlippert, E. M. Rasel, M. Mehmet, L. Kumanchik, L. Colmenero, R. Spannagel, C. Braxmaier, and F. Guzman:
  Opto-mechanical resonator-enhanced atom interferometry.
  arXiv:1902.02867 (2019)